Whitmarsh, R.B., Beslier, M.-O., Wallace, P.J., et al., 1998
Proceedings of the Ocean Drilling Program, Initial Reports, Vol. 173

4. SITE 1065[1]

Shipboard Scientific Party[2]

HOLE 1065A

Position: 40°43.447′N, 11°17.724′W

Start hole: 1800 hr, 22 April 1997

End hole: 0830 hr, 1 May 1997

Time on hole: 206.5 hr (8.6 days)

Seafloor (drill pipe measurement from rig floor, mbrf): 4781.0

Total depth (drill pipe measurement from rig floor, mbrf): 5412.40

Distance between rig floor and sea level (m): 10.9

Water depth (drill pipe measurement from sea level, m): 4770.1

Penetration (mbsf): 631.40

Coring totals:
Type: RCB; Number: 35; Cored: 375.8 m; Recovered: 46.6 m; Average recovery: 12.4%

Formation:
Unit II: (251.0–308.8 mbsf): nannofossil chalk and nannofossil claystone (early Miocene)
Unit V: (308.8–631.4 mbsf): clay, claystone, and dolomitic claystone (Middle to Upper Jurassic)
(Note: units were defined on the basis of lithology. However, because we did not continuously core the sedimentary sequence at Site 1065, we chose unit numbers to be consistent with those previously defined in this region in 1993 during Leg 149.)

Principal results: Site 1065 lies in a water depth of 4770 m near the northern edge of the southern Iberia Abyssal Plain. The site is crossed by a single east-west time-migrated seismic reflection profile that shows a large basement high with relief of 1.7 s TWT (~2000 m) on its west side, conformably overlain by 0.2–0.35 s TWT of seismically weakly reflective ("transparent") sediment on its landward (east) side. This basement high is the largest of a series of highs on the seismic profile that reduce in relief westward and which on time sections are bounded on their oceanward (west) sides by strong, curved reflectors. These reflectors are probably normal faults that were involved in the rifting process and suggest that the Site 1065 high is a fault block tilted toward the continent. The basement high and the "transparent" sediments are overlain by subhorizontally layered postrift sediments. The principal drilling objective was to identify the nature of the basement rocks and, if continental, to determine the approximate crustal level from which the rocks originated and their petrostructural evolution, in order to better constrain the modes of crustal thinning and breakup during a rifting episode. Ancillary objectives were to date the overlying prerift or synrift sediments and to determine the early subsidence history of the fault block.

Site 1065 was chosen to reach igneous or metamorphic rocks in a tilted fault block with the principal objective of determining whether the block consisted of continental crust. While the shallow-water lithologies found in the prerift/synrift (Middle–Upper Jurassic) sediments strongly indicated the presence of underlying continental crust, igneous or metamorphic basement was not reached; the acoustic basement reflection appears to be caused by lithification of Jurassic clays, under which no clear seismic reflection from the top of the crystalline crust could be discerned.

The lithostratigraphic units used during Leg 173 took into account the lithostratigraphy defined during Leg 149. The sedimentary section in Hole 1065A consists of two lithostratigraphic units: slumped lower Miocene nannofossil chalks and claystones (Unit II, >58 m thick) overlying Middle to Upper Jurassic clays, claystones, and dolomitic claystones (Unit V, >322 m). The light greenish gray to dark gray thinly bedded and laminated nannofossil chalks and claystones of Unit II were largely deposited from suspension as pelagites and hemipelagites. Intensive soft-sediment deformation characterizes the major part of Unit II. Pebbles of continental basement lithologies and shallow-water limestones occur, probably originating from the seamounts some 30 km north of Site 1065. The limestones are very similar to Tithonian rocks recovered during Leg 103 from the Galicia Bank margin. Unit V is subdivided into two subunits. Dark greenish gray to medium dark gray soft clay dominates Subunit VA (192.7 m); these clays were remarkably plastic and drilling through them was very slow. Subunit VB (>129.9 m) consists of claystone, some of which is dolomitic. The lithology, intense bioturbation, and virtual absence of cross stratification indicates deposition below wavebase in an offshore shelf environment. Muddy and silty sediments were probably transported into the area in suspension and by low-density turbidity currents. A few thin beds of coarse sand and conglomerate, also deposited by turbidity currents, contain shallow-water limestones and lithoclasts of slate and meta-arenite derived from a nearby source area.

Unit II exhibits pervasive slump folds, closely-spaced microfault arrays with both extensional and contractional orientations, and low-angle, clay-rich shear zones. Overprinting relations indicate a prolonged history of soft-sediment deformation. Bedding dips measured in the cores are highly variable because of the slumping. Unit V is much less deformed than Unit II. Only minor soft-sediment deformation is observed, as well as some extensional microfaults that postdate lithification. After its deposition, Unit V was tilted into its present, moderately dipping orientation. Bedding dips measured on the cores from this unit range between 0° and 65°. The mean dip is 18° with a standard deviation of 10°.

Calcareous microfossils are moderately to well preserved and abundant in the lower Miocene chalks of lithostratigraphic Unit II but are virtually absent in some intercalated siliceous claystones such as in Section 173-1065A-2R-CC, which is dominated by abundant sponge spicules and contains rare radiolarians. Relatively undisturbed chalks in the first two sections of Core 173-1065A-1R cap the underlying slump complex and, as such, provide a minimum date for its time of emplacement of ~16.7 Ma, based on the absence of middle Miocene planktonic foraminiferal index taxa. These overlying sediments are assigned to the planktonic foraminiferal Zone N7 and nannofossil Zone NN4. The slump complex extends down through Core 6 and involves sediment mainly from the long-ranging nannofossil Zone NN2, but may well include a complete suite of lower Miocene strata from NN1 to NN3 (or N4 to N6).

Small numbers of moderately to well-preserved nannofossils provide a Tithonian age for the upper portion of the prerift/synrift sediments (Cores 173-1065A-8R to 13R), but only long-ranging taxa are present down to Core 20R. A 132-m barren interval separates this core from the lower 33 m of the hole, which contains dissolution-resistant nannofossils that may have been introduced with turbidites. These constrain the age of the bottom of the section to only Middle to Late Jurassic. Calcareous benthic foraminifers are very rare and occasionally pyritized within these older clastic sediments, which also contain rare, sporadic occurrences of poorly preserved, indeterminate agglutinated foraminifers.

---

[1] Whitmarsh, R.B., Beslier, M.-O., Wallace, P.J., et al., 1998. *Proc. ODP, Init. Repts.,* 173: College Station, TX (Ocean Drilling Program).

[2] Shipboard Scientific Party is given in the list preceding the Table of Contents.

Prior Chapter Contents Next Chapter

Shipboard magnetostratigraphy within the early Miocene interval is not well defined because of the low core recovery, although there are distinct changes in polarity in portions of the cores. The construction of a magnetostratigraphy over this interval is not possible because of the absence of adequate age control, poor recovery, and the disturbance caused by slumps. The Jurassic cores all have normal polarity except for a short reversed interval in Core 173-1065A-29R (569.7–569.9 mbsf). This short reversal will have to be confirmed by shore-based work. Rocks of this age were generally recovered in relatively long, coherent sections of core and revealed consistent downhole inclinations after AF demagnetization. A preliminary calculation of paleolatitude from these inclination data suggests that the drilling site was located at ~23°N during the deposition of lithostratigrahic Unit V, indicating that 17° northward displacement of the region has occurred since Late Jurassic.

Methane concentrations in headspace gases were very low, varying from 2 to 6 ppm, and concentrations of other hydrocarbons, CO, CO_2, and H_2S were generally below detection. Carbonate contents are relatively high in the chalks of Unit II (avg. 68%) and variable in the sediments of Unit V, ranging from values <1% in clay and claystone to around 60% in chalk and dolomitic claystone. Unit II sediments contain only trace amounts of organic carbon, but in Unit V organic carbon contents are quite variable, ranging from 0.1% to 0.85% (avg. 0.4%). The organic matter generally appears to have a marine origin. However, organic C/N ratios as great as 20 indicate a component of terrestrial-sourced material, consistent with the presence of microscopic plant fragments (charcoal) in some sediments.

Between 251.0–631.4 mbsf, wet bulk densities range from 1.7 to 2.8 g/cm^3, porosities vary between 2 and 60%, and acoustic velocity ranges from 1.7 to 5.7 km/s. Grain densities for all but two samples are almost constant around 2.75 g/cm^3. There is a strong negative correlation between wet bulk density and porosity. Although bulk densities increase and porosities decrease downward in general, there are two layers associated with lithostratigraphic (and most likely seismic) unit boundaries that have particularly low porosities, high bulk densities, and high velocities. One of these layers appears near 330 mbsf, which is just below the contact between Unit II and Subunit VA, and the other at about 500 mbsf, near the boundary between Subunits VA and VB. These layers consist of limestone in which the maximum acoustic velocity is more than twice the velocity in the adjacent sediments.

Logging data correlated well with the lithostratigraphic units identified from core observations. A sharp increase in natural gamma-ray intensity, which is an indicator of the abundance of clay minerals, was observed between lithostratigraphic Units II and V (309–304 mbsf), as well as a pronounced decrease in the photoelectric effect, an indicator of atomic weight and, hence, indirectly of sediment type. Neutron porosity was generally high in Unit V and may be attributed to the high clay content of the formation and/or to the enlarged borehole. Resistivity increased smoothly with depth. The variable resistivity observed in Subunit VB is probably caused by bands of well-lithified claystone. The calipers revealed that the hole was washed out above 510 mbsf. The hole deviated slightly (1°–2°) in a northwest (350 mbsf) to northeast (600 mbsf) direction. Good quality FMS images were recorded in the lowest part of the hole. Preliminary analysis identified sedimentary layers dipping about 20° toward the east to northeast, whereas paleomagnetism indicates 25° dip toward N35°E.

BACKGROUND AND OBJECTIVES

Part of understanding the tectonic and magmatic processes accompanying continental rifting and breakup is to determine (1) the landward edge of the ocean/continent transition (OCT) to constrain the location of continental breakup, (2) the petrostructural evolution of the continental crust adjacent to the OCT, and (3) the synrift and immediately prerift history of sediments on the continental fault blocks. Also inherent in this approach is confirmation that basement features seen in seismic profiles are in fact continental fault blocks.

Many seismic profiles across rifted continental margins detect large, slightly asymmetric basement highs, which are commonly interpreted to be tilted fault blocks of continental crust. Sometimes such blocks are associated with deeply penetrating normal faults on their oceanward side and, more rarely, they may show wedge-shaped sediment bodies with fan-like internal reflectors that are interpreted to be synrift deposits. However, some of these characteristics also appear to exist in slow-spreading oceanic crust and have even been used as arguments for the presence of such crust in the OCT under the southern Iberia Abyssal Plain (Whitmarsh and Sawyer, 1996). Moreover, although the landward edge of the OCT is marked by the deepest continental fault block, some fragments or slivers of continental crust may occur within the OCT. Clearly, therefore, resolution of the composition and nature of fault blocks within the OCT is an important objective.

During Leg 149, drilling took place in the sediments overlying one tilted fault block that was covered conformably by a seismically weakly reflective layer on its landward side. Continental basement was inferred to be present at this site, Site 901, on the basis of the presence of Tithonian shallow-water benthic foraminifers, rare planktonic foraminifers, and the absence of bathyal-abyssal agglutinated foraminifers (Collins et al., 1996), but time prevented basement from being reached. Although reoccupation of Site 901 was proposed at one time for Leg 173, a better site (IBERIA-08B) was discovered during a geophysical cruise to the area in 1995 (Minshull, 1995). This site (which became Site 1065) not only lay further west, but also had less sediment over acoustic basement.

Thus, the principal objective of Site 1065 was to identify the nature of the basement rocks and, assuming it is continental, to determine the approximate crustal level from which the rocks originated and their petrostructural evolution. Determination of pressure, temperature, time (P-T-t) paths of crustal rocks will help to constrain the timing of events, and the rheology, stretching, and breakup mechanisms of the crust during the rifting episode. Most of the continental rocks that have been sampled so far on the northern Galicia Bank belong to the upper crust. Their characteristics suggest they belong to the major Variscan units known on land (Capdevila and Mougenot, 1988). Some granulites, in the form of allochthonous clasts, have been sampled on the northern Galicia margin (Capdevila et al., 1980), where they are Archean in age (Postaire, 1983; Guerrot et al., 1989), at the foot of the west Galicia margin (Boillot et al., 1995; Fuegenschuh et al., in press), and from Vigo Seamount (Capdevila and Mougenot, 1988). Ancillary objectives were to date the overlying pre- or synrift sediments and to determine the early subsidence history of the fault block.

Site 1065 lies in a water depth of 4770 m near the northern edge of the southern Iberia Abyssal Plain (Fig. 1). The site is crossed by a single east-west time-migrated seismic reflection profile (Fig. 2) that shows a large basement high with relief of 1.7 s TWT (~2000 m) on its west side, overlain by 0.2–0.35 s of seismically “transparent” sediment on its landward side. The top of the basement high on a depth-migrated section is convex, a shape that could be produced by submarine or subaerial mass wasting of soft sediments (Fig. 3). The landward extent of the “transparent” layer is unclear, because the seismic profile ended a short distance east of the crest of the high. The basement high is the largest of a series of highs that reduce in relief westward and that, on time-migrated seismic reflection sections, are bounded on their oceanward (west) sides by strong curved reflectors that are probably faults that were involved in the rifting process. The basement high and the seismically weakly reflective sediments are overlain by subhorizontally layered postrift sediments. The site was picked at FFID (shotpoint) 6320, but the borehole location was shifted back (westward) along *Discovery*’s track by 126 m to allow for the offset between the airgun array and the ship’s GPS aerial. At FFID 6320 there is 0.35 s of postrift sediment and ~0.2 s of “transparent” material. Therefore, we expected to drill through 330 m of postrift sediments (presumed to be turbidites and pelagites by analogy with Site 900 which lies 13 km to the west). The thickness of the “transparent” layer was more difficult to predict as it comprised an unknown lithology (the possibly equivalent lithology was poorly sam-

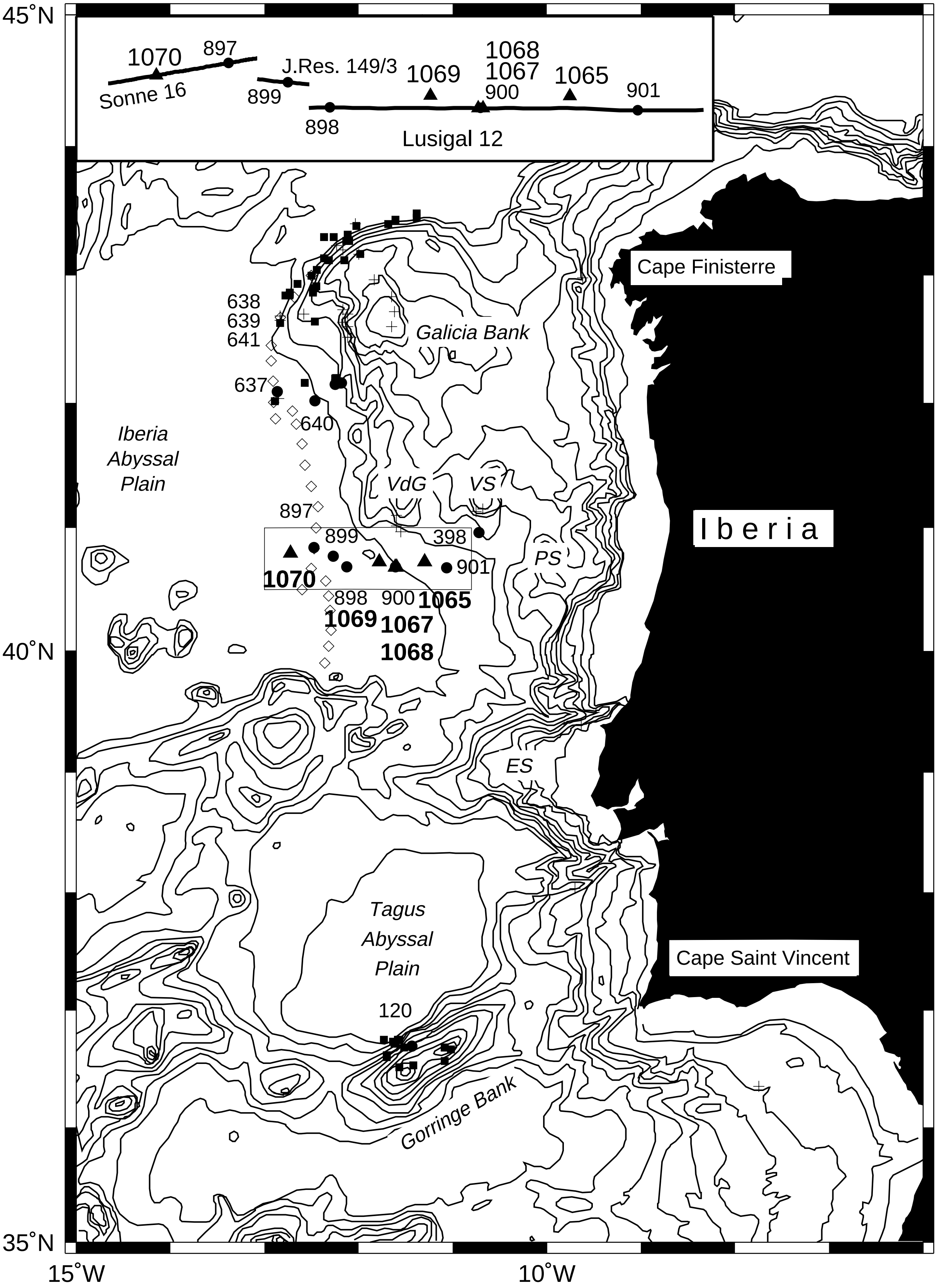

Figure 1. Contoured bathymetric chart of the west Iberia margin. Contours at 500 m intervals. Leg 173 sites are shown by triangles with bold numbers; sites drilled on earlier legs are shown by solid circles. PS, VS, and VdG correspond to Porto, Vigo, and Vasco da Gama Seamounts, respectively. ES denotes the Estremadura Spur. Solid squares and crosses = samples obtained by submersible and dredging, respectively. Inset shows relative positions of sites and locations of three seismic reflection profiles used to construct the composite section shown in Figure 3, “Leg 173 Introduction” chapter, this volume.

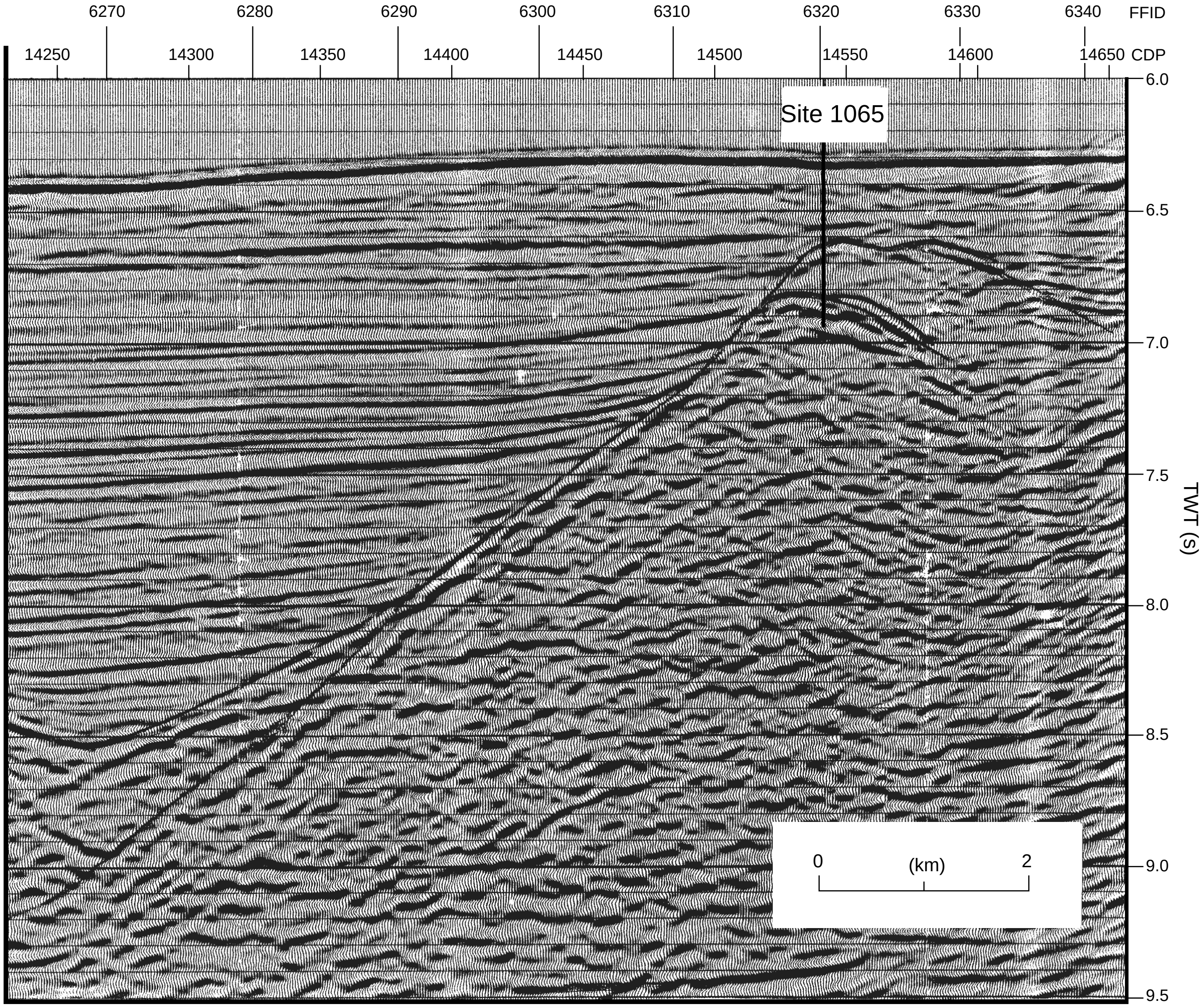

Figure 2. Time-migrated seismic reflection profile CAM144 across Site 1065 (left to right = west to east).

pled in only 3 cores at Site 901, which averaged 14% recovery). For planning purposes, a conservatively high interval velocity of 3.0 km/s was assumed, which gave a thickness of 300 m and a depth to basement of 630 mbsf.

A depth-to-basement contour chart shows that the site lies near the crest of a north-northwest–trending basement ridge that plunges southward. This ridge appears to be the southward continuation beneath the southern Iberia Abyssal Plain of a steep-sided ridge on the southern flank of the Galicia Bank massif (Figs. 1, 4) which lies just east of Vasco da Gama Seamount. Dredge samples from this seamount include phyllites and meta-arkoses (Capdevila and Mougenot, 1988).

OPERATIONS

Portuguese Drilling Clearance

Before ODP Leg 173, clearance had been obtained from the Portuguese government to operate in the Portuguese Exclusive Economic Zone (EEZ). However, while the *JOIDES Resolution* was in port in Lisbon, a Portuguese telecommunications company, Marconi Portugal, filed a written protest with the Portuguese Ministry of Foreign Affairs asking that Leg 173 drilling clearance be withdrawn. They were concerned about possible damage to seafloor telecommunication cables (TAGIDE 1, TAGIDE 2, Eurafrica, TAT-9, and FLAG) located in the Iberia Abyssal Plain operating area. A meeting was held with Marconi on 17 April 1997 in an attempt to alleviate their concerns. It was explained to Marconi that the drill ship could locate itself very accurately using a sophisticated Global Positioning System (GPS), that it was a dynamically positioned drill ship that did not require the setting or recovery of anchors, and that the seafloor could be visually surveyed using a subsea TV system before spudding any drill hole. They were further told that all of the Leg 173 drill sites were at least 2.0 nm away from the cables in question. Marconi was not appeased and reiterated its position that all drill sites should be moved outside a 15-nm corridor extending on either side of each cable. The Foreign Ministry subsequently put the Leg 173 drilling clearance verbally on hold until the problem could be resolved.

During further negotiations, ODP/TAMU agreed in writing to assume full fiscal liability for cable damage and in addition agreed to

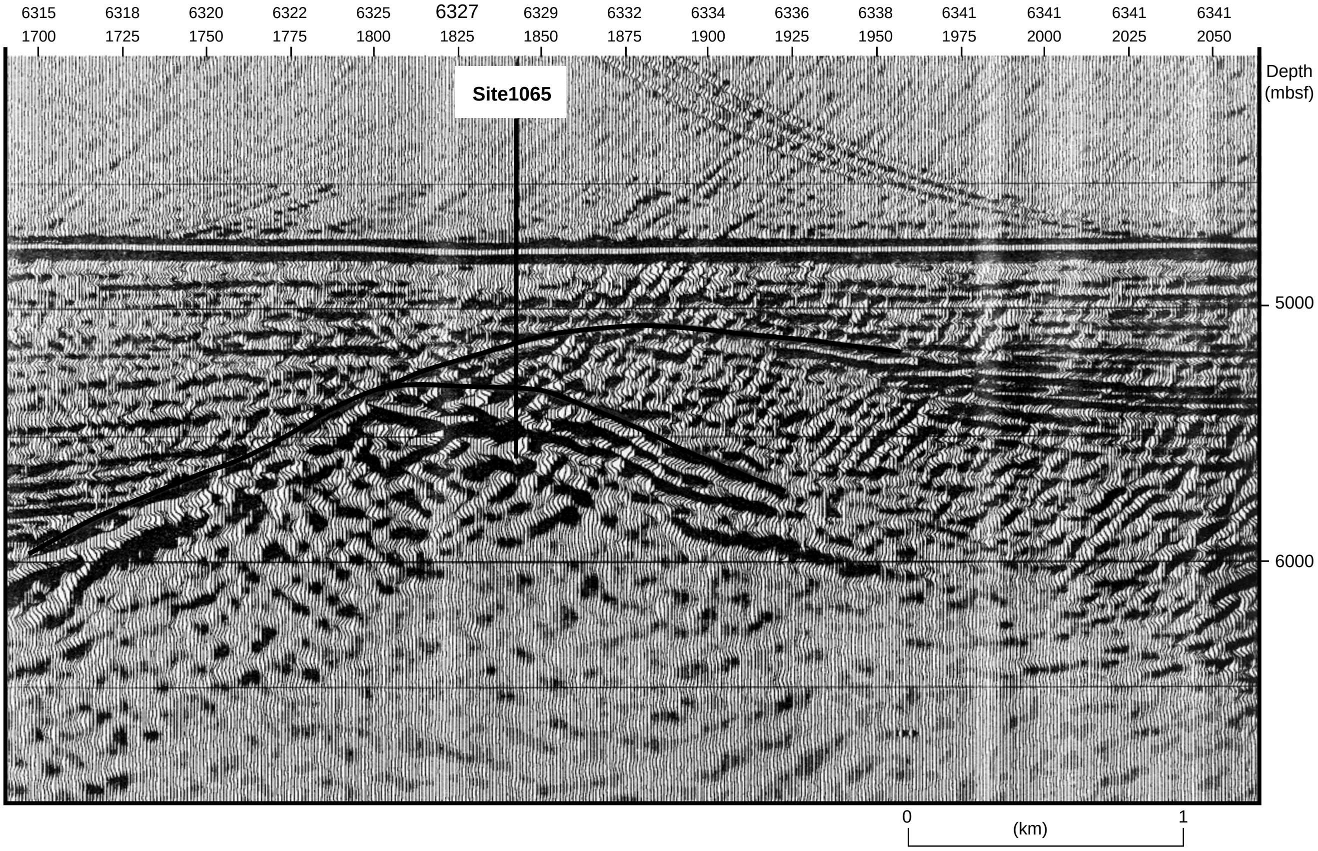

Figure 3. A depth-migrated portion of seismic profile CAM144 (courtesy D. Chian). Velocities determined by pre-stack analysis were used to construct the depth section; computed depths of the seismically weakly reflective and basement layers do not agree well with observations at Site 1065. Note the slightly beveled appearance of the top of the basement in the vicinity of the site.

drop Site IBERIA-08A from the drilling prospectus. This resulted in the closest drill site being Site IBERIA-08B (Site 1065), which was located 3.6 nm away from TAGIDE 1. Marconi continued to resist removing their official protest, and the Ministry of Foreign Affairs was reluctant to reinstate the drilling clearance while the protest remained in effect. The issue was finally resolved when ODP/TAMU further agreed to assume all financial liability for lost revenue should a cable become damaged as a result of the drilling operation. It should be noted that the vessel would have officially sailed from Lisbon at 0745 hr 20 April had it not been for the drilling clearance problem. This incident cost the leg nearly 1.5 days (34.25 hr) of operating time, excluding about 6 hr spent waiting for clearance at the first site.

Transit to Site 1065

At 1800 hr on Monday, 21 April 1997, the last line was passed ashore and the vessel headed down the river Tagus to the entrance of Lisbon harbor. At 1830 hr the pilot was away and the vessel got under way at full speed toward the first site of Leg 173. Clocks were set back 1 hr to GMT during the night. The 170-nm transit to Site 1065 was accomplished at an average speed of 7.2 kt. The transit was undertaken at a reduced speed because official drilling clearance had not yet been received. The vessel arrived on location at 1630 hr 22 April 97. Thrusters and hydrophones were lowered and the vessel began “drifting” on location in dynamic positioning (DP) mode. At 1700 hr, word was received that a beacon could be deployed, drill pipe tripped to the seafloor, and a subsea TV survey conducted while awaiting clearance. Permission to spud into the seafloor remained withheld.

Hole 1065A

At 1800 hr on 22 April, a Datasonics beacon was dropped on the GPS coordinates for Site 1065, officially initiating Hole 1065A. The beacon subsequently failed within 2.25 hr and a second beacon was deployed at 2015 hr. The precision depth recorder (PDR) indicated a seafloor depth of 4780.4 m, adjusted to the rig floor. The pipe was tripped to the seafloor and the subsea camera was deployed. While awaiting clearance to spud the hole, a visual TV survey was done for 1000 m to the west and 880 m to the east of the site. The GPS coordinates placed this site ~5 nm west of the TAGIDE 1 cable and ~10 nm to the east of the TAGIDE 2 cable. There was no visual indication that the site location was at or near any subsea cables.

At 1715 hr, 23 April 97, word was received that the hold on drilling clearance for the Portuguese EEZ had been removed by the Ministry of Foreign Affairs, allowing us to begin Leg 173 scientific drilling and coring operations. At 1730 hr, Hole 1065 was spudded at a seafloor depth of 4781.0 m. Once the TV was recovered, drilling operations commenced using the RCB coring system with a center bit installed. The hole was drilled to a depth of 251.0 mbsf in ~12.5 hr, including one inspection and the final recovery of the center bit before initiating coring operations.

Continuous wireline coring proceeded initially with an acceptable 40.9% recovery (Table 1) from 251.0 to 308.8 mbsf (nannofossil chalk and claystone). Recovery became very poor (<5%; Table 1) be-

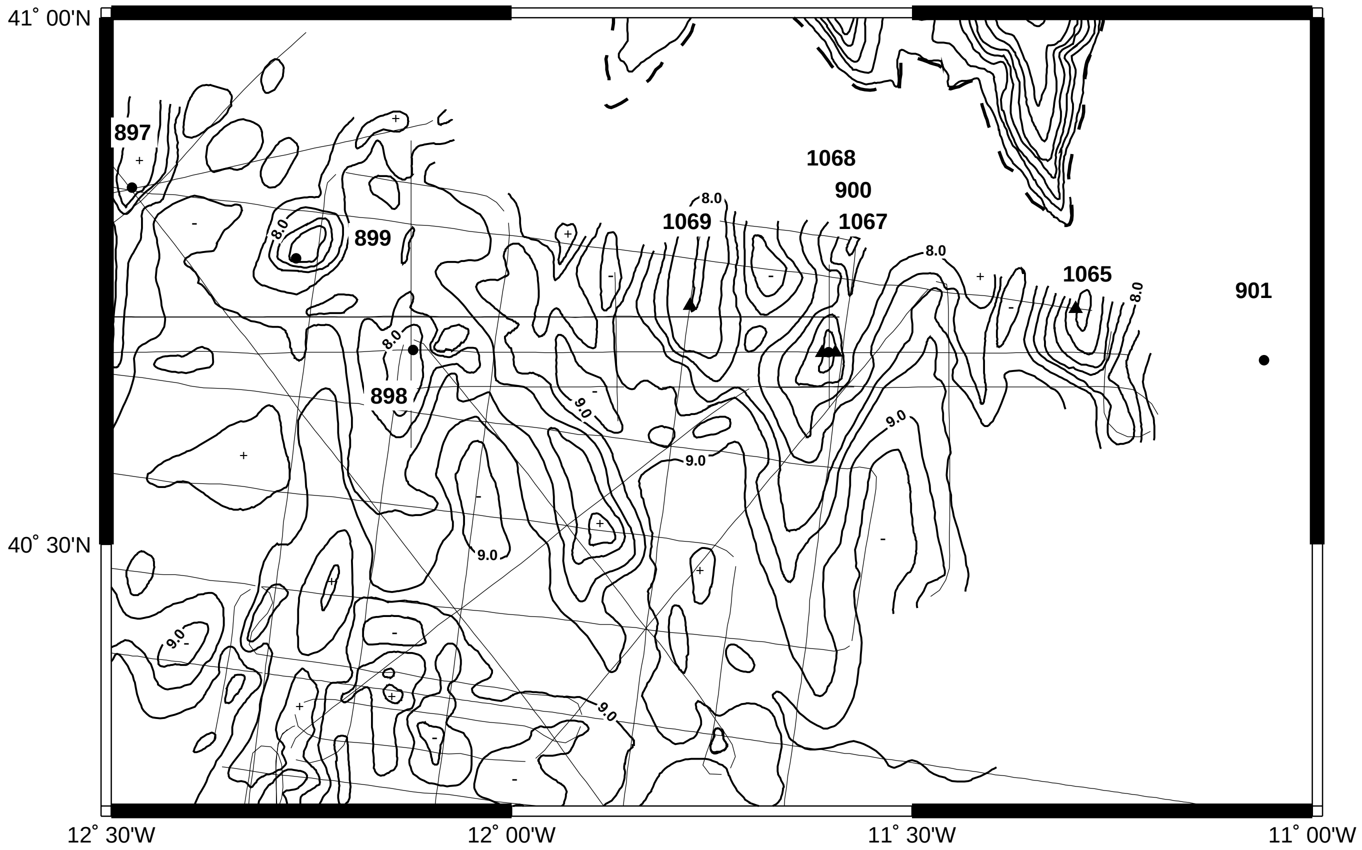

Figure 4. Contour chart of two-way traveltime (TWT) to basement (contour interval 0.25 s TWT, ~250 m; contouring based on work by C.M. Krawczyk, L.M. Pinheiro, S.M. Russell, and R.B. Whitmarsh) combined with bathymetry of the relief bordering the Iberia Abyssal Plain (contour interval 250 m; courtesy J-C. Sibuet). Dashed line denotes edge of the abyssal plain. Leg 149 and 173 sites are shown by solid circles and solid triangles, respectively. Fine lines are tracks of seismic lines used to contour basement. Selected basement highs and lows are indicated by + and –, respectively.

low 308.8 mbsf (soft clay, siltstone, sandstone, and breccia). Acoustic basement was reached at a depth of ~501.5 mbsf. At this point, the rate of penetration continued to be slow (3.8 m/hr); however, recovery did improve slightly, averaging 13.2% over the interval from 501.5 to 631.4 mbsf (Table 1). Because of the bad drilling conditions and the lack of crystalline basement beneath the reflector defining the top of the acoustic basement, coring was halted at a depth of 631.4 mbsf at 1830 hr on 29 April, and preparations were begun for wireline logging.

The hole was swept with sepiolite drilling mud and then a wiper trip was made to a depth of 100 mbsf and back. Pipe overpull of 50,000 lb was noted at 331.0 mbsf during the trip out, and a bridge was encountered at 585.0 mbsf on the return. A minimal amount of fill (~1.0 m) was found on the bottom. The bit was released, the sleeve shifted, the hole was displaced with sepiolite mud, and the pipe was placed at a logging depth of 108 mbsf. Wireline logging proceeded with the first suite of logging tools, the triple combination, consisting of HNGS/ARS/HLDT/DIT/TLT. The first run had trouble passing a tight spot in the hole at 321.0 mbsf but the tools were eventually worked through and reached within 5 m of the bottom. On the return trip the tools would not pass the same tight spot. After 1.5 anxious hours, the tools were eventually worked through the suspected keyseat and recovered back aboard ship. The pipe was then lowered across the bad zone, placing the open ended pipe at a depth of 5128.0 m (347.0 mbsf). The second logging run consisted of the NGT, SDT, and FMS. These tools reached to within 17.4 m of bottom and yielded some good logs in areas where the hole was not vastly over gauge. After wireline logging operations were concluded, the pipe was pulled clear of the seafloor and the primary positioning beacon was released and recovered.

Transit to Site 1066

While the pipe trip continued, the vessel was moved in DP mode at ~0.5 kt to a way point located halfway between Sites 1066 (IBERIA-09B) and 1067 (IBERIA-09A). The end of the bottom-hole assembly reached the rig floor at 0830 hr 1 May 97, officially ending Hole 1065A and beginning Hole 1066A. A new RCB bit and bit release were made up and the pipe was started back to bottom. Once the way point was reached (~375 m from each of the two sites), a primary positioning beacon was deployed at 1345 hr on 1 May 97. The vessel then continued on to the GPS coordinates for Site 1066.

LITHOSTRATIGRAPHY

The sedimentary section at Site 1065 consists of two lithostratigraphic units: slumped early Miocene nannofossil chalk (lithostratigraphic Unit II) overlying Middle to Upper Jurassic clay, claystone, dolomitic claystone, sandstone, and conglomerate (lithostratigraphic Unit V).

A simplified summary of the lithostratigraphy cored at this site and other Leg 173 and Leg 149 sites is shown in Figure 5. As discussed in the “Explanatory Notes” chapter (this volume), the defini-

Table 1. Site 1065 coring summary.

Core, type	Date (April 1997)	Time (GMT)	Interval (mbsf)	Length cored (m)	Length recovered (m)	Recovery (%)
173-1065A-						
(Drilled)	24	0815	0.0-251.0	0.0	0.00	NA
1R	24	1040	251.0-260.7	9.7	6.12	63.1
2R	24	1300	260.7-270.3	9.6	2.59	27.0
3R	24	1515	270.3-280.0	9.7	2.95	30.4
4R	24	1720	280.0-289.6	9.6	6.78	70.6
5R	24	1955	289.6-299.2	9.6	1.75	18.2
6R	24	2225	299.2-308.8	9.6	3.45	35.9
7R	25	0050	308.8-318.5	9.7	0.07	0.7
8R	25	0315	318.5-328.1	9.6	0.14	1.5
9R	25	0620	328.1-337.7	9.6	0.65	6.8
10R	25	1010	337.7-347.3	9.6	0.37	3.9
11R	25	1240	347.3-356.8	9.5	0.23	2.4
12R	25	1545	356.8-366.4	9.6	0.09	0.9
(Drilled)	25	1820	366.4-371.0	0.0	0.00	NA
13R	25	2040	371.0-376.0	5.0	0.47	9.4
14R	25	2340	376.0-385.7	9.7	0.30	3.1
15R	26	0210	385.7-395.3	9.6	0.09	0.9
16R	26	0430	395.3-404.9	9.6	0.33	3.4
17R	26	0915	404.9-424.2	19.3	0.74	3.8
18R	26	1445	424.2-443.5	19.3	0.58	3.0
19R	26	2030	443.5-462.9	19.4	0.08	0.4
20R	26	2330	462.9-466.5	3.6	0.11	3.1
21R	27	0425	466.5-482.2	15.7	0.01	0.1
22R	27	1200	482.2-501.5	19.3	0.77	4.0
23R	27	1900	501.5-520.8	19.3	0.83	4.3
24R	27	2345	520.8-530.4	9.6	0.95	9.9
25R	28	0305	530.4-540.0	9.6	0.11	1.1
26R	28	0630	540.0-549.7	9.7	0.63	6.5
27R	28	1040	549.7-559.3	9.6	3.01	31.4
28R	28	1445	559.3-568.9	9.6	0.93	9.7
29R	28	1835	568.9-578.5	9.6	1.29	13.4
30R	28	2215	578.5-588.1	9.6	1.65	17.2
31R	29	0230	588.1-597.7	9.6	2.73	28.4
32R	29	0600	597.7-607.4	9.7	1.69	17.4
33R	29	1035	607.4-617.1	9.7	2.44	25.2
34R	29	1530	617.1-626.7	9.6	1.25	13.0
35R	29	1820	626.7-631.4	4.7	0.38	8.1
			Cored totals	375.8	46.56	12.4
			Drilled	255.6		
			Total	631.4		

An expanded version of this table with individual section lengths is on the CD-ROM (back pocket, this volume).

tion of lithostratigraphic units during Leg 173 took into account the lithostratigraphy defined during Leg 149. At Site 900, 23 km west-southwest of Site 1065, Subunit IIA is early Miocene in age, and it consists predominantly of nannofossil claystone and chalk containing significant amounts of siliceous allochems (Shipboard Scientific Party, 1994c). At Site 1065, nannofossil chalk dominates the lower Miocene section, which also contains siliceous allochems. However, the sediments differ significantly from those of Subunit IIA at Site 900, because they are deformed by slump folds and contain pebbles composed of probably Hercynian basement rocks and Upper Jurassic/Lower Cretaceous shallow-water limestones. They cannot be directly equated with Subunit IIA at Site 900, therefore, and so for simplicity we designated the slumped nannofossil chalks at Site 1065 as Unit II.

The Middle–Upper Jurassic succession is similar to that drilled at Site 901, 21 km east-southeast of Site 1065, where it was designated as Unit II, following the normal ODP protocol of numbering units sequentially from the top downward (Shipboard Scientific Party, 1994d). As the Upper Jurassic sedimentary sections at Sites 901 and 1065 are older than the Aptian sediments and gravity transported mantle material designated as lithostratigraphic Unit IV at Sites 897 and 899 (Shipboard Scientific Party, 1994a, 1994b), we chose to identify the Upper Jurassic succession at Site 1065 as lithostratigraphic Unit V.

Rotary coring (RCB) was employed in Hole 1065A, resulting in moderate recovery of the sediments of Unit II (41%) and very poor recovery of Unit V (8%), particularly in the upper part, which is presumed to be dominated by soft clays. Coring began within Unit II at 251 mbsf and terminated in Unit V at 631.4 mbsf. Figure 6 summarizes the core recovery, lithologies, and ages of the lithostratigraphic units recognized in Hole 1065A. The ages, lithologic compositions, overall colors, facies and depositional environments, boundary depths, and cored intervals of Units II and V are summarized in Table 2. Lack of precise biostratigraphic information precluded drafting of an age vs. depth plot.

Unit II

Cores 173-1065A-1R-1, 0 cm, through 6R-CC, 23 cm
Depth: 251.0–308.8 mbsf
Age: early Miocene

General Description

Recovery of Unit II over the 57.8 m drilled section was 41%. Core disturbance is generally slight, but some short intervals (10–20 cm) of flow-in and biscuiting are present, and in 173-1065A-3R-1, 0–45 cm, washed material is present in which pebble-sized basement clasts are concentrated.

Light greenish gray nannofossil chalk forms about three-quarters of the drilled section of Unit II. The remainder consists of darker colored (greenish gray, dark greenish gray, dark gray) sediments: nannofossil claystone, clayey nannofossil chalk, and nannofossil chalk with clay.

The uppermost 2.88 m of the cored section (173-1065A-1R-1, 0 cm, to 1R-2, 138 cm) consists mostly of nannofossil chalk, which is almost structureless (possibly intensely bioturbated). The rest of this interval consists of alternating nannofossil chalk and slightly darker clayey nannofossil chalk occurring as thinly bedded or laminated intervals 2–15 cm thick. Extensional microfaults occur at the top of Section 1065A-1R-1 and are described in the "Structural Geology" section, this chapter.

The remainder of Unit II (interval 173-1065A-1R-2, 138 cm, to 6R-CC) is deformed by slump folding and subsidiary extensional and compressional faulting (see "Structural Geology" section, this chapter). Sedimentary successions similar to those described in the previous paragraph occur in the folded interval. In addition, there are intervals of darker, more clay-rich sediments ranging in thickness between 4 cm and 1 m. They are thinly bedded, wavy and parallel laminated, with low to intense bioturbation and occasional upward-darkening intervals up to 10 cm thick. It is possible that the apparently structureless intervals are the result of intense bioturbation. *Chondrites*, *Teichichnus*, and *Zoophycos* are common ichnofossils.

A feature of Unit II at Site 1065 that was not found in any of the Leg 149 holes is the presence of granules and pebbles "floating" in nannofossil chalks and claystones (Fig. 7). These clasts range in size from 2 to 40 mm and are composed of lithologies characteristic of the Iberian Hercynian basement and shallow-water limestones (see "Petrography" section below). No finer siliciclastic or lithoclastic sand material was observed in the sediments around the pebbles. The granule- to pebble-sized clasts are most common in the first core (173-1065A-1R); they are scattered through the remaining cores at intervals of 0.5–3 m.

Petrography

Smear-slide analyses (see Section 4, CD-ROM, back pocket, this volume) revealed that all the lithologies present in Unit II contain siliceous allochems at trace and rare levels. Quartz is present at trace or rare levels of abundance in all the clayey lithologies.

X-ray diffraction analyses of 13 samples from Unit II confirm the mineralogy determined by smear-slide analysis. The dominant mineral component is calcite, with minor amounts of quartz, dolomite, and unidentifiable clay minerals. Bulk carbonate analyses also indicate that the composition of Unit II is dominantly calcium carbonate

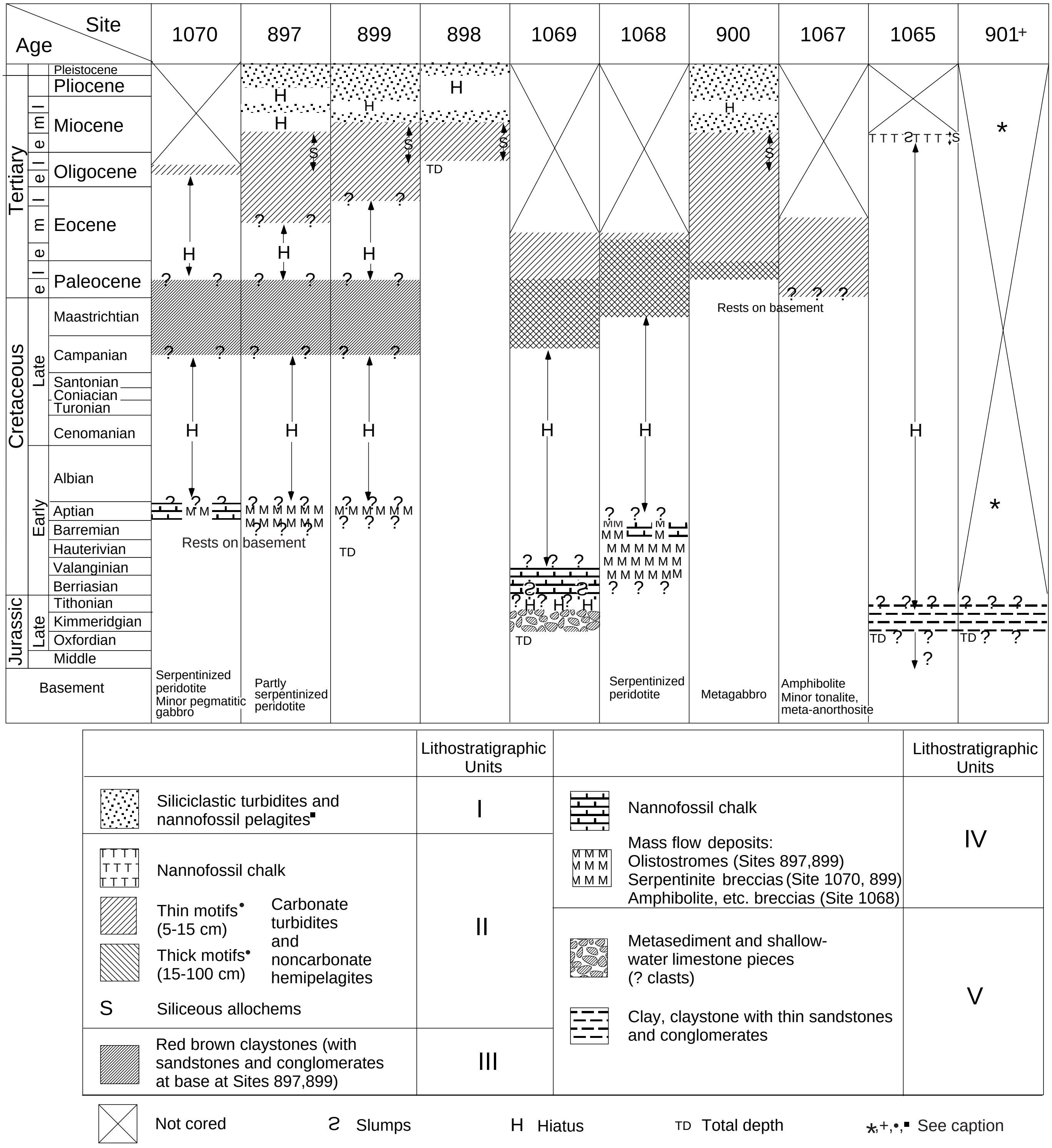

Figure 5. Simplified summaries of stratigraphic successions cored at Leg 149 and Leg 173 sites. Unit III is almost barren of fossils and so its age is very uncertain. + = Unit V as shown in Site 901 was designated by Shipboard Scientific Party (1994d) as Unit II, following the normal ODP practice of numbering units sequentially downhole; * = a washed core recovered Miocene nannofossil ooze and a 5-mm-thick layer of gray clay of Aptian age. Solid square = nannofossil pelagites dominant at Site 900. Solid circles = "Motifs" refers to types of upward-darkening sequences shown in Figure 2 of the "Site 1068" chapter and Figure 8 of the "Site 1069" chapter (both this volume). The cross-hatched symbols on the summary chart indicates that both thin (Motif 2) and thick (Motif 1) sequences are present.

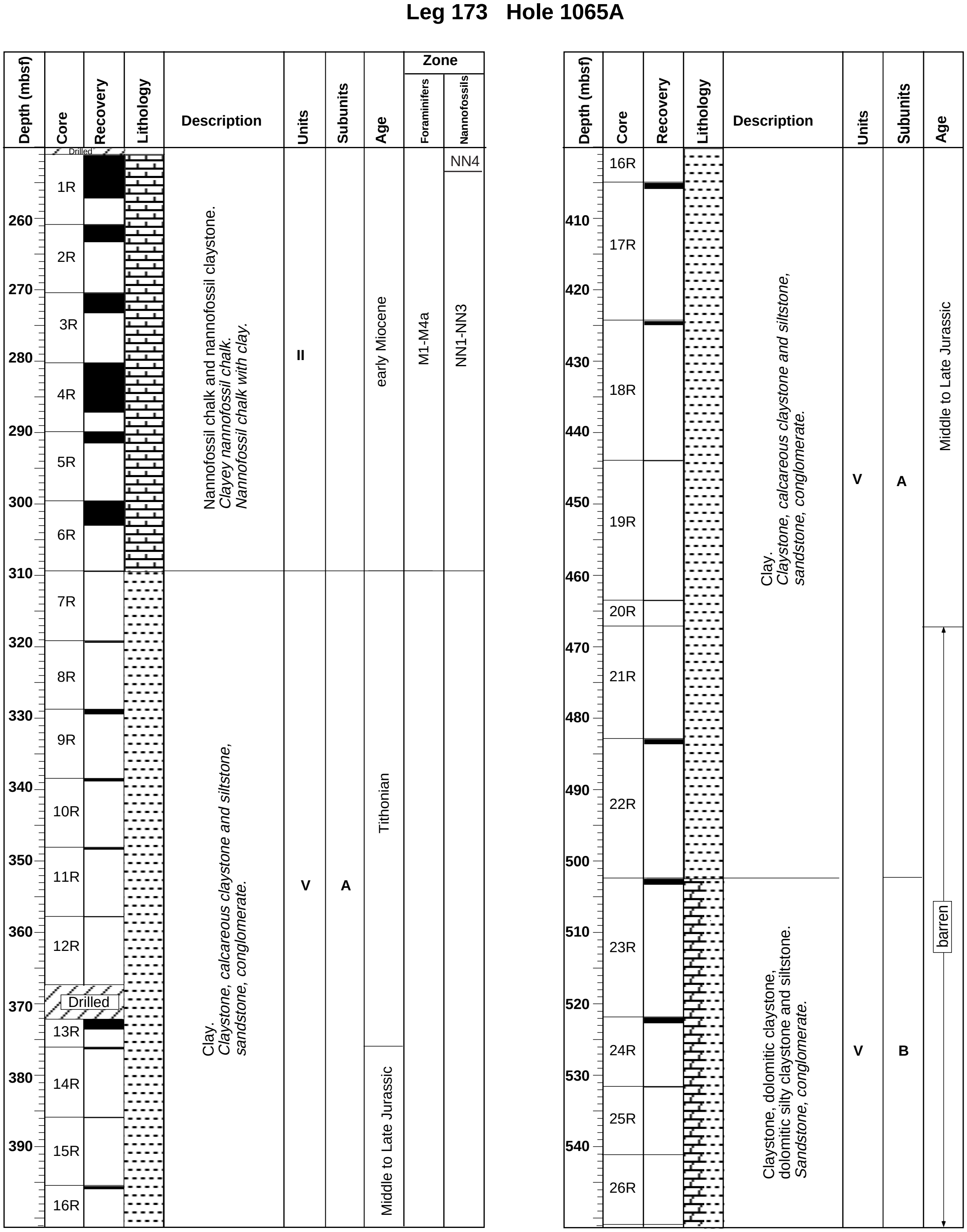

Figure 6. Summary lithostratigraphic column for Site 1065. Minor lithologies are listed in italics. (Continued next page.)

(see Fig. 24, "Organic and Inorganic Geochemistry" section, this chapter).

The results of thin-section studies of nine pebbles from Unit II are summarized in Table 3, and photomicrographs of some of the thin sections are shown in Figure 8. Three groups of clasts are recognized: (1) metamorphosed siliciclastic sedimentary rocks, (2) higher grade metamorphic rocks, and (3) shallow-water limestones.

Depositional Processes

The nannofossil chalk and claystone of Unit II were deposited from suspension as pelagites and hemipelagites. It is possible that some deposition may have occurred from low-density turbidity flows. The seismic section across Site 1065 (Fig. 3) shows that these sediments were deposited near the crest of a tilted fault block on a

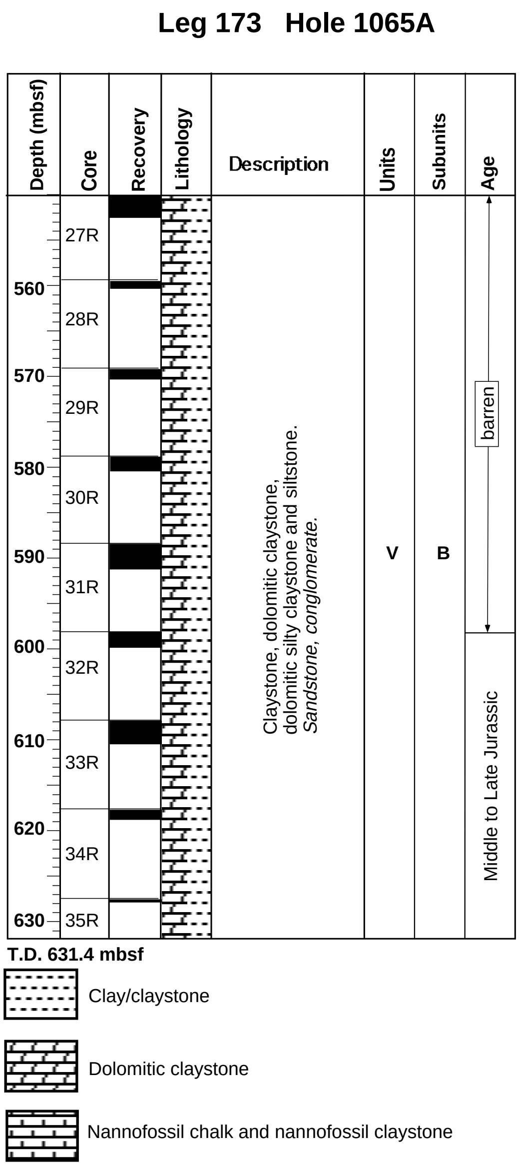

Figure 6 (continued).

eastward-inclined slope with a dip of ~5°. Accumulations of mud grade sediment are inherently unstable, and, on such a relatively steep slope, slumping would not necessarily require external triggering mechanisms such as earthquakes.

The pebbles of basement and shallow-water limestones indicate that pre-Miocene rocks were being eroded from nearby areas of the western Iberia continental margin. The metamorphosed sediments are broadly similar to dredged samples described from Vasco da Gama Seamount by Capdevila and Mougenot (1988) and from the west Galicia margin by Mamet et al. (1991). Vasco da Gama Seamount is situated 30 km northwest of Site 1065, and the dredged samples obtained here include phyllites with interbedded arkoses. The pebbles of metamorphosed sediment in Unit II at Site 1065 consist of slate and of lithic sandstone that contains small amounts of feldspar. None of the dredged samples obtained by Capdevila and Mougenot (1988) from the west Iberia margin is fully comparable with the biotite hornfels and coarse-grained porphyroblastic mica schist obtained at Site 1065, although Capdevila and Mougenot report the presence of fine-grained mica schist with biotite porphyroblasts from the northwest slope of Galicia Bank.

The limestones and their constituent allochems are similar to Tithonian limestones drilled off Galicia Bank during ODP Leg 103 (see Table 3; Fig. 8; Jansa et al., 1988). It is likely, therefore, that a Tithonian carbonate platform, similar to that described by Jansa et al. (1988), developed over what is now Vasco da Gama Seamount and over the ridge to the east of it (Fig. 4).

The most likely mechanism to have transported the pebbles from the region of Vasco da Gama Seamount and deposited them at Site 1065 is turbidity flow. However, such powerful flows should also have reached Site 900, yet no pebbles were found in Unit II at this site during Leg 149. We have no explanation for this paradox.

How did the pebbles become scattered through some intervals of the nannofossil chalks and claystones without being accompanied by sand-grade material that pebble-laden density flows must have carried? The answer to this question lies in the likely fluid properties of the slumped sediments during and immediately after their movement.

In addition to the faulting, folding, and variably developed cleavage system described in the "Structural Geology" section, this chapter, the slumped nannofossil chalks show millimeter- to centimeter-scale features including boundaries between layers, undulatory fold-like banding, discordant banding, and fractal structures such as dendrites and cauliflower structures. These self-organized structures, in association with the larger scale structures indicative of soft sediment deformation, suggest that the sediments behaved as a non-Newtonian fluid before lithification. Viscosity gradients across the slumped intervals, with viscous fingering and other surface tension mediated effects, arise through fluids of differing viscosity and yield strengths pushing across unstable interfaces (Viscek, 1989).

The inferred existence of a viscous medium subjected to progressive dewatering can account for the presence of pebbles floating in nannofossil sediments and the absence of a sand fraction that must have been transported to Site 1065 with the larger clasts. It is possible that the pebbles in the postulated overlying turbidite were able to exceed the yield strength of the antecedent nannofossil ooze, whereas the finer grained material remained at the turbidite/ooze interface. The downward movement of the pebbles was arrested when dewatering of the ooze reduced its viscosity and increased its yield strength.

Unit V

Cores 173-1065-7R-CC, 0 cm, through 35R-CC, 18 cm
Depth: 308.8–631.4 mbsf
Age: Middle–Late Jurassic (Tithonian)

General Description

Sediments in Unit V are greenish gray in color and consist dominantly of clay grade sediments. The top of Unit V is defined by the first occurrence of gray claystone in Section 173-1065A-7R-CC. As this lithology comprises one of only three pieces recovered in this core, the top of Unit V is arbitrarily placed at the top of Core 173-1065A-7R.

Unit V is divided into two subunits: Subunit VA is 192.7 m thick, and Subunit VB is >129.9 m thick. Plastic clay dominates the recovered material in Subunit VA, whereas in Subunit VB, claystone is the most common lithology. Core recovery of Subunit VA was extremely low (3%). The first appearance of claystones and dolomitic claystones defines the top of Subunit VB at interval 173-1065A-23R-1, 0 cm (501.5 mbsf); core recovery was 14%. Drilling was terminated in this subunit at 631.4 mbsf (Core 173-1065A-35R-CC, 18 cm).

Subunit VA

Plastic dark greenish gray clay is the main lithology recovered. *Chondrites* are present over most of the cored intervals, and the abundance of these ichnofossils generally decreases upward over intervals ranging in thickness from 10 to 20 cm. Minor lithologies include fine-grained limestone, calcareous claystone and siltstone, medium to coarse-grained sandstone, and conglomerate. Parallel laminae occur

Table 2. Summary of lithostratigraphic Units II and V in Hole 1065A.

Lithostratigraphic unit/subunit	Age	Thickness* (m)	Major lithology† *Minor lithology*†	Color	Facies *Environment* (total meters described)	Depth (mbsf)	Occurrence
II	early Miocene	>57.8**	Nannofossil chalk >80% *Nannofossil claystone <10%* *Clayey nannofossil chalk <5%* *Nannofossil chalk with clay <5%*	Light greenish gray/grayish green	Slumped pelagites and hemipelagites/low density muddy turbidites *Foot of continental rise/crest of tilted fault block* (20.20)	Top = 251 Base = 308.8**	1R-1 at 0 cm 6R-CC at 23 cm
VA	Tithonian/Middle to Late Jurassic	192.7	Clay *Fine-grained limestone* *Calcareous claystone and siltstone* *Sandstone* *Conglomerate*	Dark greenish gray/medium dark gray	Sub-wave base suspension deposits and minor turbidites *Offshore shelf* (5.03)	Top = 308.8 Base = 501.5	7R-CC at 0 cm 22R-CC at 22 cm
VB	Middle to Late Jurassic	>129.9	Claystone/dolomitic claystone Dolomitic silty claystone and siltstone *Sandstone* *Conglomerate*	Dark greenish gray/medium dark gray	Sub-wave base suspension deposits and minor turbidites *Offshore shelf* (17.89)	Top = 501.5 Base = 631.4	23R-1 at 0 cm 35R-CC at 18 cm

Notes: See Figure 5 for explanation and correlation of lithostratigraphic units in the Leg 149/173 area. * = minimum thickness, as drilling commenced in Unit II, and terminated before the base of Unit V was reached. † = Proportions of lithologies not given for Unit V, as recovery was very low. ** = depth of base uncertain, as the only samples recovered in Core 7R were pieces of sedimentary rock in the core catcher.

in the clays and are common in the siltstones; many of them contain black plant debris.

Beds of the coarse lithoclastic sand and conglomerate are 3–7 cm thick. The lithoclasts in the conglomerates reach 10 mm in size. The lithoclasts are composed of either gray pelite or light colored limestone; both clast types are subangular to subrounded. Similar conglomerates occur in Subunit VB (Fig. 9A, B), but except for the example shown in this figure, they are less than one centimeter thick. In interval 1065A-22R-CC, 15–22 cm, the limestone lithoclasts are darker colored because they have been dolomitized (Fig. 9E, F).

Subunit VA is similar to Unit II (which is Tithonian in age) at Site 901. However, the lithoclastic coarse sand and conglomerate present at Site 1065 are not present at Site 901 (Shipboard Scientific Party, 1994d). At the latter locality, greenish and olive gray parallel laminated sandstones form about 10% of the cored interval of Unit II.

Subunit VB

Subunit VB consists dominantly of claystone and dolomitic claystone; the plastic clay characteristic of Subunit VA was not recovered. In addition, only very thin (<2 cm) beds of coarse sand and conglomerate occur, with the exception of a 7-cm-thick bed in Core 173-1065A-23R-1, 36–42.5 cm (Fig. 9A, B).

In parts of the cores, the claystone and dolomitic claystone contain up to 30% silt. Figure 10 shows the key features present in these lithologies. Most of the cored intervals consist of sharp-based thin beds of claystone or dolomitized claystone (1–20 cm thick), with *Chondrites* burrows that are filled with darker sediments. The *Chondrites*-rich intervals are sometimes interbedded with thin bedded to laminated alternations of lighter and darker claystone/dolomitized silty claystones/silty dolomitic claystones, or dolomitic siltstones. The contact between the *Chondrites*-rich and overlying thin bedded/laminated intervals is gradational over a distance of a few millimeters, and in places it is clear that this contact is the result of burrowing (Fig. 10).

Siltstones and fine sandstones occur either as thin beds or as single laminae. Some of these beds contain faint cross stratification (Fig. 10). The bases of some of the silty and sandy beds are erosional (Fig. 10). Rare lenticular laminae containing faint cross-lamination and wavy laminae suggest the presence of wave ripples (Fig. 10). Only one bed of coarse sand and conglomerate comparable in thickness to those present in Subunit VA was recovered from Subunit VB (Fig. 9), but several very thin beds and laminae of this lithology occur in the cores.

A slump-folded interval occurs in Section 173-1065A-33R-1, 55 cm, to 33R-2, 10 cm (see “Structural Geology” section, this chapter).

Petrography

Inspection of smear slides indicates that quartz is present in trace to rare amounts in the clay and claystone of Unit V, rising to common in more silty lithologies. In some samples, mica occurs at the trace to rare level. The claystone typically contains trace to rare proportions of pyrite and plant debris (much of which is charcoal). Trace levels of nannofossils occur in the clays of Subunit VA.

X-ray diffraction analysis of Unit V claystone lithologies indicate that quartz, feldspar, and clay minerals, including illite and possibly chlorite, are common mineral components. Variable amounts of dolomite and calcite are also present with dolomite occasionally dominating the mineralogy (e.g., Core 1065A-23R), suggesting that some of the claystone and silty claystone of Unit V has undergone dolomitization. Results of bulk carbonate analyses (see Fig. 24, “Organic and Inorganic Geochemistry” section, this chapter) and thin section analyses support this conclusion. In the latter case a spectrum of lithologies was observed, from carbonate-free claystones, through mixtures of clay and dolomite, to completely dolomitized sediments in which quartz siltstone clasts float in a mosaic of dolomite crystals about 0.05 mm across. Some of the claystones contain mica flakes about 0.01 mm long, oriented parallel to bedding.

The thin beds of coarse sand and the conglomerates contain two dominant lithoclast types: (1) slates, metasiltstones and lithic arenites, and (2) shallow-water limestones showing similar variety of compositions to the limestone clasts in Unit II described in Table 3. The spaces between the larger clasts in the conglomerates contain subangular single and polycrystalline quartz grains and subangular to rounded carbonate allochems, some of which are pyritized. The space between these smaller clasts is cemented by sparry calcite. Both the conglomerates and coarse sands were well compacted before calcite cementation, as there are long intergrain contacts between the closely packed clasts, but very little grain contact solution. A conglomerate interval at 173-1065A-22R-CC, 15–22 cm, contains a sparry dolomite cement, and the limestone clasts are dolomitized.

Depositional Processes

The sediments of Unit V are dominantly suspension deposits. The features illustrated in Figure 10 suggest that all the silt and much of the clay material was transported and deposited by low-density tur-

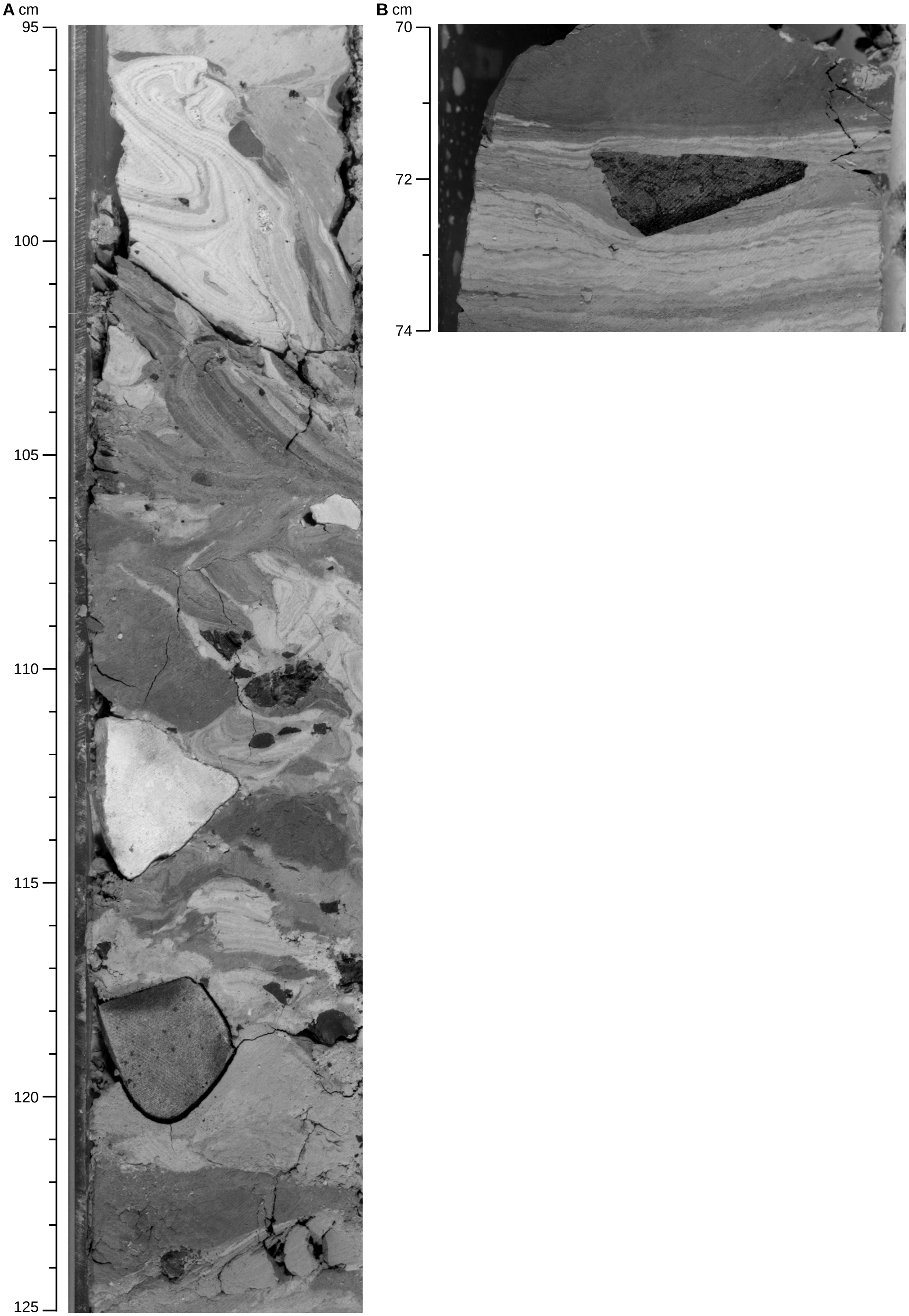

Figure 7. Matrix-supported pebbles in nannofossil chalks and claystones of Unit II at Site 1065. **A.** Interval 173-1065-1R-3, 95–125 cm. Dark (basement-derived) and light (shallow-water limestone) pebbles in nannofossil chalks and claystones highly deformed by slumping. Pebble at 111–115 cm: partially cemented peloidal/intraclastic grainstone; at 117.5–120.5 cm: pelitic hornfels with biotite porphyroblasts (darker spots). Most of the smaller darker clasts are probably either composed of slate or fine-grained lithic graywacke. **B.** Interval 173-1065-6R-2, 70–74 cm. Angular pebble of biotite schist “floating” in nannofossil chalk (lighter) and clayey nannofossil chalk (darker).

Table 3. Summary of observations made on thin sections of pebbles occurring in Unit II at Site 1065.

Core, section, interval (cm)	Rock name	Comments	Figure 8 photomicrograph	Description
173-1065A-				
1R-2, 139-141	Lithic graywacke	Low-grade metamorphism	A	Fine-grained sand; angular clasts; moderately sorted. Clasts dominated by single and polycrystalline quartz grains; most quartz shows shadow extinction. Rare feldspar (plagioclase). Matrix forms 0-20%: micas and clay minerals. Minimal grain contact solution.
1R-3, 4-7	Metamorphosed lithic arenite	Low-grade metamorphism	B	Medium sand; angular clasts. Clasts dominated by single and polycrystalline quartz grains; most quartz shows shadow extinction. Rare feldspar (plagioclase). Matrix ~10%: micas and clay minerals; some grain contact solution.
1R-3, 73-75	Carbonate mudstone			Micrite with scattered foraminifers.
1R-3, 85-88	Peloidal/intraclastic grainstone		C	Allochems medium- to coarse-sand grade. Part of thin section shows microspar cement; intra-particle porosity preserved elsewhere, save for calcite overgrowths around echinoderm plates.
1R-3, 111-115	Peloidal packstone	Cryptalgal structure: possible boundstone	D and E	Peloids fine- to medium-sand grade. Long colonial coral fragment traverses slide, and is encrusted by a variety of algae, and a chaetitid.
1R-4, 34-37	Pelite	Low-grade metamorphism		Very fine-grained quartz, clay minerals and mica (muscovite).
6R-1, 84-86	Mica schist	Greenschist facies metamorphism	F	Quartz: ~50%; muscovite: ~30%; biotite: ~10%. Fairly strong foliation defined by muscovite alignment; biotite porphyroblasts.
6R-2, 30-32	Pelite	Low-grade metamorphism		Similar to 1065A-1R-3, 111-115 cm, but red (?hematite) iron staining.
14R-CC, 0-2	Biotite hornfels	Contact metamorphism		This clast is within Subunit VA, but was probably washed downhole from Unit II. ~10% biotite porphyroblasts. Matrix crystal size ~0.01 mm; largely white mica with minor quartz. Relict foliation. Original rock may have been a slate.

bidity currents, although a hemipelagic origin cannot be ruled out for some of the sediment. The sharp-based silt and clay layers, and the erosive bases of the former, are indicative of turbidites. Cross and parallel laminae shown in Figure 10 are characteristic of turbidite units Tc and Td, respectively.

The abundance of *Chondrites* and other ichnofossils, and the absence of body fossils is indicative of disaerobic bottom conditions. The absence of wave-ripple lamination, apart from rare possible occurrences such as those illustrated in Figure 10, indicates deposition below wavebase in an offshore shelf setting. The clay/claystone facies of Unit V is broadly comparable to the Kimmeridgian Abadia formation of the onshore Lusitanian Basin, which is interpreted as a slope deposit on the basis of its sedimentological features and clinoform seismic reflection geometry (Leinfelder and Wilson, 1989, in press; Ravnås et al., 1997; Wilson et al., 1989).

It is probable that the beds of lithoclastic sand and conglomerate were also deposited by turbidity flows, as some are graded and show a graded sand cap (Fig. 9). The presence of slate and meta-arenite lithoclasts in the conglomerates indicates exposure and erosion of Variscan basement rocks, presumably to the north in the Vasco da Gama Seamount area (see previous discussion of “Depositional Processes” subsection for Unit II, this section, this chapter). The lithoclasts of shallow-water limestones exhibiting lithologies similar to those recovered during Leg 103, described by Jansa et al. (1988), suggest that limestones slightly older than Unit V were being eroded, or that contemporaneous carbonate buildups located on tectonic highs were shedding debris into the area around Site 1065. The latter scenario is similar to that described by Leinfelder and Wilson (1989, in press) for Kimmeridgian sediments filling the Arruda Sub-basin 30 km to the north of Lisbon.

BIOSTRATIGRAPHY

Calcareous microfossils are moderately to well preserved and abundant in the lower Miocene chalks of lithostratigraphic Unit II but are virtually absent in some intercalated siliceous claystones such as in interval 173-1065A-2R-CC, which is dominated by abundant sponge spicules together with rare radiolarians. Relatively undisturbed chalks in the first two sections of Core 173-1065A-1R cap the underlying slump complex (see “Lithostratigraphy” section, this chapter) and, as such, provide a minimum date for its time of emplacement of ~16.7 Ma, based on the absence of middle Miocene planktonic foraminifer index taxa. These overlying sediments are assigned to the planktonic foraminifer Zone M4a and nannofossil Zone NN4. The slump complex extends down through Core 173-1065A-6R and involves sediment mainly from the long-ranging nannofossil Zone NN2, but it may well include a complete suite of lower Miocene strata from NN1 to NN3 (or planktonic foraminifer Zones M1 to M3).

A yellowish sandy claystone recovered in the core catcher of Core 173-1065A-7R was barren of microfossils. This highly oxidized material could be nonmarine, possibly from the Cretaceous or uppermost Jurassic, both of which are missing as a result of a major hiatus and/or the poor recovery in Core 173-1065A-7R.

Small numbers of moderately to well-preserved nannofossils provide a Tithonian age for the upper portion of sediments in lithostratigraphic Unit V (Cores 173-1065A-8R to 13R), but only long-ranging taxa are present down to Core 173-1065A-20R. A 132-m barren interval separates this core from the lower 33 m of the hole, which contains dissolution-resistant nannofossils that may have been introduced with turbidites. These constrain the bottom of the section to only Middle to Late Jurassic in age, an assignment that could be considerably improved by further shorebased palynology (see Appendix, this chapter). Calcareous benthic foraminifers are very rare and occasionally pyritized within these older clastic sediments, which also contain rare, sporadic occurrences of poorly preserved, indeterminate agglutinated foraminifers.

Planktonic Foraminifers

Planktonic foraminifers were only recovered in situ from the upper part of the cored section at Hole 1065A and are characteristic of early Miocene faunas (see Table 4). Cores 1065A-1R through 5R yielded assemblages of abundant, moderately diverse, well-preserved planktonic foraminifers. The stratigraphically highest sample analyzed was interval 173-1065A-1R-1, 81–85 cm, which is dominated by species characteristic of Zone M4a (late early Miocene), including abundant *Globigerinoides trilobus, Globoquadrina dehiscens,* and *Globoquadrina venezuelana.* Species indicative of Zone M5 (middle Miocene), such as *Praeorbulina glomerosa curva* and

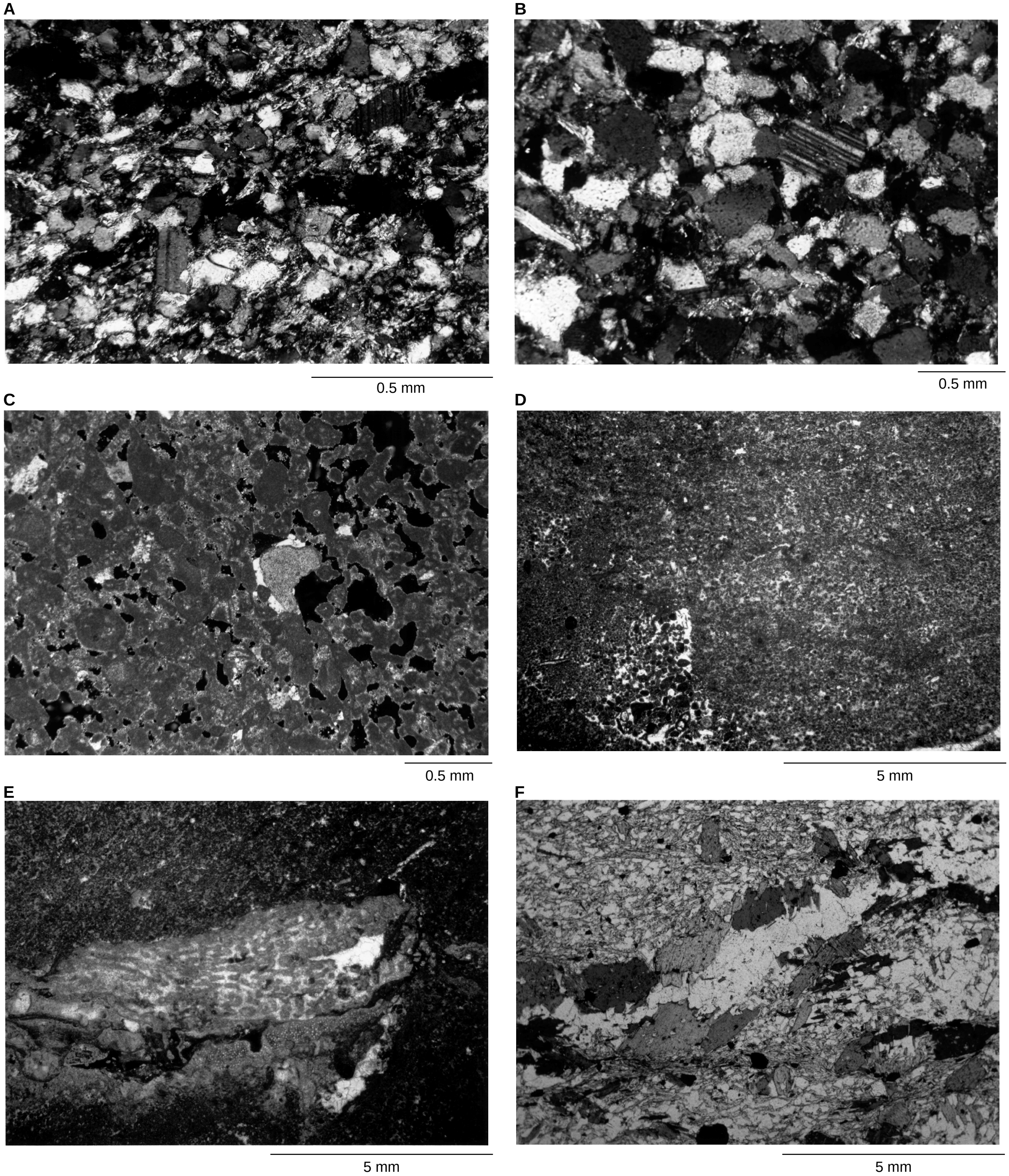

Figure 8. Photomicrographs of thin sections of pebbles occurring in Unit II in Hole 1065A. **A.** Lithic graywacke, 173-1065A-1R-2, 139–141 cm. Crossed polars. Single and polycrystalline quartz clasts, with rare feldspars, set in a matrix of clay minerals and sericitic mica. **B.** Lithic arenite. Sample 173-1065A-1R-3, 4–7 cm. Crossed polars. Single and polycrystalline quartz clasts, with rare feldspars, showing grain contact solution, and some sericitic micas between the clasts. **C.** Intraclast/peloidal grainstone. Sample 173-1065A-1R-3, 85–88 cm. Crossed polars. The limestone is partially cemented by finely crystalline cement, and syntaxial calcite overgrowths over echinoderm plates (slightly right of center). Black areas are primary porosity. **D, E.** Peloidal packstone/boundstone, Sample 173-1065A-1R-3, 111–115 cm. Plane polarized light. (D) shows typical texture of this pebble: the slightly layered "clotted" texture is typical of Late Jurassic low-energy carbonate build-ups occurring onshore in Portugal. (E) shows part of a fragment of a colonial coral coated with a variety of encrusting organisms. **F.** Porphyroblastic biotite schist. Sample 173-1065A-6R-1, 84–86 cm. Plane polarized light. Pleochroic biotite shows as darker minerals, encased in low-relief quartz.

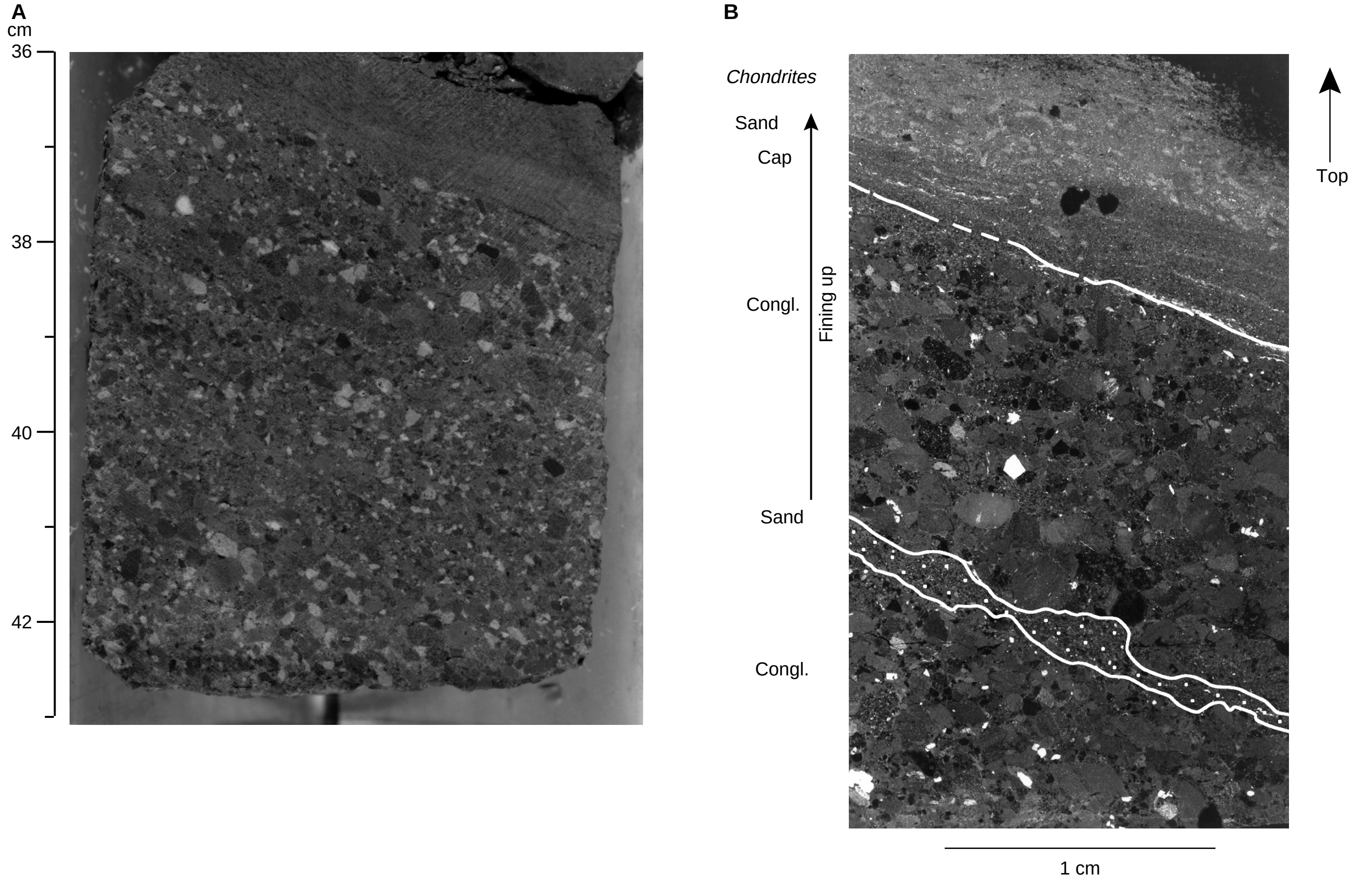

Figure 9. Lithoclastic conglomerates and sandstones cored in Unit V, Hole 1065A. **A.** Core photograph: interval 173-1065A-23R-1, 36–42.5 cm. Lighter lithoclasts are composed of shallow-water limestone; darker ones are predominantly slate. Note the thin sandstone cap to the conglomerate. **B.** Negative photograph of thin section taken between 37 and 41 cm on right side of Core 23R-1 shown in (A). Angular white areas are pyrite, and elongate white flecks are plant debris. A sand layer ~2 mm thick occurs in the lower part of the photograph: above it, the size of the lithoclasts diminishes upward. At the top of the photograph, laminae are present in the sand cap, and above this interval *Chondrites* burrows occur. (Continued next page.)

Praeorbulina transitoria or species characteristic of younger sediments at these latitudes, are not present in this sample. The age assignment is further reinforced by the occurrence of *Globorotalia peripheroronda* and the rare occurrence of *Catapsydrax stainforthi* and *Globigerinoides altiapertura.*

The occurrence in Sample 173-1065A-1R-CC of *Globorotalia kugleri*, *Catapsydrax dissimilis*, *Catapsydrax stainforthi* and a moderately diverse assemblage of *Globigerinoides* spp. suggests an early Miocene (Zones M1–M3) age for this sample and also for Samples 173-1065A-3R-CC, 173-1065A-4R-CC, and 173-1065A-5R-CC. Age index species needed to further define Zones M1, M2, and M3 were not recovered from these samples. Sample 173-1065A-2R-CC is barren of foraminifers and is dominated by abundant sponge spicules together with rare radiolarians. Rare, very poorly preserved, keeled Upper Cretaceous planktonic foraminifers are present in Samples 173-1065A-29R-CC and 173-1065A-30R-CC and are interpreted as contamination from unknown sources.

Benthic Foraminifers

Common, well-preserved, calcareous benthic foraminifers are present throughout the lower Miocene sediments analyzed from Site 1065A with the exception of Sample 173-1065A-2R-CC, which is barren of benthic foraminifers. In the older Jurassic samples (core-catcher samples below 310 mbsf) calcareous benthic foraminifers are very rare, occasionally pyritized, and not age-diagnostic. Rare, sporadic occurrences of poorly preserved, indeterminate agglutinated foraminifers are also recorded throughout this interval (310–631.4 mbsf).

Calcareous Nannofossils

Coring for Hole 1065A was expected to begin in Miocene sediments and to proceed into Mesozoic sediments before reaching acoustic basement. A detailed Oligocene–Miocene nannofossil biostratigraphy for this immediate area on the Iberia Abyssal Plain had previously been rendered by de Kaenel and Villa (1996); thus, a seamless tie-in to their stratigraphy was expected. Not expected was the massive and convoluted slump complex encountered in the six Miocene cores recovered at this site, which complicated the biostratigraphy.

The top two sections of nannofossil chalk in Core 173-1065A-1R postdate the slumped interval and are therefore relatively undisturbed, cut only by minor brittle fractures with minimal displacements (2–3 mm). Within those two sections, five samples examined between 173-1065A-1R-1, 25–26 cm, and 173-1065A-1R-2, 126–128 cm, contain *Sphenolithus heteromorphus* (few to common) which, combined with *Helicosphaera ampliaperta* in Sample 173-1065A-1R-1, 123–124 cm, delineate Zone NN4 for this part of the section. The assemblages are dominated by abundant *Coccolithus pelagicus*, *Cyclicargolithus floridanus,* and a host of small reticulofenestrids. *Cyclicargolithus abisectus* (>10 µm) is present, as are robust *Coronocyclus nitescens.* Discoasters are abundant, but heavily overgrown, preventing recognition of species. *Triquetrorhabdulus*

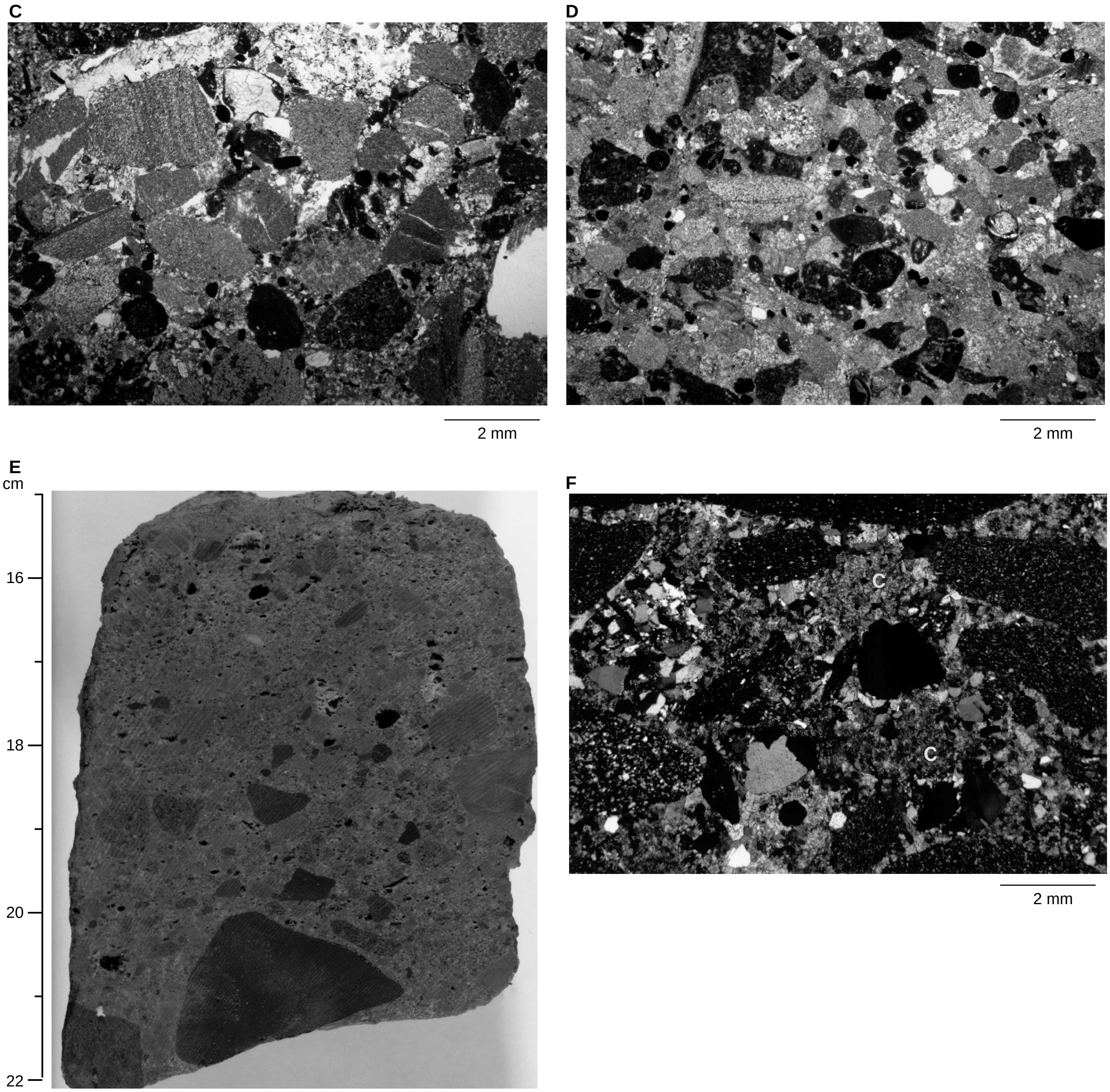

Figure 9 (continued). **C.** Photomicrograph, Sample 173-1065A-8R-CC, 4–7 cm. Lithoclast conglomerate. Light gray, angular to subrounded, very fine-grained clasts consist of pelites; darker grains are composed of limestone, most of which are peloidal or intraclast packstones. At top left of the photograph, an elongate bivalve fragment occurs above a banded pelite clast. The clasts are closely packed and some show grain contact solution. They are cemented by sparry calcite, within which quartz clasts occur. **D.** Photomicrograph, Sample 173-1065A-8R-CC, 8–10 cm. Lithoclastic coarse sand. The clast composition is similar to that shown in (C). The black rounded grains are probably pyritized limestone allochems. **E.** Core photograph: interval 173-1065A-22R-CC, 15–22 cm. This conglomerate is similar to that shown in (A), but the limestone clasts have been dolomitized and so are only faintly visible within the dolomitic matrix (see Fig. 9F). **F.** Photomicrograph, Sample 173-1065A-22R-CC, 16–21 cm. Crossed polars. Speckled clasts are pelitic, and black areas are probable pyritized limestone clasts. The cement is dolomite; larger areas of dolomite labeled “C” are dolomitized limestone clasts.

milowii (few in number) are moderately overgrown but quite recognizable. Otherwise, the assemblages are well preserved. The only sign of reworking in these samples was a single specimen of *Sphenolithus belemnos* in Sample 173-1065A-1R-2, 11–14 cm.

Small to large clasts of exotic material in the nannofossil chalks beginning at about the level of Sample 173-1065A-1R-2, 126–128 cm, denote the top of the disturbed interval. Three samples from the top, bottom, and middle of Section 173-1065A-2R-2 within the slump, however, were essentially barren of nannofossils. Most of the nannofossils that were present appeared to be contaminants since they include overgrown discoasters, forms that would normally be well preserved in such a silica-rich sediment. Sponge spicules are particularly prevalent in this lithology.

Cores 173-1065A-3R through 6R (plus one pebble-sized piece from 173-1065A-7R-CC) contain lithologies ranging from carbonate-rich gray nannofossil chalks in which coccoliths are moderately preserved (from overgrowths on the discoasters) to dark green silty claystones in which nannofossil preservation is very good and abundances are moderate. These lithologies are often intimately interbedded as laminae or thin layers that may be folded together within the slump(s), or they may be separated within the core as discrete, isolated pieces for which the original depositional relationships have been obscured by slumping and/or drilling disturbance. A precise age determination for all of the components within the slump mass will require that many more samples be examined, in addition to the core-catcher samples that were examined here.

Core-catcher Samples 173-1065A-3R to 6R are assigned primarily to Zone NN2 based on the presence of few to rare *Discoaster druggii* in the presence of few *Triquetrorhabdulus carinatus.* More detailed sampling could well show a greater stratigraphic range of materials (from Zones NN1 to NN3) included within the slump(s). To date, however, no Oligocene strata have been identified.

As mentioned above, the dark green lithologies within the lower Miocene contain the best preserved nannofossils. Relative to the light-colored chalks, they also contain the most, or at least the most easily recognized, contaminants from older units. Such reworked nannofossils are seen in trace amounts rather consistently throughout the slumped interval. For instance, Sample 173-1065A-7R-CC, 5 cm, contained *Arckangelskiella cymbiformis* from the Upper Cretaceous, *Vekshinella stradneri, Cretarhabdus conicus, C. crenulatus* from the Cretaceous (undifferentiated), *Tribrachiatus orthostylus* from the lower Eocene, *Chiasmolithus grandis* from the middle Eocene, and *Micrantholithus attenuatus, M.* aff. *attenuatus, Reticulofenestra bisecta,* and *Braarudosphaera bigelowii,* which are probably all from the Eocene. Sample 173-1065A-6R-2, 70–71 cm, contained *Micula decussata, Tranolithus phacelosus, Prediscosphaera cretacea, Rotelaplillius lafittei,* and *Cribrosphaerella ehrenbergi,* which are probably mostly from the mid- to Upper Cretaceous.

Besides the one Miocene pebble mentioned above, Sample 173-1065A-7R-CC yielded a pebble of yellowish sandy claystone that was barren of nannofossils and that did not match any Cenozoic lithology recovered in the study area during previous expeditions.

Core 173-1065A-8R penetrated clastic marine sediments that contained small numbers of well-preserved Upper Jurassic nannofossils. This core, plus most subsequent cores down to Core 173-1065A-14R, contained *Stephanolithion bigotii* and/or *Conusphaera mexicana minor*. The latter taxon indicates a lower Tithonian age, and its presence would indicate the *Conusphaera mexicana* Zone of various authors. Core recovery was extremely poor, however, so it is impossible to know if upper Tithonian strata are present at this site.

Core 173-1065A-13R yielded only a small dolomitic pebble that was barren of nannofossils. Relative to the Tithonian section at nearby Site 901 (de Kaenel and Bergen, 1996), nannofossil abundance and diversity at Site 1065 was low. This could be caused in part by the low core recovery, which lessened the opportunity to detect nannofossiliferous samples. Some other taxa noted in the assemblages included *Zeugrhabdotus erectus, Z. embergeri, Minavetesina favula, Diazomatolithus galicianus, D. lehmanii,* and members of the *Ellipsagelosphaera/Watznaueria* plexus, in which the *Watznaueria* were dominant.

Stephanolithion bigotii could be traced in core catchers from Core 173-1065A-14R down to 1065A-20R, but *Conusphaera mexicana minor* was absent in this interval; thus, the interval cannot be assigned exclusively to the lower Tithonian. Watznauerids continued to dominate the ellipsagelosphaerids, which could indicate a Tithonian age (J. Bergen, 1997, pers. comm.); however, the paucity of nannoliths makes any such determination highly tenuous at this point. The interval from 173-1065A-21R-CC to 30R-CC was totally barren of nannofossils.

Traces of nannofossils reappear downhole in Section 173-1065A-32R-CC and consist only of the dissolution-resistant members of the *Ellipsagelosphaera*/*Watznaueria* plexus, in which the latter taxa are still dominant. Unlike the well-preserved condition of these forms noted higher in the hole, however, these specimens exhibit mostly broken or fragmented shields. This, plus the lack of more delicate taxa (such as podorhabdids) toward the top of the Jurassic section, might reflect transport in turbidity currents, evidence for which was noted in this lower part of the drilled section (see “Lithostratigraphy” section, this chapter).

PALEOMAGNETISM

Archive-half sections of cores from Hole 1065A were measured using the cryogenic magnetometer at 5-cm intervals as described in the “Paleomagnetism” section, “Explanatory Notes” chapter (this volume). As time permitted, most sections were progressively demagnetized at 5-cm intervals using peak alternating fields (AF) of 10, 15, 20, 25, 30, 35, 45, 55, and 65 mT. Twenty-eight discrete samples were progressively AF and thermally demagnetized to determine directional stability and to verify magnetostratigraphic results from the cryogenic magnetometer. The volume magnetic susceptibility was measured at 5-cm intervals on most of the cores from Hole 1065A.

Demagnetization Behavior

Whole-Core Pass-Through Measurement

As found in previous legs, we observed evidence for remagnetization imparted by coring. In Figure 11, we show the natural remanent magnetization (NRM) in Core 173-1065A-27R before and after 25-mT AF demagnetization. The NRM inclinations are often biased toward high positive inclinations (>65°), suggesting drilling-induced magnetization. Fortunately, AF demagnetization to 25 mT generally removed the drilling-induced component, as indicated by a change in inclination to a mean value of 47° (Fig. 11).

AF and Thermal Demagnetization of Discrete Samples

Oriented samples (6-cm^3 plastic cubes or 10-cm^3 minicores) were collected to verify the magnetostratigraphic results from the cryogenic magnetometer and to understand the magnetic property of the rocks during stepwise demagnetization. Sixteen of these samples were AF demagnetized and 12 minicores from representative lithified cores from Hole 1065A were thermally demagnetized. We found that both demagnetization techniques effectively removed secondary magnetizations and isolated the characteristic remanent magnetization (Fig. 12). Several minicores from lithostratigraphic Unit V displayed signs of mineralogical alteration after thermal demagnetization above 300°C. The shipboard thermal demagnetization results are not straightforward to interpret and need to be improved postcruise by analyzing additional discrete samples.

Magnetostratigraphy

Shipboard magnetostratigraphy within the lower Miocene interval is not well defined, although there are distinct polarity changes in portions of the cores. Cryogenic magnetometer measurements suggest that several polarity reversals were recorded in Core 173-1065A-1R (between 251 and 254 mbsf; Fig. 13). The polarity sequence determined from measurements in the cryogenic magnetometer was confirmed by progressive AF and thermal demagnetization of corresponding discrete samples. Biostratigraphic Zones NN4 and M4a (16.7–18.3 Ma) are also placed in this depth interval (see “Biostratigraphy” section, this chapter). Thus, the first shift in polarity at 251.3 mbsf (Fig. 13) may correspond to the end of the C5Cr chron (16.726–17.277 Ma), assuming the biostratigraphic age markers are correct. More exact polarity assignments and construction of a magnetostratigraphy for the deeper intervals, however, are impossible because of the absence of adequate age control, poor core recovery, and disturbance by slumps in the cored sediments.

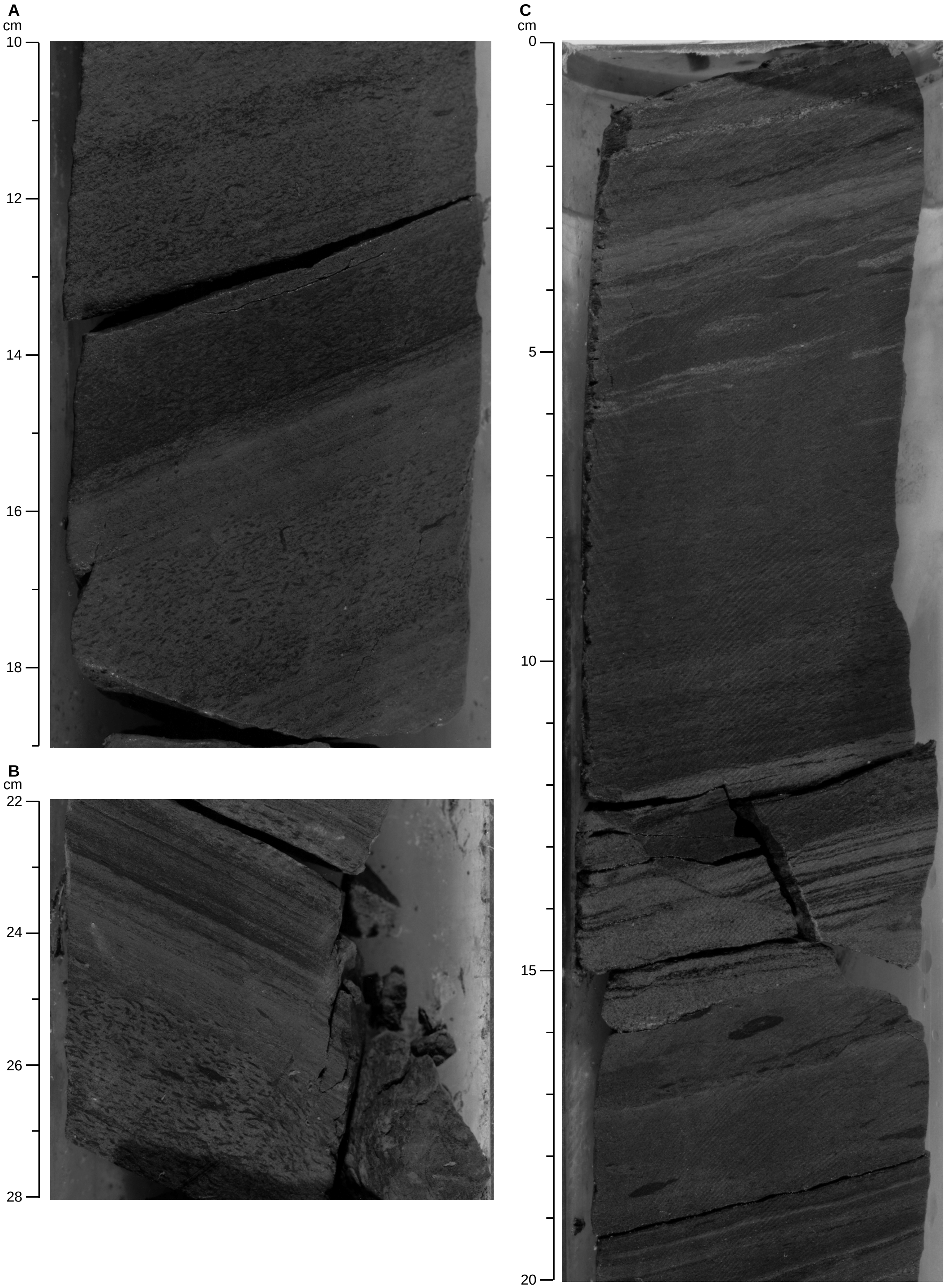
A
cm
10
12
14
16
18
B
cm
22
24
26
28
C
cm
0
5
10
15
20

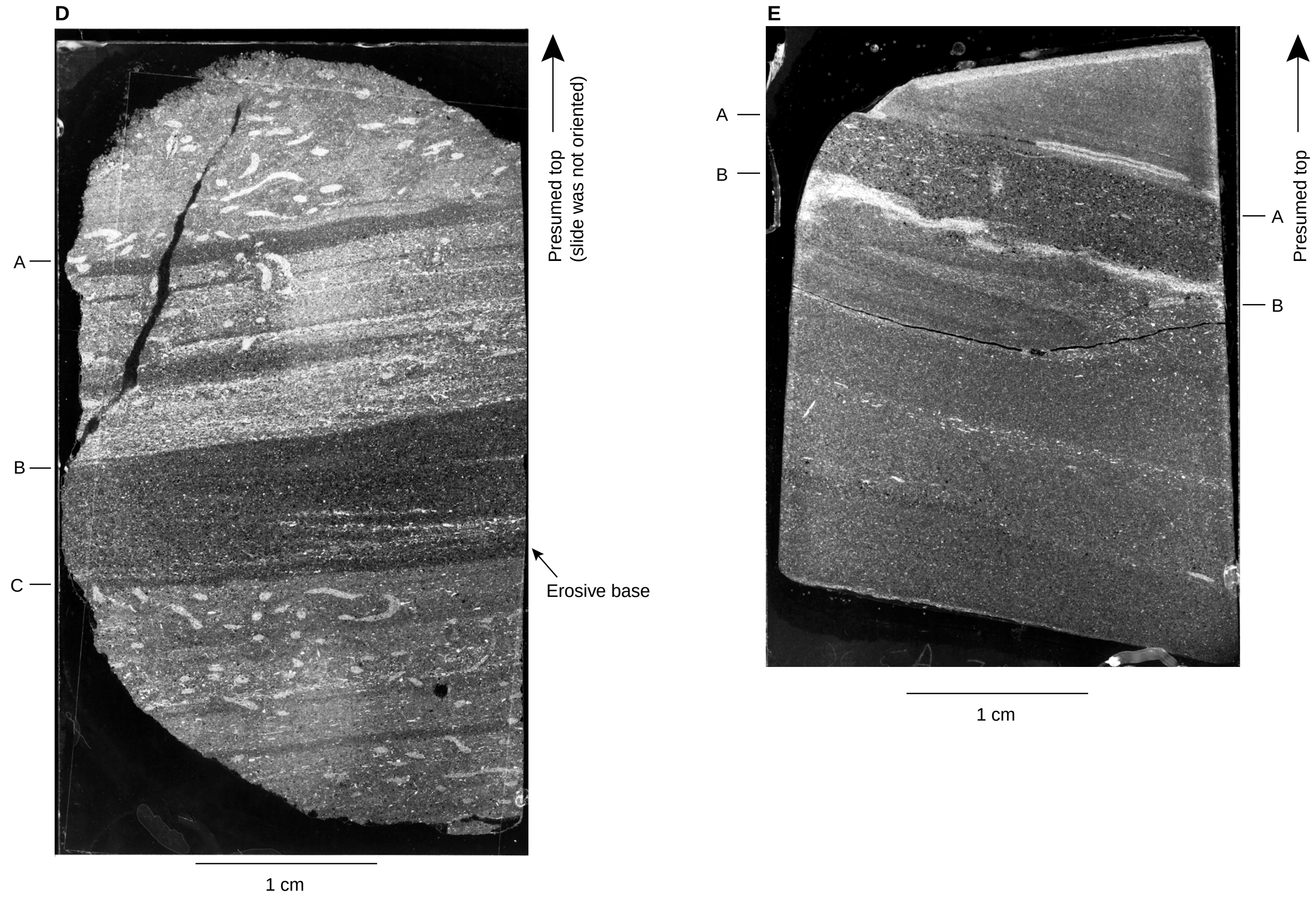

Figure 10. Characteristic features of Subunit VB in Hole 1065A. **A–C.** Core photographs. Note that all depths and intervals given in the descriptive text in the captions refer to the left side of the cores. (A) Interval 173-1065A-30R-1, 10–19 cm. Claystones dominated by *Chondrites.* Note that the bases of the *Chondrites* burrowed intervals have sharp bases (at 18.5 cm at core fracture surface, 15.9 and 15.6 cm). At the top of one of these intervals (at 17.0 cm) larger burrows penetrate 2–3 mm downward so that the contact between the *Chondrites* interval and the overlying more massive lithology is irregular. (B) Interval 1065A-29R-1, 22–28 cm. The top of a *Chondrites* interval at 24.8 cm shows a burrowed contact with the overlying lithology. The base of a sharp-based silty layer occurs at 23.6 cm, above which there is a laminated interval, overlain by a *Chondrites* interval, the base of which intersects the top of the photograph. (C) Interval 1065A-33R-1, 0–20 cm. Between 12.5 and 16 cm, two laminated fine sandstone intervals are cut by a fault. The darker laminae contain abundant fragments of plant material. The base of the sandstone to the left of the fault is erosive, truncating a *Teichichnus* burrow. Above this basal contact cross laminae occur. Between 4 and 6 cm, lenticular and wavy laminae of siltstone occur. The lighter interval between 2.0 and 2.3 cm has a slightly undulating base, with thin silty sediment occurring only in the depressions along this surface. **D, E.** Negative photographs of thin sections. Note that darker areas contain greater proportions of silt-sized quartz clasts (individual clasts show as tiny gray subangular spots) and fine-grained dolomite, and lighter areas contain more clay, very fine-grained plant debris, and pyrite. Elongate white flecks are composed of carbonized plant debris. (D) Sample 1065A-24R-1, 72–75 cm. Sharp contact at “A” is between upper *Chondrites* burrowed bed above, and darker lamina below. Some *Chondrites* penetrate through the latter into the underlying lighter interval. “B” shows the sharp contact between dolomite-rich (below) and plant-rich (above) intervals. “B–C” marks a dolomite-rich bed showing cross laminae picked out by plant debris. “C” is a sharp contact between cross laminated bed and underlying burrowed bed that is slightly undulatory, and may be erosional, as the two burrows to the far left are truncated by it, and to the right its base becomes progressively close to a faint lamina ~1 mm below. (**E**) Sample 1065A-31R-CC, 15–20 cm. A dolomitic siltstone between “A” and “B” has a sharp base and top. The base is undulatory and is underlain by a deformed plant-rich lamina. The contact may be the result of erosion before the deposition of the silt and subsequent load casting.

Paleomagnetic Observations from Lithostratigraphic Unit V

The Middle–Upper Jurassic cores all have normal polarity except for two short reversed intervals in Core 173-1065A-29R between 568.8 and 570.1 mbsf (Fig. 14). Note that the upper reversal indicated by the change in polarity of inclination is accompanied by a nearly 180° change in declination, adding confidence to the polarity determination (Fig. 14). However, there is a huge intensity spike at 569.8 mbsf associated with the second reversal (Fig. 14). An examination of the corresponding core photograph reveals an interval of dark gray laminated silty claystone and conglomerate. AF demagnetization at 25 mT greatly reduced this susceptibility peak (Fig. 14), casting doubts on the validity of this reversal interval. Therefore, this second short reversal will have to await shore-based work for confirmation. The Jurassic rocks were generally recovered in relatively long, coherent sections of core. An example of the magnetic results of these cores is shown in Figure 11 (for Core 173-1065A-27R). Downhole inclinations and declinations after AF demagnetization (Fig. 11) are similar and consistent, suggesting the magnetization recorded in this core is homogeneous and was not produced during drilling. Based on the assumption that this magnetization represents the actual geomagnetic field during the Middle–Late Jurassic and because the hole was essentially vertical (maximum deviation of 2° estimated from FMS data, see “Downhole Measurements” section, this chapter), we estimated the attitude of bedding planes by using the Late Jurassic pale-

Table 4. Stratigraphic distribution of planktonic foraminifer taxa from Hole 1065A.

Age	Zonal range	Hole, core, section, interval (cm)	Depth (mbsf)	Abundance	Preservation	*Globigerinoides trilobus*	*Globoquadrina dehiscens*	*Globoquadrina venezuelana*	*Globorotalia peripheroronda*	*Catapsydrax stainforthi*	*Globigerinoides altiapertura*	*Globorotalia kugleri*	*Catapsydrax dissimilis*	*Catapsydrax unicavus*	*Globigerinoides* spp.	*Globorotalia mayeri*	*Globigerina praebulloides*	*Globigerinoides immaturus*	*Globigerinoides primordius*	Indeterminate spp.
early Miocene	M4a	1065A-1R-1, 81-85	253.31	A	G	A	A	A	F	R	R		F		F			F		R
early Miocene	M1-M3	1065A-1R-CC	257.1	A	G		F	F		R		R	F		F	F	F	F		
early Miocene	M1-M3	1065A-2R-CC	263.27	B																
early Miocene	M1-M3	1065A-3R-CC	273.23	A	G		F	F		R			F	R		R				
early Miocene	M1-M3	1065A-4R-CC	286.7	A	G	F	F	F									F			
early Miocene	M1-M3	1065A-5R-CC	291.33	A	G			F				R	F						R	R
Tithonian		1065A-6R-CC	302.63	B																
Tithonian		1065A-7R-CC	308.86	B																

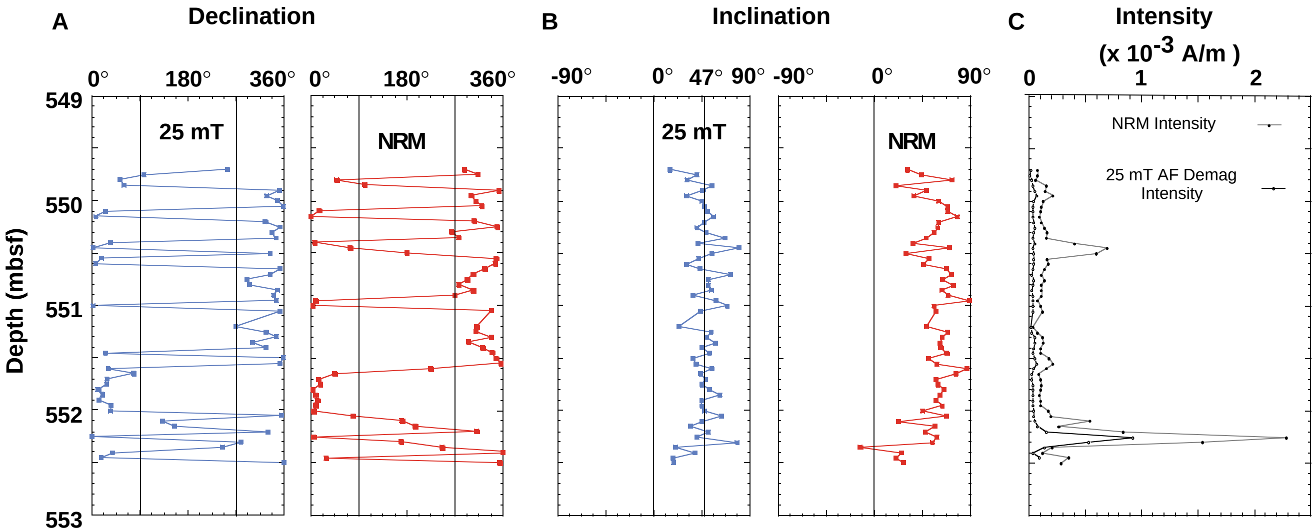

Figure 11. Remanent magnetization before (NRM) and after (25-mT) AF demagnetization to 25 mT as a function of sub-bottom depth. Declination (**A**), inclination (**B**), and intensity (**C**) of the archive half of Core 173-1065A-27R are shown. NRM inclinations are biased toward high positive inclinations, suggesting that drilling-induced magnetization is present. AF demagnetization to 25 mT generally can remove this drilling-induced magnetization, as indicated by changes in inclination and intensity.

omagnetic reference pole for the Iberia plate (Van der Voo, 1969; Schott et al, 1981; Galdeano et al., 1989). If the observed mean paleomagnetic vector is rotated to match the Late Jurassic paleovector, then the result indicates that the azimuth of dip of the bedding planes for Core 173-1065A-27R is northeast (N35°E) and the amount of dip is 25.4°. These computed values are in excellent agreement with those obtained by FMS logging (see "Downhole Measurements" section, this chapter). A preliminary calculation of paleolatitude from these inclination data suggests that the drill site was located at about 23°N during the Middle–Late Jurassic and indicates about 17° northward displacement of the region since the Late Jurassic.

Magnetic Susceptibility

Figure 15 shows the downhole profiles of magnetic susceptibility and the variation of NRM intensity for Hole 1065A. In general, the whole-core magnetic susceptibility measurements vary in similar fashion to the NRM intensity signals. In Hole 1065A, poor core recovery, drilling disturbance, and the fact that lithostratigraphic Unit II contained slumped sediments resulted in an incomplete record of magnetic susceptibility that is difficult to interpret.

The greatest susceptibility occurs at about 270 mbsf. An examination of the corresponding core photograph reveals an interval of dark terrigenous sand at the base of Section 173-1065A-2R-2. This characteristic susceptibility response might be useful for identifying turbidites using a magnetic susceptibility logging tool.

STRUCTURAL GEOLOGY

Structural Observations in Lithostratigraphic Unit II

The cores of lithostratigraphic Unit II exhibit pervasive soft-sediment deformation. A variety of deformation structures was observed, including slump folds (Fig. 16), microfaults (Figs. 17, 18), and zones of sheared clay. The sedimentary bedding is predominantly subhorizontal to gently dipping, but because of slumping, steeply inclined and subvertical bedding occurs as well (Fig. 19; Table 5).

Slump folds were observed in all six cores from Unit II. The folds are marked by alternating dark- and light-colored siltstone layers (Fig. 16). The layering does not appear to have had a mechanical influence on the folding process but only to have acted as a passive marker during flow of poorly lithified material. Fold shapes range

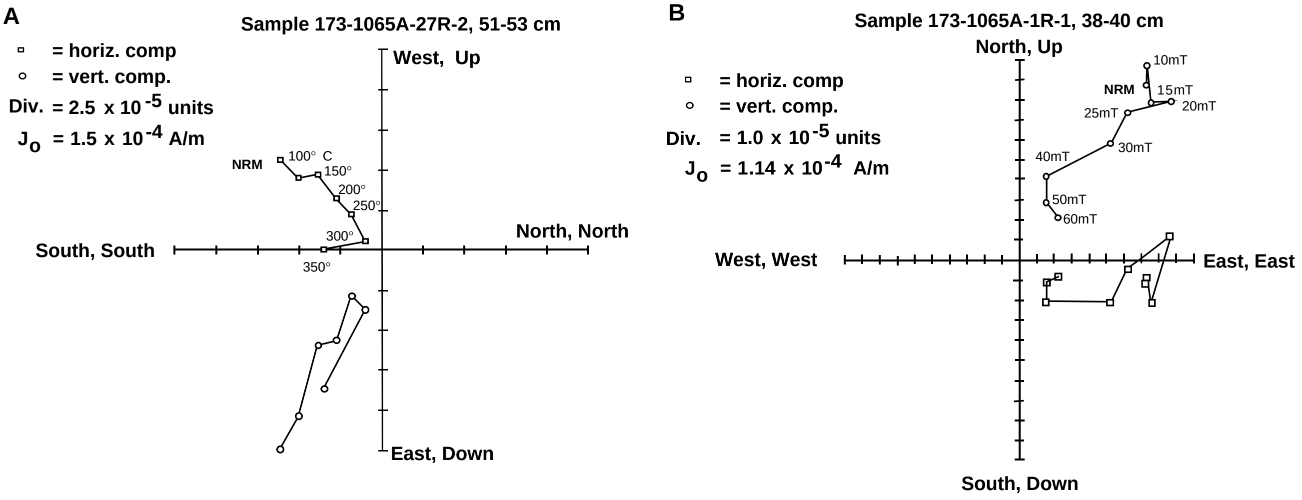

Figure 12. Representative vector end-point diagrams showing the results of (**A**) thermal demagnetization of discrete Sample 173-1065A-27R-2, 51–53 cm, and (**B**) AF demagnetization of Sample 173-1065A-1R-1, 38–40 cm. Open squares and circles represent the projection of the magnetization vector end points on the horizontal and vertical planes, respectively. (Note: the declination values in this figure have not been corrected; see "Paleomagnetism" section, "Explanatory Notes" chapter, this volume).

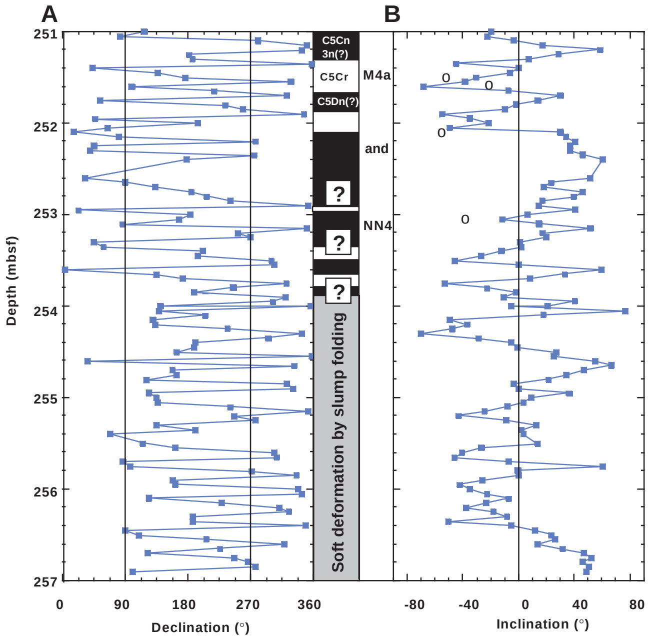

Figure 13. Downhole variation of stable magnetic (**A**) declination and (**B**) inclination, with inferred polarity and biostratigraphic zones for Core 173-1065A-1R. Normal polarity is indicated by black areas; reversed polarity is indicated by white areas. Discrete samples are shown by circles.

from isoclinal (e.g., interval 173-1065A-1R-3, 60–75 cm) to open. Slump folds occur on all scales visible in the cores. The orientation of axial surfaces and fold axes is highly variable, although shallowly inclined axial surfaces appear to be slightly more common than steep ones. Folds are strongly noncylindrical (e.g., sheath fold in interval 173-1065A-1R-3, 100 cm). Refolded folds also occur. The irregular shapes of these indicate that they were not formed during successive deformation events but during progressive, inhomogeneous flow deformation in a single event.

Microfaults are also ubiquitous in lithostratigraphic Unit II. They occur in closely (about 1 cm to 2 mm) and regularly spaced arrays, which resemble a cleavage in some intervals. In such arrays all microfaults exhibit the same orientation and sense of slip (Fig. 17). On close inspection with a hand lens, many of the microfaults turn out to be brittle, less than 1-mm-wide shear zones. Slip along the microfaults is accompanied by antithetic rotation of the material between the microfaults (domino mechanism; Fig. 17). Microfaults include normal faults (Fig. 17), reverse faults (Fig. 18), subvertical, and subhorizontal faults (with respect to the core reference frame). Conjugate microfaults were observed in some intervals (e.g., interval 173-1065A-4R-1, 120–125 cm; see also Fig. 18). The orientations of σ_1 obtained from these vary between subhorizontal and subvertical with respect to the core reference frame.

The microfault arrays mostly cut across earlier formed isoclinal folds (Figs. 18, 20; e.g., interval 173-1065A-6R-1, 25–40 cm). In two cases (173-1065A-2R-1, 20–30 cm; 173-1065A-6R-1, 1–15 cm), however, the orientation of the microfault arrays changes across the axial plane of a slump fold (Fig. 20B).

Several millimeter- to centimeter-wide shear zones with relatively darker, clay-rich material were observed in the cores from Unit II. These are moderately inclined (e.g., working orientation 090°/25° in Section 173-1065A-2R-1, at 50 cm) and truncate the bedding in the adjacent rock at low angles.

Interpretation

The occurrence of arrays of normal, reverse, subvertical, and subhorizontal microfaults indicates that these structures did not form in a homogeneous stress field. They formed in response to either local stresses, both compressional and extensional, or to a rotational deformation regime. Both situations can arise during the slumping process. The fact that the orientations of σ_1 obtained from conjugate microfaults vary between subhorizontal and subvertical may be explained in the same way. Although the microfaults often overprint the slump folds and might therefore be interpreted as younger structures, the change in orientation of the microfaults across the axial planes of some slump faults indicates that folds and microfaults formed contemporaneously in these cases. The microfaults correspond to the "closely spaced antithetic shear surfaces" described by Dennis (1982). Such structures are only formed during soft-sediment deformation. The clay shear zones may represent the decoupling horizons along which individual packages of sediment moved.

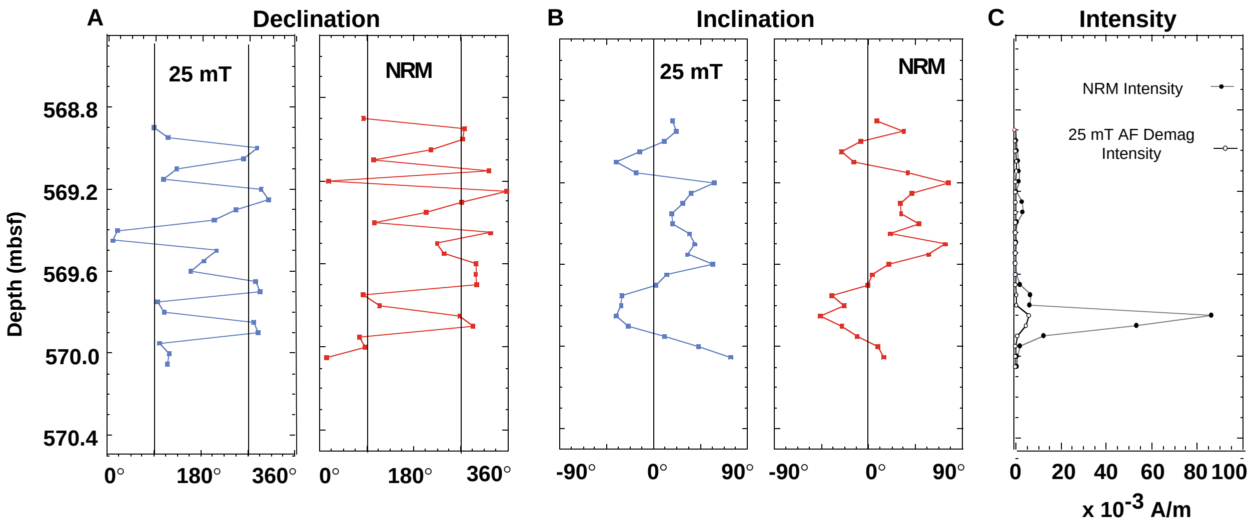

Figure 14. Downhole variation of (**A**) declination, (**B**) inclination, and (**C**) intensity of NRM and stable magnetization after AF demagnetization to 25 mT for Core 173-1065A-29R.

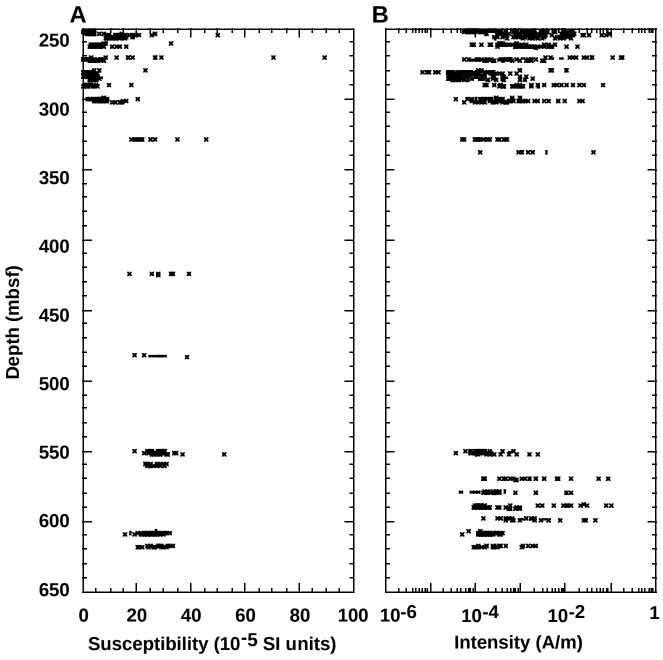

Figure 15. Plots of (**A**) magnetic susceptibility and (**B**) intensity as a function of sub-bottom depth in Hole 1065A.

Structural Observations in Lithostratigraphic Unit V

The dip of the bedding (relative to the core's vertical axis) in Unit V is between 0° and 65° (Fig.19; Table 5). The mean dip is 18° with a standard deviation of 10°. Deformation structures were observed only in 6 out of 29 cores (Cores 173-1065A-13R, 22R, 24R, 26R, 30R, and 32R). Altogether, Unit V appears rather undeformed, although the cores may not be fully representative because of the poor recovery (12.4%). Deformation structures include folds (Fig. 21), faults (Fig. 22), veins, and brecciation.

Small folds with amplitudes of a few millimeters occur in intervals 173-1065A-32R-CC and 173-1065A-33R-1, 70–78 cm (Fig. 21). In both cases, they appear to represent soft-sediment deformation because they are not regularly oriented and affect only single layers.

Faults were observed in Cores 173-1065A-13R, 22R, 32R, and 33R. These have offsets of a few millimeters, except the fault in interval 173-1065A-33R-1, 10–16 cm (Fig. 22), which has an offset of about 2 cm. This fault has a listric shape and is sealed by the overlying sediment, indicating synsedimentary faulting. Two moderately dipping faults in Section 173-1065A-33R-1 may have larger offsets, but neither the offset nor the slip sense could be determined because of the lack of markers. The other faults in Section 173-1065A-33R-1 include both reverse and normal faults and are associated with small folds (Fig. 21). The faults as well as the folds are interpreted to be related to soft-sediment deformation. Other microfaults, found in interval 173-1065A-32R-1, 10–40 cm, are connected with irregularly shaped, calcite-filled small veins and have slickensided surfaces. They represent conjugate normal faults. One of them dips east in the core reference frame (090°/62°) and the slip direction is 142°/49°, the conjugate one dips west (270°/67°). The acute angle between the faults is 51° and the orientation of σ_1 was almost vertical (090°/87°); that is, the conjugate faults indicate extensional stress.

Small veins about 1 mm thick, of irregular shape, occur in Sections 173-1065A-24R-1, 26R-1, 30R-1, 32R-1, and 32R-CC. Some are filled with calcite, some with dolomite.

Interpretation

Lithostratigraphic Unit V has been only weakly deformed. Most of the structures can be attributed to soft-sediment deformation, except possibly several small normal faults that are associated with carbonate veins.

Core Imaging

All recovered material from Site 1065 was imaged using the DMT Color CoreScan system in the slabbed mode. Images were made of the split archive half and recorded as bitmap images (Table 6, on CD-ROM, back-pocket, this volume). Variations in image size and camera aperture are also recorded in Table 6. Images were initially used to quantify structural features such as microfaults and slumping (see above). Postcruise processing will include assembly of an image for each core section.

Selected whole pieces of the Subunit VB bedded claystones were imaged in the unrolled mode to identify the dip of bedding planes

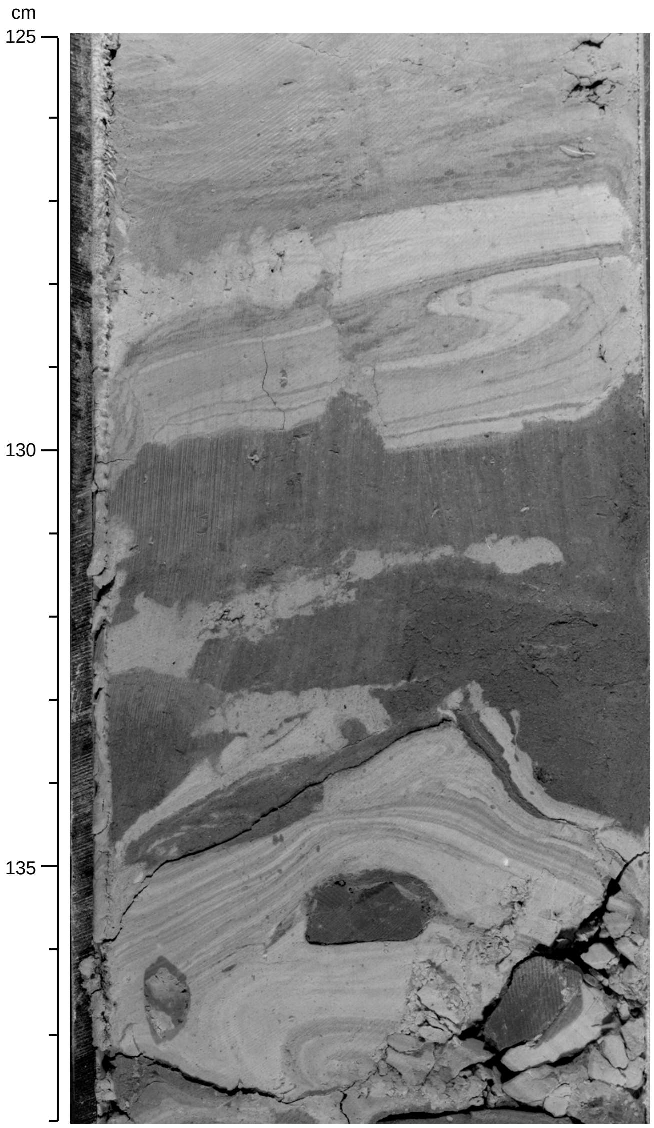

Figure 16. Soft-sediment fold structures from lithostratigraphic Unit II, Sample 173-1065A-1R-4, 125–138 cm.

with respect to the core axis. Initial quantitative studies identified beds with maximum dips ranging from 10° to 30°, which is consistent with on-core measured dips in Subunit VB (see Table 5). Core imaging of interval 173-1065A-32R-1, 92–113 cm, allowed the measurement of increasing dips downhole and correlative changes of azimuth in successive bedding planes (Fig. 23). This change is related to a subhorizontal rotation axis striking south-southeast (once the average dip is re-oriented toward east in the core reference frame). Unfortunately, the poor recovery at Hole 1065A limits the potential for further quantification of planar features and core-log integration.

ORGANIC AND INORGANIC GEOCHEMISTRY

Concentrations of carbonate, organic carbon, and total nitrogen in sediments from Hole 1065A were measured for one to five samples per core, depending on recovery. Routine measurements were also made of headspace gas compositions as part of the drilling safety program.

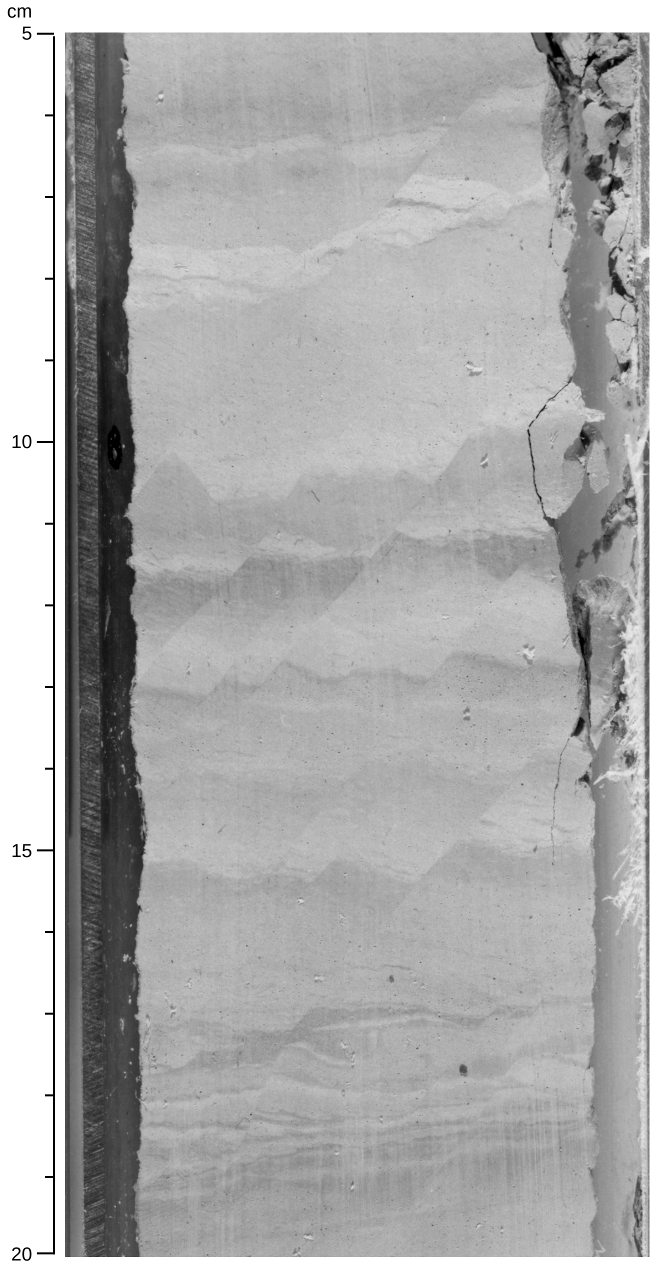

Figure 17. Micro-normal faults in sediments of lithostratigraphic Unit II showing uniform orientation and sense of slip and accompanied by antithetic rotation of bedding (domino mechanism). Sample 173-1065A-1R-1, 5–20

Inorganic and Organic Carbon

Concentrations of inorganic (carbonate) carbon in sediments at Site 1065 vary from near 0% to almost 11% (Table 7). These amounts are equivalent to $CaCO_3$ concentrations (assuming that all the carbonate is present as pure calcite) of ~1% to 90%. Concentrations of $CaCO_3$ are generally high for sediments from Unit II (lower Miocene), which are dominantly nannofossil chalk (Fig. 24). In contrast, most of the Upper Jurassic sediments in Unit V have very low $CaCO_3$, with the exception of chalk at ~328 mbsf, near the top of Subunit VA, and a carbonate-rich horizon at 501.6 mbsf, right at the boundary between Subunits VA and VB (Fig. 24). Although Subunit

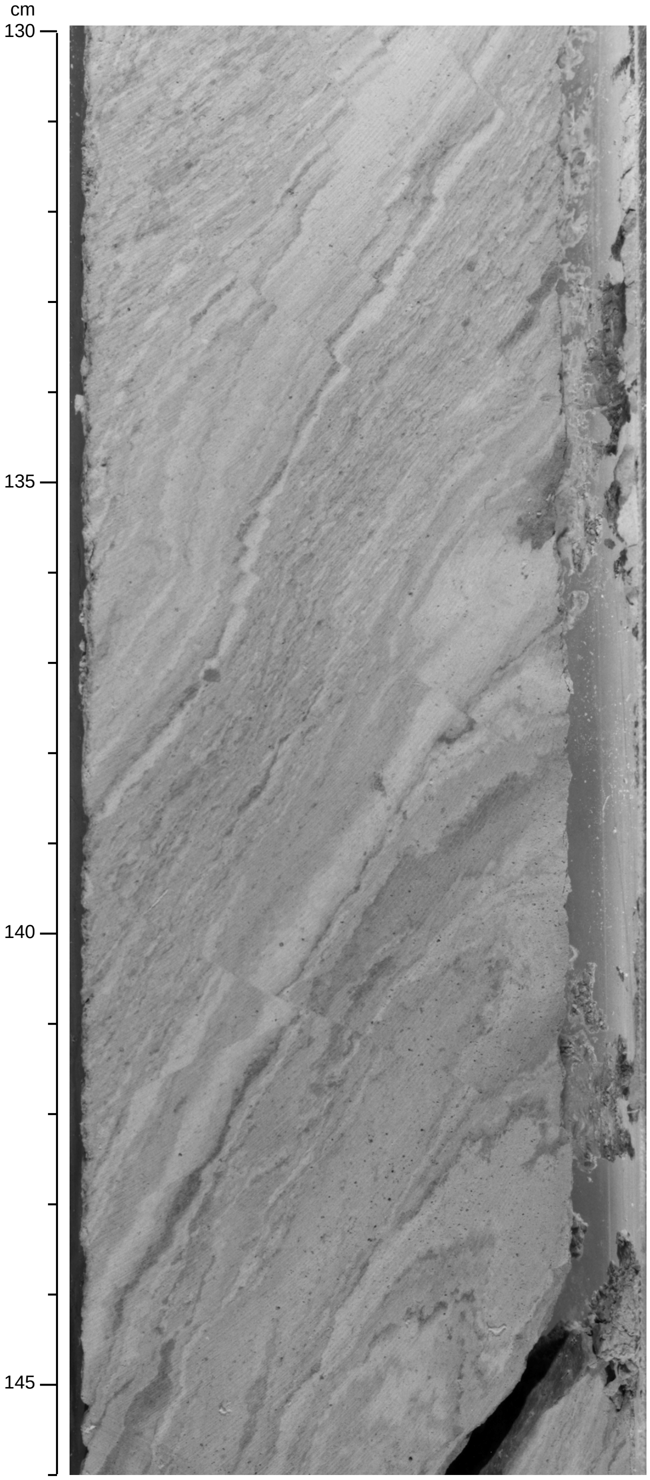

Figure 18. Micro-reverse faults overprinting slump folds in sediments of lithostratigraphic Unit II. At 141 cm, a set of conjugate microfaults can be observed. Sample 173-1065A-4R-4, 130–146 cm.

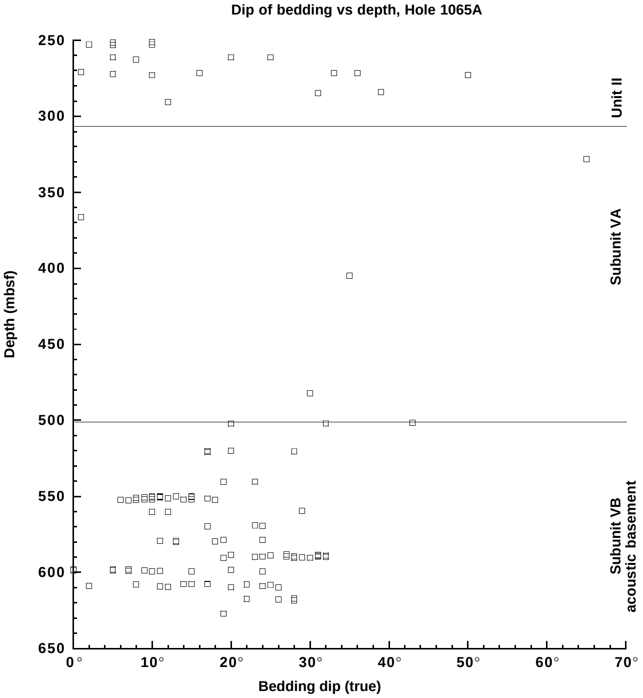

Figure 19. Dip of bedding vs. depth for lithostratigraphic Unit II and Unit V.

VA is dominantly composed of claystone, some samples show petrographic evidence of dolomitization, which is manifested in slightly elevated carbonate contents (≤20 wt% $CaCO_3$).

Concentrations of organic carbon are very low in Unit II (below detection in most samples), and quite variable in Unit V, ranging from 0.1% to 0.85% (Table 7; Fig. 24). Sulfur contents of nearly all samples were below detection. Nitrogen contents were below detection in sediments from Unit II and mostly between 0.05% and 0.1% in Unit V. Most samples in Unit V have organic C/N values <10, which indicates that the organic matter is dominantly of marine origin (Fig. 24). However, organic C/N values as great as 20 in a sample from 501.6 mbsf indicate a component of terrestrial-derived material, consistent with the presence of microscopic plant fragments (charcoal) in some sediments. Because marine algal organic matter is normally oxidized and recycled during settling and deposition on the seafloor (e.g., Suess, 1980), the moderately high organic carbon contents in Unit V require special depositional conditions, such as downslope transport and rapid burial. Based on sedimentary structures, much of the sediment in Unit V has been interpreted as having been emplaced by turbidites (see “Lithostratigraphy” section, this chapter), which could provide an explanation for the observed organic carbon contents.

Headspace Gas Measurements

Methane concentrations in headspace gases were very low at Site 1065, varying from 2 to 6 ppm (Table 8), and concentrations of heavier hydrocarbons, CO, CO_2, and H_2S were generally below detection. Such low methane concentrations for sediments in Unit V are surprising given their moderately high organic carbon contents. At Site 897, located ~100 km west of Site 1065, low methane in sediments with organic carbon contents similar to those at Site 1065 were correlated with anomalously high interstitial water sulfate contents (Shipboard Scientific Party, 1994a). Because the presence of interstitial water sulfate inhibits methanogenesis (Claypool and Kvenvolden, 1983) the lack of methane in Unit V at Site 1065 may also be a result of anomalous interstitial water sulfate values. Unfortunately, as described below, we were unable to collect interstitial water samples from Unit V, and thus the cause of the low methane contents remains uncertain.

Interstitial Water

Because of very low core recovery at Site 1065, as well as the low interstitial water content of sediments below ~500 mbsf, only two in-

Table 5. Measured structural data in Hole 1065A.

Core, section	Depth in core (cm)	Depth (mbsf)	Bedding azimuth (working; °)	Bedding dip (true; °)	Fault azimuth (working; °)	Fault dip (true; °)	Fault dip (apparent; °)	Lineation azimuth (working; °)	Lineation dip (true; °)
173-1065A-									
1R-1	10	251.1			72	45			
1R-1	20	251.2	325	10					
1R-1	48	251.5	45	5					
1R-1	70	251.7					57 to east		
1R-2	5	252.5					25 to west		
1R-2	13	252.6			76	63			
1R-2	18	252.7	90	2					
1R-2	35	252.8	19	10					
1R-2	40	252.9					10 to west		
1R-2	75	253.3	42	5					
1R-4	130	256.8					75 to west		
2R-1	20	260.9					50 to west	90	45
2R-1	30	261					30 to west		
2R-1	36	261.1					12 to west		
2R-1	50	261.2			90	25		90	25
2R-1	52	261.3	47	20					
2R-1	85	261.3	45	5					
2R-1	132	262					9 to west		
2R-1	145	262.2					55 to west		
2R-2	57	262.9	90	8					
3R-1	61	270.9	0	1					
3R-1	135	271.6	64	16					
3R-1	137	271.7	20	36					
3R-1	148	271.8	67	33					
3R-2	50	272.3	270	5				0	30
3R-2	93	272.7	330	50					
3R-2	110	272.9			348	42		330	40
3R-CC	11	273.1	90	10					
4R-1	120	281.2					3 to west		
4R-1	121	281.3					37 to east		
4R-2	115	282.7					81 to west		
4R-3	126	284.3	284	39					
4R-4	28	284.8	270	31					
5R-2	3	290.8	270	12					
5R-2	8	290.9					60 to east		
6R-1	28	299.5			130	37			
9R-1	20	328.3	180	65					
13R-1	5	366.4	0	1					
17R-1	18	405.1	310	35					
22R-1	8	482.3	60	30					
23R-1	5	501.6	196	43					
23R-1	40	501.9	218	32					
23R-CC	5	502.2	62	20					
24R-1	15	520.9	113	17					
24R-1	35	520.1	58	20					
24R-1	42	520.2	60	17					
24R-1	58	520.4	191	28					
26R-1	25	540.3	329	23					
26R-1	52	540.5	90	19					
27R*-1	23	549.9	63	15					
27R-1	23	550	90	11					
27R-1	33	550.1	90	10					
27R-1	41	550.2	90	13					
27R*-1	55	550.3	62	15					
27R-1	61	550.4	90	11					
27R-1	81	550.5	90	9					
27R*-1	87	550.6	93	11					
27R-1	99	550.7	90	9					
27R*-1	105	550.8	66	10					
27R-1	127	551.1	90	8					
27R-2	6	551.3	90	12					
27R-2	30	551.5	90	17					
27R-2	64	551.8	90	10					
27R*-2	67	551.9	40	15					
27R-2	73	552	90	9					
27R-2	103	552.2	90	14					
27R*-2	105	552.3	69	18					
27R-2	115	552.4	90	8					
27R-2	128	552.5	90	6					
27R-CC	4	252.6	90	7					
28R-1	20	559.5	122	29					
28R-1	76	560.1	105	12					
28R-CC	3	560.2	90	10					
29R-1	25	569.1	246	23					
29R-1	40	569.3	246	24					
29R-1	85	569.7	214	17					
30R-1	10	578.6	90	19					
30R*-1	18	578.7	81	24					
30R-1	35	578.8	90	19					
30R-1	65	579.1	90	13					
30R-1	100	579.4	90	11					
30R*-1	104	579.5	126	18					
30R-1	130	579.8	90	13					
31R-1	20	588.3	90	27					
31R*-1	44	588.5	86	31					
31R-1	45	588.6	90	20					
31R-1	65	588.8	90	25					
31R*-1	86	589	99	32					

Table 5 (continued).

Core, section	Depth in core (cm)	Depth (mbsf)	Bedding azimuth (working; °)	Bedding dip (true; °)	Fault azimuth (working; °)	Fault dip (true; °)	Fault dip (apparent; °)	Lineation azimuth (working; °)	Lineation dip (true; °)
31R-1	90	589.1	90	31					
31R-1	120	589.4	90	27					
31R*-1	134	589.5	91	28					
31R-1	140	589.6	90	31					
31R-2	15	589.7	90	24					
31R*-2	17	589.8	86	23					
31R*-2	28	589.9	92	32					
31R-2	34	590	90	29					
31R-2	65	590.3	90	30					
31R-2	84	590.5	90	28					
31R-2	100	590.6	90	19					
32R-1	20	597.9	90	7	90	62		142	49
32R-1	22	598			270	67			
32R*-1	26	598.1	107	5					
32R-1	30	598.2	90	0					
32R-1	31	598.3	90	20	234	62			
32R-1	55	598.5	90	0					
32R-1	70	598.7	90	5					
32R*-1	99	598.9	95	9					
32R-1	100	599	90	7					
32R*-1	105	599.1	88	11					
32R*-1	107	599.2	80	15					
32R-1	130	599.4	90	10					
32R-CC	5	599.5	289	24					
33R-1	5	607.5	90	17					
33R*-1	13	607.6	114	14					
33R-1	20	607.7	90	15					
33R*-1	21	607.8	63	17					
33R*-1	30	607.9	59	22					
33R-1	45	608	90	8					
33R*-1	50	608.1	71	25					
33R-1	113	608.8	90	2					
33R-1	134	609	118	24					
33R-2	29	609.3	135	11					
33R-2	53	609.5	325	12					
33R-2	82	609.8	340	20					
33R-CC	5	609.9	10	26					
34R-1	10	617.2	90	28					
34R-1	48	617.6	90	22					
34R-1	80	617.9	90	26					
34R-CC	10	618.4	90	28					
35R-CC	5	627.1	270	19					

Note: * = measurements were obtained by using the Digital Color CoreScan system (DMT).

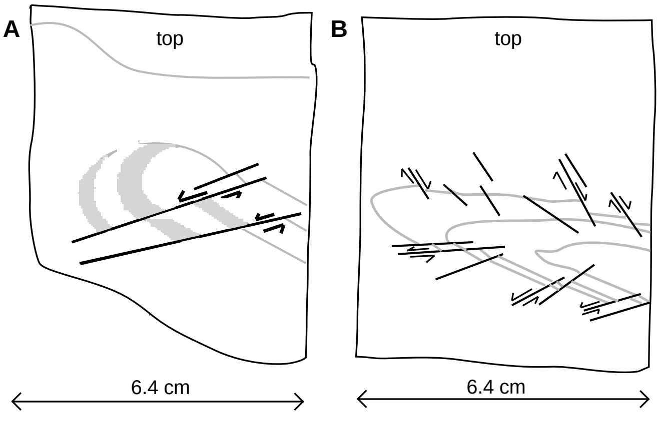

Figure 20. Relationships between microfaulting and folding in soft sediments. **A.** Fold in soft sediments cut by later microfaults (Sample 173-1065A-6R-1, 25−40 cm). **B.** Orientation of microfaults changes across the axial plane of a slump fold (Sample 173-1065A-6R-1, 1−15 cm).

terstitial water samples were collected and analyzed (Table 9). Both samples were from nannofossil chalk in Unit II (251−301 mbsf; early Miocene in age). For these samples, sulfate concentrations are low (6−7 mM), and chloride values (~550 mM) are close to that of seawater. Cation concentrations are ~6 mM for potassium, 25 mM for both calcium and magnesium, and ~450 mM for sodium. The cation concentrations are similar to those in interstitial waters from lower Miocene sediments at similar sub-bottom depths at Site 900, located 26 km west of Site 1065 (Shipboard Scientific Party, 1994c).

PHYSICAL PROPERTIES

Introduction

Physical property measurements were made on whole cores, split cores, and discrete samples. Multisensor track (MST) measurements for whole cores included magnetic susceptibility, gamma-ray attenuation (GRAPE bulk density), acoustic compressional-wave velocity, and natural gamma radiation. Index properties measured on discrete samples included wet and dry masses and dry volume. These measurements were used to calculate porosity, bulk and grain density, void ratio, and water content. Acoustic compressional-wave velocity and thermal conductivity were measured on split cores using the Hamilton Frame Velocimeter and TK04 Thermal Conductivity Meter, respectively.

Index Properties

Bulk densities, grain densities, and porosities were calculated for discrete samples recovered from Hole 1065A using gravimetric methods (Table 10). Uncertainties in calculating these properties can be ascertained using the precision of the mass and volume measurements that were directly determined (see “Physical Properties” section, “Explanatory Notes” chapter, this volume). The uncertainties are approximately 2% of the measurement for each property. Plots of bulk density and porosity vs. depth for this site (Fig. 25) indicate a systematic decrease in water content and porosity with depth. The bulk density vs. depth plot also shows a step increase in density at 501 mbsf, which is coincident with the lithostratigraphic Subunit VA/ Subunit VB boundary.

Bulk density ranges from 1.71 to 2.21 g/cm^3 in Unit II (nannofossil chalk and claystone), 2.00 to 2.80 g/cm^3 in Subunit VA (claystone and calcareous claystone), and 2.22 to 2.80 g/cm^3 in Subunit VB (claystone and dolomitic claystone). Porosity decreases from Unit II to Subunit VB, ranging from 30% to 56% in Unit II and 3% to 31% in Subunit VB. Grain densities are uniform over the entire depth of Hole 1065A, ranging from 2.58 to 3.20 g/cm^3 with all but two measurements lying between 2.69 and 2.84 g/cm^3. No crystalline basement rock was cored at Site 1065. The bulk densities and porosities associated with the claystones in Subunit VB suggest that the top of this subunit represents acoustic basement.

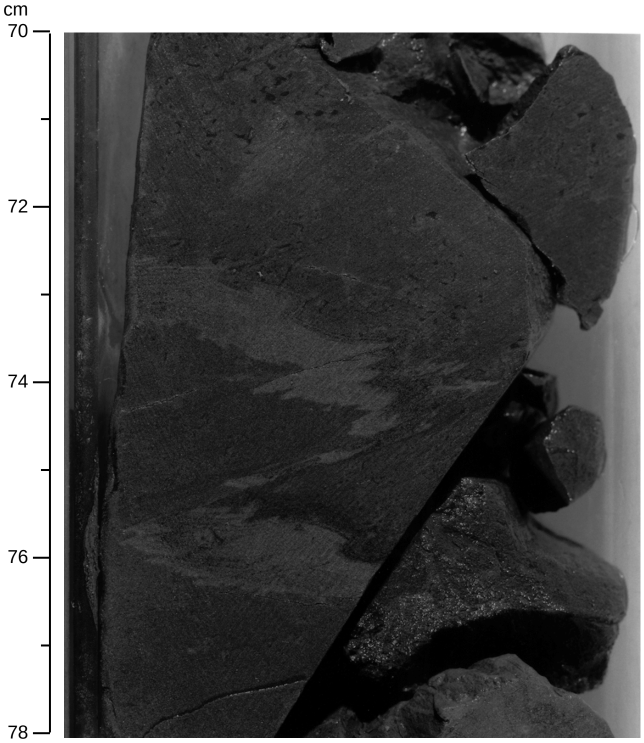

Figure 21. Folds and micro-reverse faults in lithostratigraphic Unit V. Sample 173-1065A-33R-1, 70–78 cm.

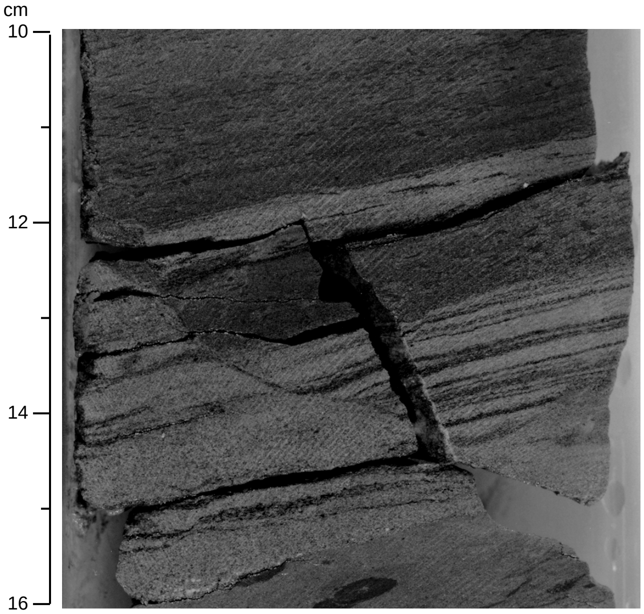

Figure 22. Synsedimentary micro-normal fault in lithostratigraphic Unit V. Sample 173-1065A-33R-1, 10–16 cm.

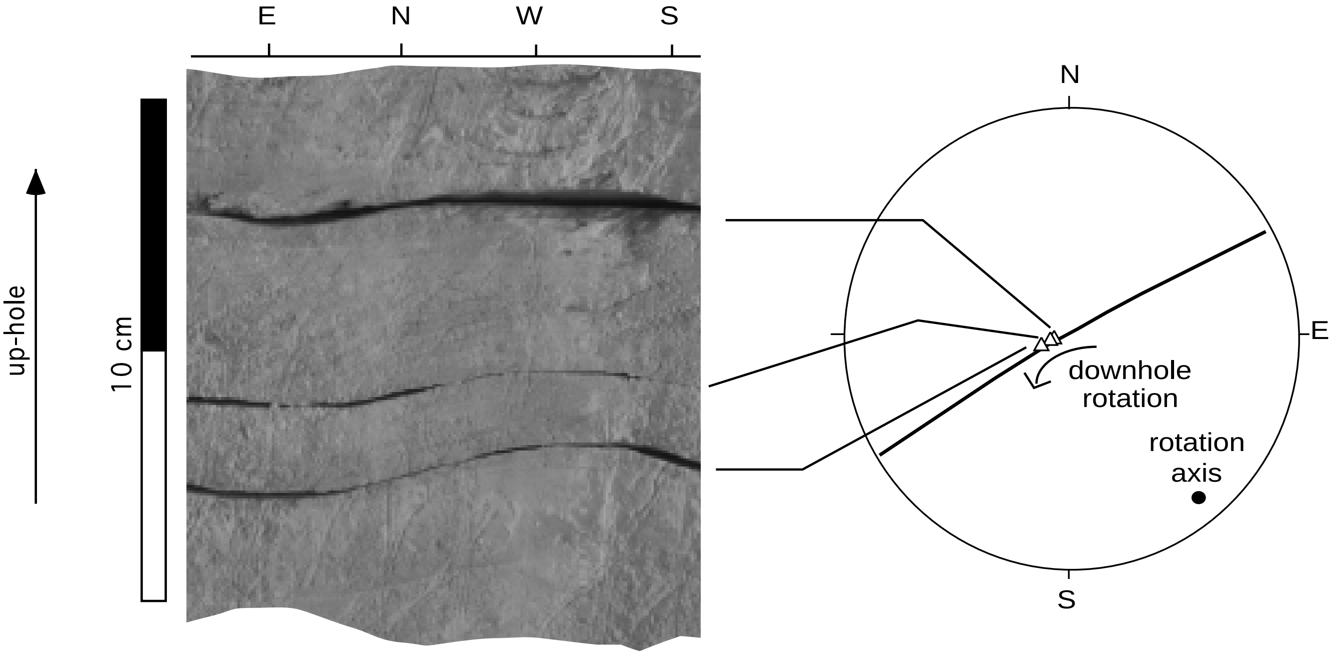

Figure 23. Unrolled image of interval 173-1065A-32R-1, 92–113 cm. The main dip of bedding is assumed to be toward the east in the core reference frame (see Fig. 8 in “Structural Geology” section, “Explanatory Notes” chapter, this volume). The core is broken along three bedding planes, which exhibit a downhole rotation around an almost horizontal axis plunging with a low angle toward the southeast (Wulff projection, lower hemisphere).

Thermal Conductivity

A half-space thermal conductivity probe was used exclusively to measure thermal conductivity in split core samples with a frequency of one sample per core (see “Physical Properties” section, “Explanatory Notes” chapter, this volume). Thermal conductivity vs. depth for Site 1065 is shown in Figure 26 and data are listed in Table 11 (on CD-ROM, back-pocket, this volume). Sparse data between Core 173-1065A-9R and Core 173-1065A-22R are a result of extremely low core recovery. Measurements suggest gradual increase in thermal conductivity with depth with a sharper increase around 520–550 mbsf. This boundary, which displays an increase of 0.50 W/(m·K), lies within acoustic basement. Over the entire depth range at Hole 1065A, thermal conductivity varies from 1.2 W/(m·K) in Subunit VA to 3.45 W/(m·K) in Subunit VB.

Table 7. Carbonate, carbon, and nitrogen in sediments from Site 1065.

Core, section, interval (cm)	Depth (mbsf)	Inorganic C (wt%)	$CaCO_3$ (wt%)	Organic C (wt%)	N (wt%)	Organic C/N
173-1065A-						
1R-1, 31-32	251.31	8.79	73.2	—	—	—
1R-1, 69.5-70.5	251.7	10.77	89.7	—	—	—
1R-1, 110-111	252.1	10.12	84.3	—	—	—
1R-2, 75-76	253.25	10.60	88.3	—	—	—
1R-4, 71-72	256.21	0.21	1.7	0.1	—	—
2R-1, 67-69	261.37	8.48	70.6	—	—	—
2R-2, 75-77	262.95	5.48	45.6	—	—	—
3R-2, 72-73	272.52	8.37	69.7	—	—	—
4R-1, 72-73	280.72	9.17	76.4	—	—	—
4R-1, 115-116	281.15	3.81	31.8	0.3	—	—
4R-3, 71-72	283.71	10.15	84.6	—	—	—
4R-5, 66-67	286.66	8.30	69.2	—	—	—
5R-1, 69-71	290.29	9.51	79.2	—	—	—
5R-1, 101-103	290.61	10.33	86.0	—	—	—
5R-2, 4-5	290.84	7.72	64.3	0.1	—	—
6R-1, 82-83	300.02	7.96	66.3	—	—	—
6R-2, 40-41	301.1	8.00	66.6	—	—	—
9R-1, 4-5	328.14	7.15	59.6	0.1	—	—
9R-1, 16-17	328.26	6.17	51.4	0.3	0.05	6.8
9R-1, 47-49	328.57	8.30	69.2	0.2	—	—
10R-CC, 18-19	337.88	0.15	1.2	0.2	0.09	2.1
12R-CC, 7-8	356.87	6.28	52.3	0.3	0.06	4.8
16R-CC, 14-15	395.44	0.48	4.0	0.2	0.06	3.8
17R-1, 14-16	405.04	0.84	7.0	0.6	0.08	7.7
18R-1, 20-21	424.4	0.41	3.4	0.6	0.07	8.9
22R-1, 39-41	482.59	0.38	3.1	0.5	0.08	5.9
23R-1, 10-11	501.6	6.70	55.8	0.8	0.04	20.1
24R-1, 36-38	521.16	0.15	1.3	0.2	0.09	2.4
26R-1, 38-39	540.38	0.09	0.8	0.1	0.06	2.0
27R-1, 54-55	550.24	0.09	0.7	0.8	0.06	12.8
27R-2, 78-80	551.98	0.65	5.4	0.9	0.09	9.5
28R-1, 69-70	559.99	1.93	16.0	0.7	0.11	6.1
29R-1, 81-83	569.71	0.09	0.7	0.5	0.05	9.9
30R-1, 80-82	579.3	0.05	0.4	0.3	0.05	6.8
31R-1, 48-50	588.58	0.11	0.9	0.1	0.04	2.5
32R-1, 136-138	599.06	0.07	0.6	0.1	0.06	1.7
33R-1, 37-38	607.77	1.63	13.6	0.8	0.07	11.2
33R-2, 73-75	609.58	0.67	5.6	0.6	0.06	10.8
34R-1, 104-106	618.14	0.09	0.7	0.2	0.07	3.2
35R-1, 5-6	626.75	2.24	18.6	—	0.05	—

Note: — = concentrations were below detection limit.

Acoustic Velocities

Acoustic velocities were measured in split core samples and discrete samples using the Hamilton Frame Velocimeter. Where enough

Table 8. Methane concentrations in headspace gases from Site 1065.

Core, section, interval (cm)	Depth (mbsf)	Methane (ppm)
173-1065A-		
1R-2, 0-2	252.50	3
2R-1, 145-150	262.15	5
3R-2, 0-2	271.80	4
4R-3, 0-2	283.00	2
5R-2, 30-32	291.10	2
6R-3, 20-22	302.40	2
13R-1, 0-2	371.00	3
17R-1, 52-54	405.42	3
18R-1, 42-43	424.62	6
22R-1, 54-55	482.74	5
23R-1, 22-24	501.72	4
24R-1, 1-2	520.81	3
26R-1, 61-62	540.61	3
27R-2, 0-1	551.20	3
28R-1, 79-80	560.09	4
29R-1, 5-7	568.95	4
30R-1, 144-145	579.94	3
31R-2, 106-107	590.64	4
32R-1, 146-147	599.16	3
33R-2, 84-86	609.69	4
34R-1, 5-6	617.15	4
35R-1, 0-2	626.70	3

Note: Methane concentrations in all samples are close to the minimum detection limit. No heavier hydrocarbons were found in any of the gas samples.

Table 9. Interstitial water chemistry data for Site 1065.

Core, section, interval (cm)	Depth (mbsf)	SO_4^{2-} (mM)	K^+ (mM)	Cl^- (mM)	Ca^{2+} (mM)	Mg^{2+} (mM)	Na^+ (mM)
173-1065A-							
1R-1, 145-150	252.45	6.9	5.9	552	24.7	25.2	447
4R-2, 140-150	282.90	6.2	5.4	548	24.8	24.5	450

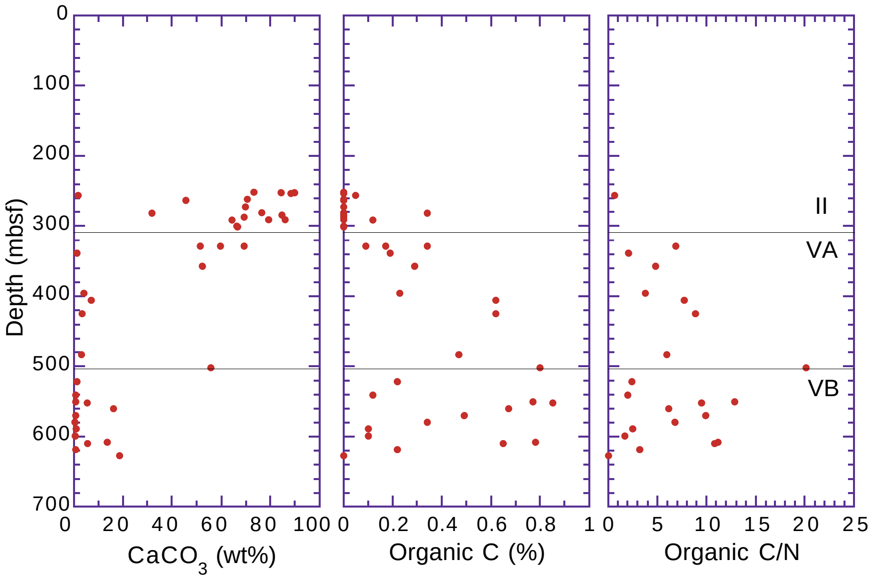

Figure 24. Downhole plots of $CaCO_3$, organic carbon, and organic C/N values in sediments from Hole 1065A in lithostratigraphic Unit II and Subunits VA and VB.

Table 10. Index properties data from Hole 1065A.

Core, section, interval (cm)	Depth (mbsf)	Bulk density (g/cm^3)	Grain density (g/cm^3)	Porosity (%)	Water content (% dry mass)
173-1065A-					
1R-1, 71-73	251.725	1.98	2.69	43	22.24
1R-2, 74-76	253.26	2.04	2.69	39	19.81
1R-4, 72-74	256.24	1.71	2.58	56	33.49
2R-1, 72-74	261.44	2.21	2.73	30	14.10
2R-2, 26-28	262.48	2.19	2.72	31	14.72
2R-2, 74-76	262.96	1.95	2.73	46	23.90
3R-1, 94-96	271.26	2.08	2.80	41	20.00
3R-2, 68-70	272.5	2.13	2.72	35	16.98
4R-1, 70-72	280.72	2.05	2.76	41	20.49
4R-3, 70-72	283.72	2.03	2.70	40	20.32
4R-5, 66-68	286.68	1.98	2.69	42	21.96
5R-1, 70-72	290.32	1.99	2.71	43	21.87
6R-1, 78-80	300	2.15	2.72	34	15.94
6R-2, 38-40	301.1	2.18	2.72	32	15.06
7R-CC, 0-3	308.83	2.13	2.78	37	17.97
9R-1, 14-15	328.25	2.00	2.84	20	8.25
9R-1, 39-42	328.52	2.02	2.80	5	1.76
10R-CC, 9-11	337.81	2.03	2.78	38	18.26
11R-CC, 0-3	347.33	2.07	2.76	43	21.64
11R-CC, 21-23	347.53	2.09	3.19	18	6.67
13R-1, 8-10	371.1	2.12	2.75	37	17.73
14R-CC, 8-10	376.1	2.12	2.75	37	17.79
16R-CC, 22-24	395.54	2.12	2.72	41	20.56
17R-1, 11-13	405.03	2.13	2.77	40	19.95
17R-CC, 15-17	405.61	2.20	2.76	44	22.43
18R-1, 20-22	424.42	2.48	2.83	41	19.93
22R-1, 44-46	482.66	2.72	2.82	35	16.24
22R-CC, 3-5	482.8	2.80	2.77	37	17.58
23R-1, 8-10	501.6	2.73	2.77	2	0.86
23R-1, 55-57	502.07	2.66	2.77	6	2.44
24R-1, 37-39	521.19	2.40	2.77	21	9.13
26R-1, 38-40	540.4	2.22	2.75	31	14.25
27R-1, 52-54	550.24	2.37	2.77	23	9.90
27R-1, 112-114	550.84	2.38	2.80	24	10.28
27R-2, 81-83	552.03	2.51	2.78	16	6.45
28R-1, 71-73	560.03	2.58	2.80	13	5.03
29R-1, 82-84	569.74	2.38	2.75	21	9.07
30R-1, 81-83	579.33	2.35	2.77	24	10.40
31R-1, 48-50	588.6	2.38	2.78	22	9.61
32R-1, 136-138	599.08	2.46	2.78	18	7.57
33R-1, 38-40	607.8	2.51	2.78	16	6.39
33R-2, 72-74	609.59	2.38	2.80	23	10.00
34R-1, 104-106	618.16	2.44	2.77	18	7.75
35R-1, 3-5	626.75	2.38	2.76	22	9.39

core existed, measurements were made on every section (Table 12). Discrete samples were cored (2.54 cm diameter cylinders) and their ends were trimmed parallel to minimize wave traveltime error. Split core sections were measured in the core liner, and corrections were made for the increased wave traveltime and travel path caused by the presence of the liner.

The velocity data are consistent with the bulk density and porosity measurements for Hole 1065A. The velocities for Unit II and Subunit VA cluster around 2.0 km/s, while there is a sharp increase in compressional-wave velocity at the Subunit VA/VB boundary (501.58 mbsf; Fig. 27). This increase in velocity is thought to indicate acoustic basement at this site. In Subunit VB velocities are more scattered but average 2.8 km/s. The velocity-depth profile in Figure 27 also displays several velocities above 4 km/s. These high velocity layers consist of well-cemented massive limestones that are present intermittently in Unit II and Subunit VA but more frequently in Subunit VB.

Multisensor Track

Despite the many measurements taken with the MST, the data for Site 1065 were not used to determine rock physical properties. Because the four MST sensors take measurements on whole cores through a core liner, their accuracy relies on soft-sediment lithologies that are continuous and completely fill their core liner. If recovered core does not fill the core liner, then sensor-core coupling and the resultant data are compromised. Furthermore, if the rock core is discontinuous, volume-dependent measurements, such as GRAPE density

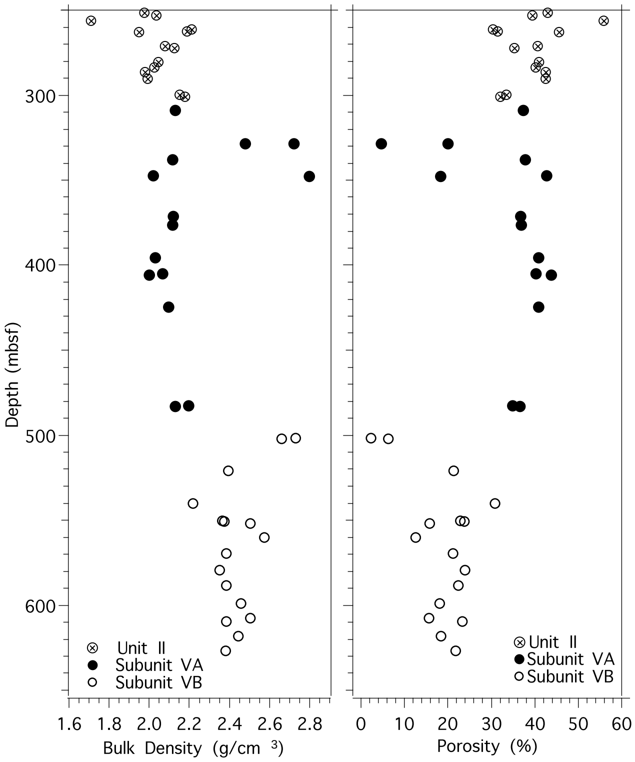

Figure 25. Bulk density and porosity vs. depth in Hole 1065A.

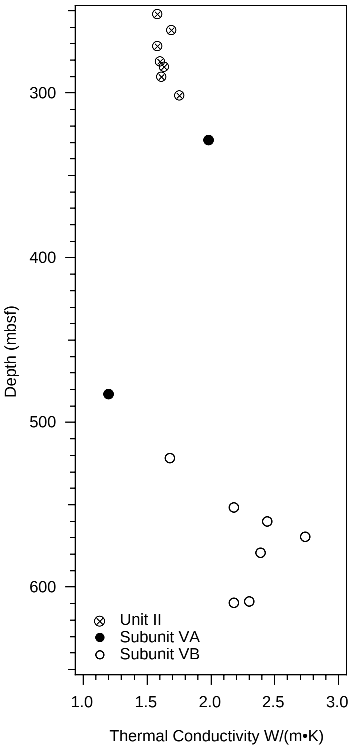

Figure 26. Thermal conductivity vs. depth in Hole 1065A.

and compressional-wave velocity, suffer. At Site 1065, no soft sediment was recovered; therefore, MST measurements were completed on discontinuous, partially and totally lithified rock cores that incompletely filled core liners. Consequently, data from the MST were inaccurate and highly scattered. For reference, Tables 13 through 16 (on CD-ROM, back pocket, this volume) contain MST data.

DOWNHOLE MEASUREMENTS

After drilling and coring Hole 1065A to a total depth of 5412 mbrf (631 mbsf) using an RCB coring system, a complete wiper trip was made to condition the hole for logging. Additional cuttings were removed from the borehole by circulating sepiolite mud (see "Operations" section, this chapter).

Table 12. Compressional-wave velocity data from Hole 1065A.

Core, section, interval (cm)	Depth (mbsf)	Velocity (m/s)
173-1065A-		
1R-1, 70	251.70	1952
1R-2, 71	253.21	2156
1R-3, 72	254.72	1905
2R-1, 75	261.45	2042
2R-2, 76	262.96	1833
2R-2, 24	262.44	1926
3R-1, 91	271.21	1950
3R-2, 80	272.60	2041
4R-1, 70	280.70	1927
4R-2, 69	282.19	1915
4R-3, 71	283.71	1927
4R-4, 71	285.21	2022
4R-5, 65	286.65	1923
5R-1, 71	290.31	1976
6R-1, 80	300.00	2059
6R-2, 40	301.10	2060
9R-1, 15	328.25	2969
9R-1, 47	328.57	5721
14R-CC, 20	376.20	1727
17R-1, 16	405.06	1773
18R-1, 13	424.33	1817
22R-CC, 19	482.94	4167
22R-CC, 5	482.80	1722
23R-1, 55	502.05	4176
23R-1, 8	501.58	5491
24R-1, 37	521.17	2177
25R-CC, 5	530.45	5239
26R-1, 34	540.34	1977
27R-1, 115	550.85	2269
27R-1, 55	550.25	2259
27R-2, 82	552.02	2593
28R-1, 72	560.02	3323
29R-1, 82	569.72	2377
30R-1, 82	579.32	2143
31R-1, 48	588.58	2306
32R-1, 136	599.06	2600
33R-1, 128	608.68	2530
33R-2, 68	609.53	2405
33R-1, 38	607.78	2763
33R-2, 73	609.58	2208
34R-1, 104	618.14	2770

Wireline logging operations began in Hole 1065A at 5:30 GMT on 30 April 1997. All logging operations were completed by 1:00 on 1 May, for a total logging time of 19.5 hours. The triple combination and FMS-sonic logging tool strings were run at Site 1065 (see "Downhole Measurements" section, "Explanatory Notes" chapter, this volume). Each tool string was run to the bottom of the hole, with high-resolution log data being acquired during an upward transit at speeds of 300 to 600 m/hr. An overview of the logging operations can be seen in Table 17. Because of bridging complications during the first tool run, the pipe was lowered for the second tool run (see Table 18 for logging and drilling depth information).

The first run with the triple combination tool string, included from top to bottom, the telemetry cartridge, HNGS, APS, HLDT, DIT, and TLT. The majority of data collected by the triple combination are of good quality even though the hole was washed out to >16 in over the majority of the logged interval (Fig. 28). The HLDT caliper arm was

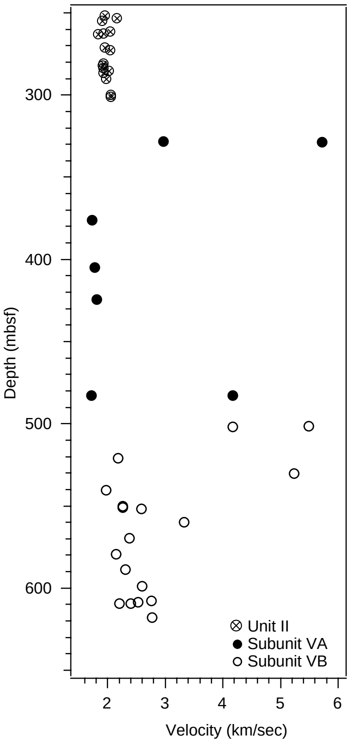

Figure 27. Compressional-wave velocity vs. depth in Hole 1065A.

Table 17. Logging operations at Site 1065.

Date	Time (GMT)	Activity
4/30/97	5:30	Rig up wireline and triple combination tool string
	6:30	Run in hole with triple combination (TLT/DIT/HLDT/APS/HNGS)
	10:00	Began upward log from total depth (TD)
	10:50	Encountered bridge at 5100 mbrf, which took 1.5 hours to pass.
	12:30	Continue to log to pipe depth (PD; 4887 mbrf) with loss of APS and caliper function
	13:30	Complete repeat section from bridge to PD with APS restarted and caliper functioning
	14:00	Tool entered pipe and was run to seafloor with HNGS running
	16:00	Tool out of drill string and rig down
	17:00	Lower pipe to below bridge (new PD 5128 mbrf)
	18:00	Rig up FMS tool string (FMS/SDT/NGT)
	18:45	Run in hole with FMS string to TD
	20:55	Log up with FMS tool string to PD
	21:45	Close calipers and enter pipe
5/1/97	0:30	Tool out of drill string
	1:00	End of logging operation

Table 18. Depth parameters at Site 1065 from log and drilling operations.

Tool run	Operation depth	Depth (mbrf)
1	Driller's depth	5412
	Logger's depth	5402
	Driller's pipe	4887
	Logger's pipe	4885
	Driller's seafloor	4781
	Logger's seafloor	4778
2	Driller's pipe	5128
	Logger's pipe	5131

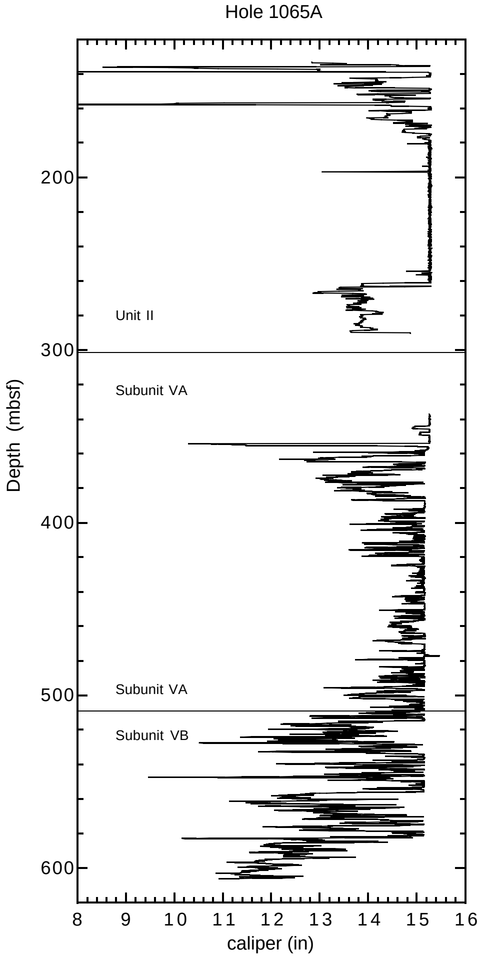

Figure 28. Width of Hole 1065A as measured by the two calipers (average value is displayed) of the FMS tool between 605 and 354 mbsf, and by the HLDT caliper between 354 and 338 mbsf (main pass) and between 290 and 140 mbsf (repeat pass).

fully extended; however, the tools were not necessarily eccentralized, which may affect the accuracy of some of the measurements, in particular, the HLDT and APS readings. During the up-log, the tool became stuck at 5100 mbrf (319 mbsf). The caliper was closed and the tool was worked for ~1.5 hr before the bridge was passed. During this time, a voltage spike caused the tool to lose telemetry, causing the APS to reset. The remainder of the hole was logged without the APS and with the caliper closed (to assess hole conditions and minimize the risk of more sticking). A repeat section was logged over this interval with the APS functioning and the caliper open.

The second run showed the borehole to be larger than the maximum caliper reading of the FMS (greater than 15 in) above 510 mbsf and very irregular between 510 and 600 mbsf (Fig. 28). However, some usable FMS images were recorded in a few intervals where the hole was not so badly washed out. Analog sonic data were also affected by the large, irregular hole size, causing signals to be somewhat weak and noisy.

The results of standard shorebased log processing are in Section 7, "Shorebased Processed Logs" (CD-ROM, back pocket, this volume).

Geophysical Logging Data

Downhole measurements from Hole 1065A provide geophysical and geochemical (U, Th, K) data, covering the interval from 600 to 100 mbsf. Sonic data were recorded in only the lowest part of the hole, from 600 to 350 mbsf. Poor core recovery (~12%) prevents accurate core-log integration; these logs, however, provide valuable information to complement the lithostratigraphy determined from cores and in the drilled interval between 100 and 250 mbsf. All logging data were shifted from meters below rig floor to meters below seafloor using the driller's water depth (4781 m) for preliminary shipboard analysis. The postcruise comparison of the natural gamma-ray data from both tool strings provided new depth-shifted data (Figs. 29, 30).

The boundaries between lithostratigraphic Unit II and Subunits VA and VB (see "Lithostratigraphy" section, this chapter) can be clearly identified from the logging data, allowing the unit boundaries to be estimated more accurately. The boundary between Units II and V, located at 308.8 mbsf from the cores is identified at 303 mbsf from the logging data (Figs. 29, 30). The boundary is marked by a sharp increase of the natural gamma-ray activity and a sharp decrease of the resistivity, density (only in the top 2 m), and photoelectric effect factor (PEF).

Above lithostratigraphic Unit II (251 to 308.8 mbsf), other units or subunits can be inferred from changes in the logging data. For example, above ~200 mbsf the resistivity curves have a constant baseline of about 1 Ωm, which increases slightly and regularly up to 2 Ωm at the bottom of lithostratigraphic Unit II.

Strong variations of natural gamma ray are present in the top 300 m of the hole (Fig. 29). Natural gamma-ray peaks caused mainly by increasing concentrations of thorium are considered to be indicators of clay minerals (Serra, 1986). Above the cored interval, increases in gamma-ray activity are correlated with increased resistivity and density and with decreased porosity. Thus, intervals with high gamma-ray counts may correspond to more compacted, clay-bearing layers that alternate with less lithified, more porous pelagic sediments. We propose that much of the upper sedimentary section of Hole 1065A corresponds to lithostratigraphic Unit I (nannofossil ooze, nannofossil clay, clay) as defined during Leg 149 at Site 900 (located 23 km to the west-southwest of Site 1065; Shipboard Scientific Party, 1994c; see Fig. 5).

Lithostratigraphic Unit II comprises nannofossil chalk (dominant) and nannofossil clay (see "Lithostratigraphy" section, this chapter). Logging data identifies its upper boundary between 200 and 230 mbsf (Figs. 29, 30). In contrast to Unit I, most of the data are in antiphase to the natural gamma-ray data. Low gamma-ray counts correspond to high resistivity and density and to low porosity. The photoelectric effect, which is typically a good indicator of lithologic changes, does not clearly define the lithostratigraphic intervals in Unit I; it does, however, present strong in-phase variations with the other data in Unit II. Between 258 and 263 mbsf, and between 239 and 245 mbsf, high gamma-ray values correspond to high porosity and to low resistivity, density, and PEF (~2), which may correspond to clay-rich

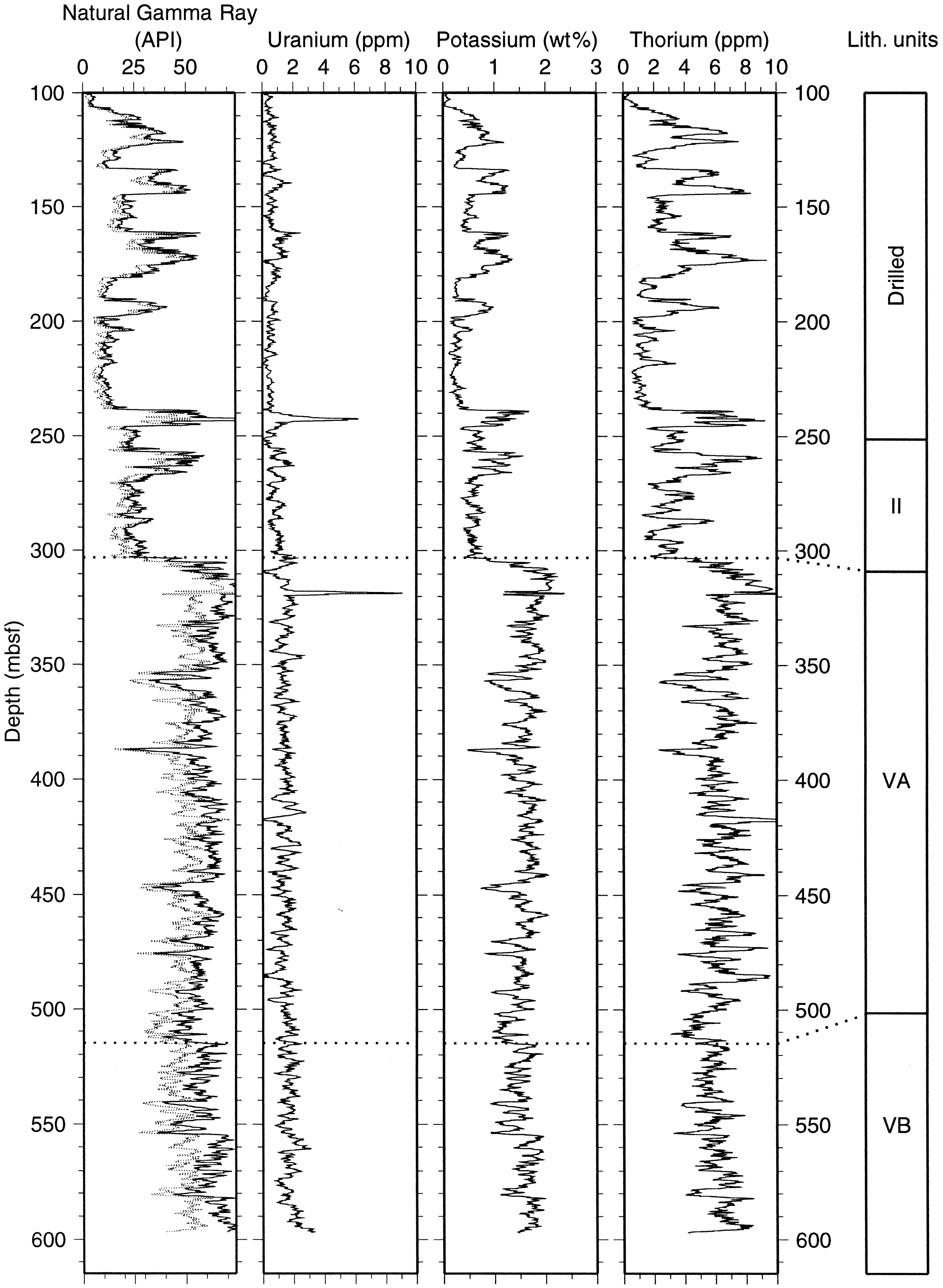

Figure 29. Hole 1065A downhole logs from the HNGS natural gamma-ray tool: natural gamma ray (continuous line = total gamma ray, dotted line = computed gamma ray [total gamma ray minus uranium]), uranium, potassium, and thorium. Depths are in mbsf. Lithostratigraphic units are from the "Lithostratigraphy" section, this chapter. Horizontal dotted lines represent the proposed lithostratigraphic unit boundaries inferred from logging data.

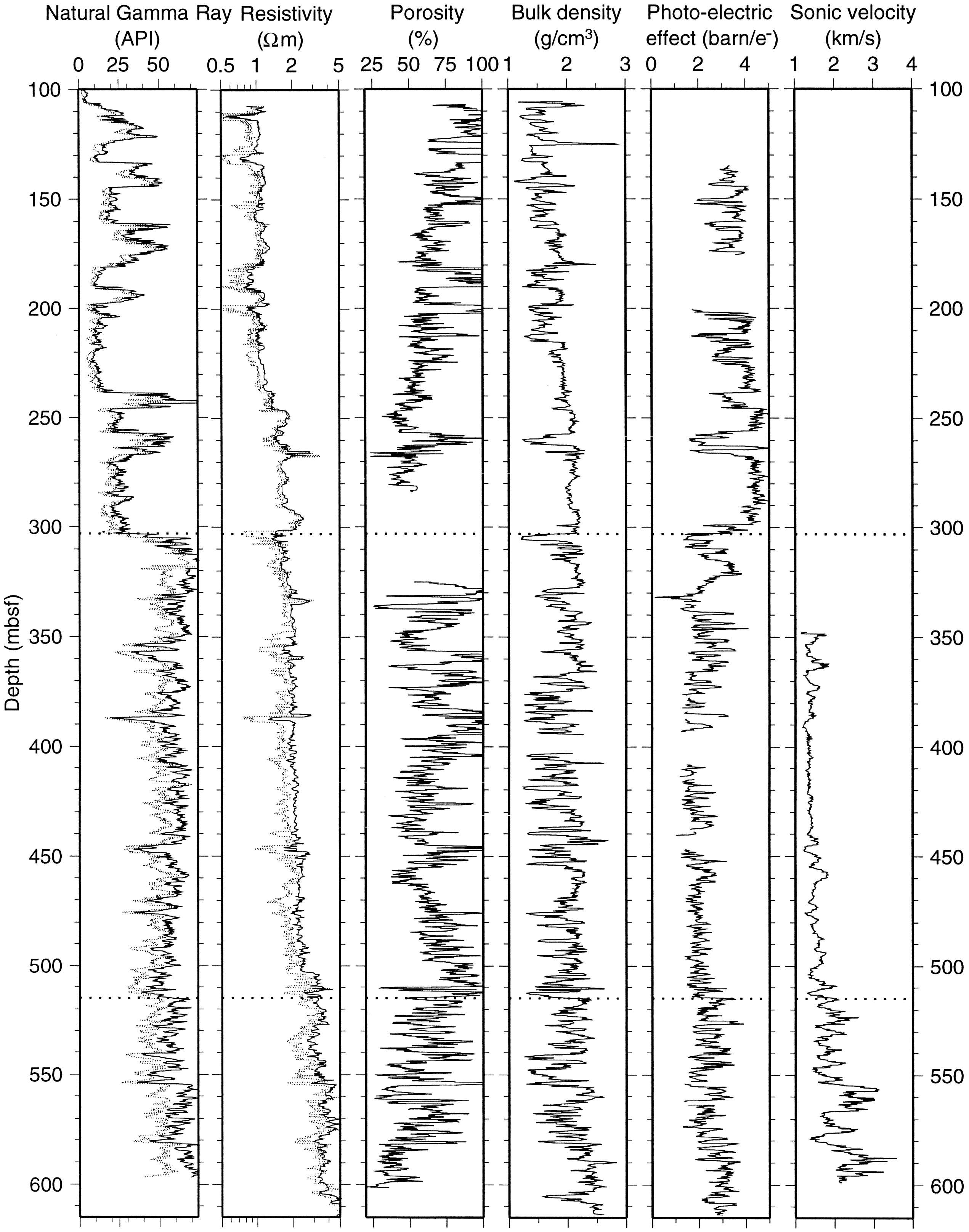

Figure 30. Downhole logs of natural gamma ray and resistivity (main run; ILD = continuous line; SFLU = dotted line), porosity (main run below 300 m and repeat run above), bulk density (main run), photoelectric effect factor (main run below 300 m and repeat run above), and velocity from Hole 1065A. Dotted lines represent the proposed lithostratigraphic units boundaries inferred from logging data.

layers. Between 264 and 268 mbsf, the gamma-ray peak corresponds to a low PEF of 2, high resistivity, and a lower porosity. This layer is probably also constituted of clay, but in a more indurated form. This depth corresponds also to a lower value of caliper, which can modify some of the data. The dominant value of PEF in Unit II is >4, which could correspond to the presence of calcite which has a PEF of ~5, whereas the layers interpreted as clay have a PEF of ~2, typical of kaolinite or montmorillonite. Thus, the logging data are consistent with the dominant presence of chalk associated with interbedded clay-rich layers in lithostratigraphic Unit II.

The boundary between lithostratigraphic Units II and V is characterized by a sharp increase in natural gamma-ray activity (mainly thorium and potassium), reduced resistivity and PEF, and a lower density for the upper 2 m. No porosity data are available at this boundary. No clear variations can be seen in the logging data in Unit V, except for porosity. Variations of PEF observed from 300 to 330 mbsf are probably associated with the closing of the HLDT caliper and therefore may not be valid. The density, resistivity, and velocity below 350 mbsf all show slight increases with depth. Physical properties data show more significant changes (see "Physical Properties" section, this chapter), suggesting that the logging data were affected by hole rugosity. High gamma-ray counts in lithostratigraphic Unit V correspond to the presence of clay, which is the dominant lithology described from cores. Localized low values (358, 387, 448 mbsf) are observed in the gamma-ray log and can be associated with low resistivity peaks. Changes in some curves at 515 mbsf may correspond to the boundary between Subunits VA and VB, picked at 500 mbsf from core observations. Lithostratigraphic Subunit VB is characterized by slightly increased gamma-ray counts, decreased porosity, a narrower hole (caliper), and by higher amplitudes in the velocity, PEF, and resistivity logs. These changes may be linked to the more indurated and lithified claystone recovered in Subunit VB.

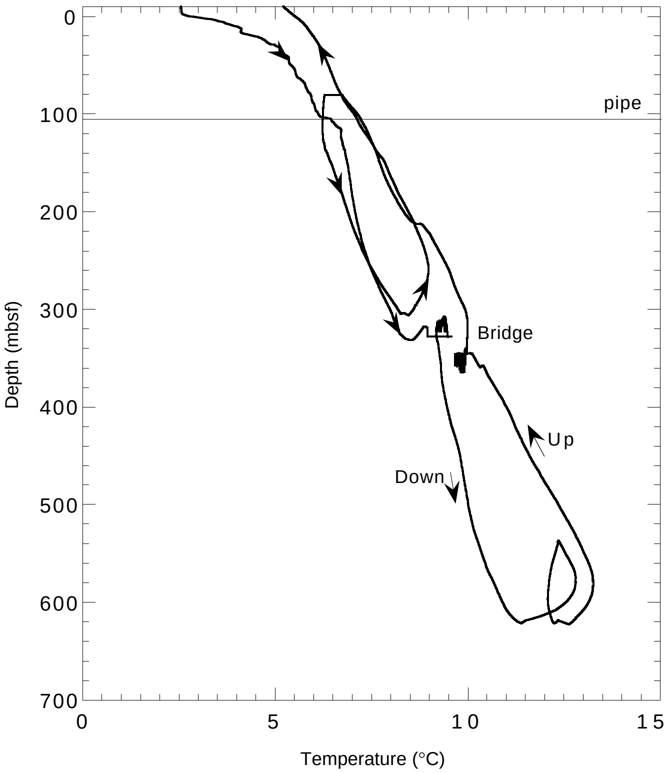

Figure 31. Temperature log from the TLT at the base of the triple combination tool string. The horizontal line represents the pipe depth.

Borehole Temperature

Figure 31 shows the temperature vs. depth profile for the main and repeat runs of the triple combination tool string. The temperature data are not representative of a thermal equilibrium with the formation because of the disturbance created during drilling operations associated with fluid circulation. The temperature gradient is constant over the complete logged interval; however, these data indicate a lower geothermal gradient (13.6°C/km) than normal, which may be due to the fact that the hole had not reached thermal equilibration.

Structural Measurements from FMS Data

FMS data indicate that the hole was slightly deviated from the vertical. The mean deviation increased from 1.1° at 350 mbsf to 1.3° at 515 mbsf, reaching a maximum of 2° between 530 and 560 mbsf, and then decreased again downhole to 1° at 600 mbsf (Fig. 32). In the same interval, the average azimuth varied linearly from northwest at 350 mbsf to northeast at 600 mbsf; however, a stable azimuth (015°) was recorded between 510 and 550 mbsf (top of Subunit VB; Fig. 32). Because of the bad shape of the hole, the present state of stress cannot be determined from borehole elongation. Moreover, no breakouts were observed on FMS images.

Preliminary shipboard processing of FMS images was performed using Schlumberger's Geoframe software. The images were enhanced by histogram (static and dynamic normalization) equalization after undergoing depth and voltage corrections. Images were used to determine the dip and azimuth of sedimentary bedding.

Because of the poor shape of the borehole, only a few intervals provide reliable FMS data. Extended intervals include 364–374 mbsf (lithostratigraphic Subunit VA), 558–562 mbsf, and 594–606 mbsf (Subunit VB). In these intervals, we measured the true dips and azimuths of sedimentary layers (Fig. 33). No significant differences were identified between Subunit VA and the upper part of Subunit VB. Between 360 and 570 mbsf, most dips range from 10° to 20°, with azimuths from 045° (northeast) to 090° (east). Below 570 mbsf, average dips increased to values between 20° and 40°. Azimuths are also seen to change from 000°–020° (north) at 586 mbsf, to 100°–130° (east-southeast) at 595 mbsf, and 080°–110° (east) at 600–605 mbsf. At a large scale, rapid changes in bedding orientation are seen that are probably related to sedimentary features. For example, Figure 34 shows a cross-bedded set (dip decreasing downhole) at the bottom of Subunit VB.

The FMS inclinometer measurements display relatively high-frequency (short-wavelength) variations (e.g., Fig. 32). We performed spectral analyses on three independent records (hole deviation, hole azimuth, pad 1 azimuth). The three analyses exhibit similar 36- and 72-s periods, which are probably harmonics from shorter periods generated by the ship heave.

SUMMARY AND CONCLUSIONS

Summary

Site 1065 is located in the southern Iberia Abyssal Plain over a roughly north-south basement high covered by a 300-m-thick postrift sedimentary cover. This high seems to be the southern prolongation of a ridge on the eastern part of the Vasco da Gama Seamount, which lies on the southern slope of Galicia Bank. The ridge is buried under abyssal plain sediments 8 km north of the site. At Site 1065, the basement high presents a tilted block geometry on the 098°-trending CAM144 seismic reflection line; it is capped on its eastern flank by a tilted "transparent" layer of Middle–Upper Jurassic sediments and its western flank is bounded by an oceanward-dipping normal fault with a throw of about 6000 m. Further west, the basement is dissected into a series of smaller basement highs clearly bounded by west-dipping listric normal faults, which flatten at a depth of 9.5–10 s TWT.

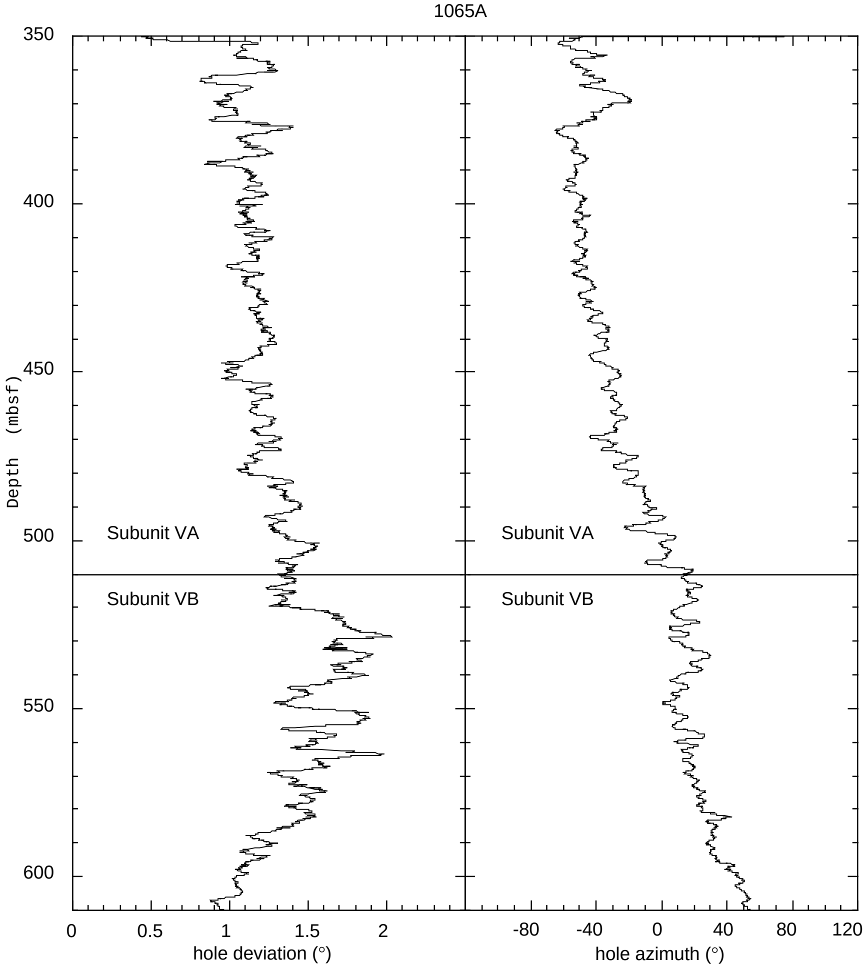

Figure 32. Deviation and azimuth of Hole 1065A in the interval logged by the FMS. Deviation and azimuth are by reference to the vertical and north, respectively.

None of these flat-lying intracrustal reflectors curves back up to the top of the basement, unlike the H reflector observed farther south on the Lusigal-12 reflection profile. These blocks differ, however, from the Site 1065 block in that their asymmetric shape is not emphasized by a "transparent" sedimentary layer at the top of their eastern flank. This suggests that the Site 1065 high is at the westernmost limit of the Mesozoic marginal basin formed in the Late Jurassic off Iberia and that it should be the westernmost large block of continental crust. The CAM144 line ends just eastward of Site 1065 and gives no information about the relationships with basement structures further east.

Five kilometers southward, the geometry of the basement highs appears different on the east-west Lusigal-12 reflection profile (Fig. 7, "Introduction" chapter, this volume). This indicates that, although grossly north-south oriented, the extensional structures are not cylindrical. The southward prolongation of the Site 1065 basement high is deeper and does not display a clear overall asymmetric shape. It is dissected by internal faults delineating a small basin at the top of the high. It is, however, limited by a westward-dipping normal fault, which may join or intersect the H reflector at depth. This H reflector has been interpreted as a major synrift tectonic contact along which deep lithospheric levels were exposed at Site 900. In between these two highs, two smaller blocks appear to have been tilted toward the east along the H reflector. The fan-shaped sediments that cover their eastern flank do not display the same "transparent" seismic facies as at Sites 1065 or 901. Eastward, Site 901 is located on a tilted block similar to that of Site 1065, but is shallower. Its westward-bounding fault (L) appears to be a listric fault on the time-migrated section, flattening at around 10.5 s two-way traveltime (TWT) beneath the Site 1065 fault block. Swath bathymetry near Site 901 shows that the L escarpment has a north-south strike. The regional stress, which led to the reactivation of a set of northeast-southwest Variscan faults with transcurrent motion that appear to have controlled the formation of Mesozoic basins (Wilson et al., 1989), may have caused a wrench component of movement along this fault. This could explain some of the dip variation in the tilted Jurassic sediments at the top of the high (see below).

The sedimentary history of this site probably began in the Middle–Late Jurassic at a paleolatitude of about 23°N, based on shipboard paleomagnetic inclination measurements. The clays, claystones, dolomitic claystones, sandstones, and conglomerates of lithostratigraphic Subunit VB were followed by the dark greenish gray plastic clay characteristic of Subunit VA, which has minor amounts of calcareous claystone and siltstone, medium to coarse sandstone, and conglomerate. All the silt and much of the clay fraction was deposited by low-density turbidity currents, although a hemipelagic origin cannot be ruled out for some of the sediments. Features in the sediment indicate disaerobic bottom conditions. The lithoclastic sands and conglomerates were also deposited by turbidity currents, and their clasts indicate that contemporaneous erosion of Variscan basement rocks was going on in the vicinity, possibly on the highs to the north of the site. A thin slump-folded interval occurred near the base of lithostratigraphic Unit V. The depositional environment was below wavebase but in an offshore shelf situation.

In the time interval between the Late Jurassic (Tithonian) and the early Miocene, the Jurassic sediments underwent substantial tilting with an approximate net 20° dip to the northeast. This was probably the result of the final Early Cretaceous phase of rifting on this margin but, in view of the uncertainty in dating the lower 165 m of Unit V,

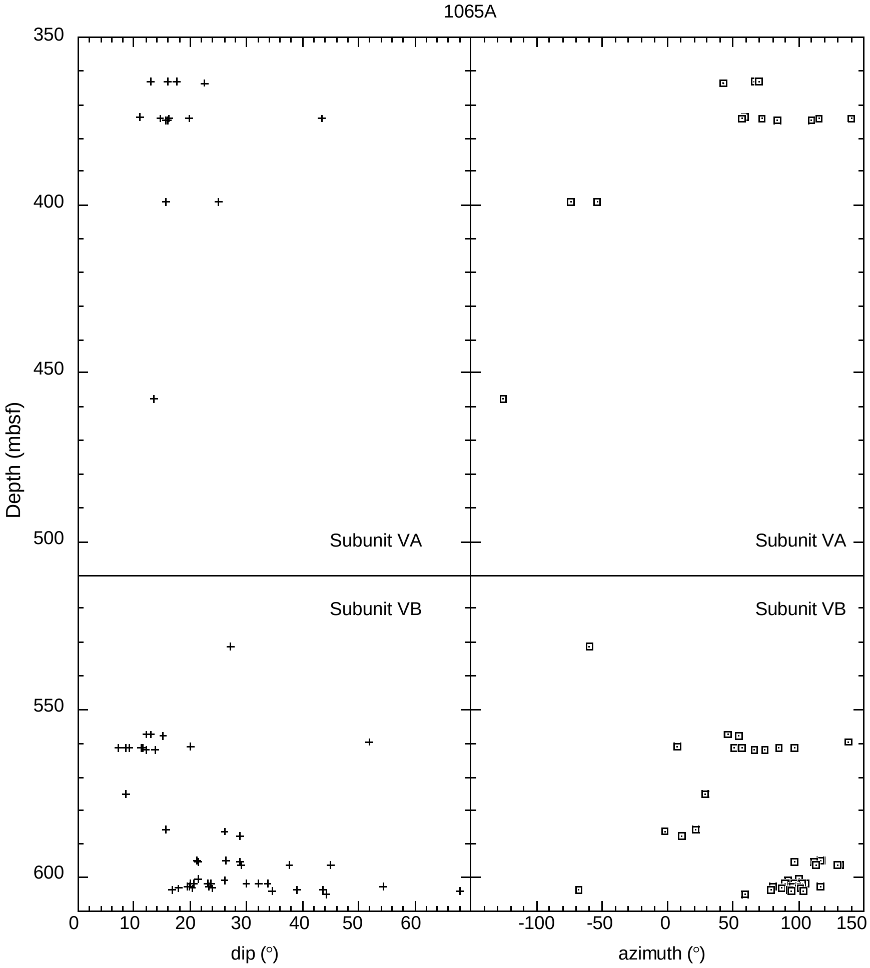

Figure 33. True dips (crosses) and azimuths (squares) of bedding logged by the FMS in Hole 1065A.

may have included some tilting contemporaneous with the previous phase of rifting, known from the onshore Lusitanian Basin, which occurred in late Oxfordian/early Kimmeridgian times. However, there is no clear indication, in either the cores or the seismic section, of a systematic increase in dip toward the base of, or within, Unit V to substantiate this hypothesis.

No sediments deposited unequivocally during the Tithonian–Miocene hiatus have been recognized, but recovery near the lithostratigraphic Unit II/Unit V boundary was very poor and they may have been missed. An unfossiliferous yellowish sandy claystone from Sample 173-1065A-7R-CC, possibly from the Cretaceous or uppermost Jurassic, could be nonmarine on account of its highly oxidized state. However, even if the site had not been subaerial for a time, substantial thermal subsidence of the Jurassic shelf sediments in excess of 4500 m must have occurred before the site was inundated by Cenozoic sedimentation not earlier than 24 Ma.

Cenozoic sedimentation at the site began with the deposition of early Miocene nannofossil chalk, with siliceous allochems, and claystone. These sediments were deposited from suspension as pelagites and hemipelagites, with possibly some deposition from low-density turbidity flows. The sediments also include 2- to 40-mm clasts composed of lithologies characteristic of the Iberian Hercynian basement and of Upper Jurassic/Lower Cretaceous shallow-water limestones. A slump occurred sometime before 16.4 Ma, giving rise to a layer of deformed chalk ~60 m thick. The youngest cored sediment is late early Miocene in age (foraminiferal zone M4a, nannofossil zone NN4).

The seismic profile across the site shows a seismically weakly reflective “transparent” layer that corresponds to lithostratigraphic Subunit VA, the top of which is approximately conformable with the dip slope of the tilted fault block that it overlies. While the apparent dip on the seismic depth section of the base of the transparent layer is about 14° in the direction 097°, it is interesting to see what independent estimates can be made from other observations such as paleomagnetism and FMS images. The dip angle will constrain the tilt history of the block and the nature and extent of the faults that bound it.

In the following discussion it is assumed, perhaps not always correctly, that the original bedding planes were laid down horizontally and compacted uniformly, so that one may deduce that the net deviation away from horizontal of the bedding planes since the Late Jurassic is the same as that experienced by the underlying fault block.

Measurements of dipping beds in the split cores of lithostratigraphic Unit V revealed a mean dip of 18° with a standard deviation of 10° relative to the core reference frame. Similarly, images acquired with the CoreScan device of dipping planes on the outside of whole cores indicate maximum dips of 10°–30° relative to the core reference frame. However, all such observations depend on how much the hole deviates from the vertical and they cannot independently provide the azimuthal direction of any dip. The hole deviation in Unit V, measured by the FMS tool, is about 1°–2° in a northeast direction, which would require some minor correction of the apparent dips mentioned above if the geographic orientation of the cores was known.

Analysis of the FMS images of bedding planes, corrected for hole deviation, gave absolute dips and azimuths in the range 10°–40° and 000°–130°, respectively (Table 19). Some of this variation appears to depend on the depth in the hole but there is also evidence that some of this variation could be caused by localized cross-bedding.

Last, the paleomagnetic NRM magnetization vector in the cores can provide an independent estimate of dip. If the NRM vector for the unfossiliferous Middle–Late Jurassic Core 173-1065A-27R is

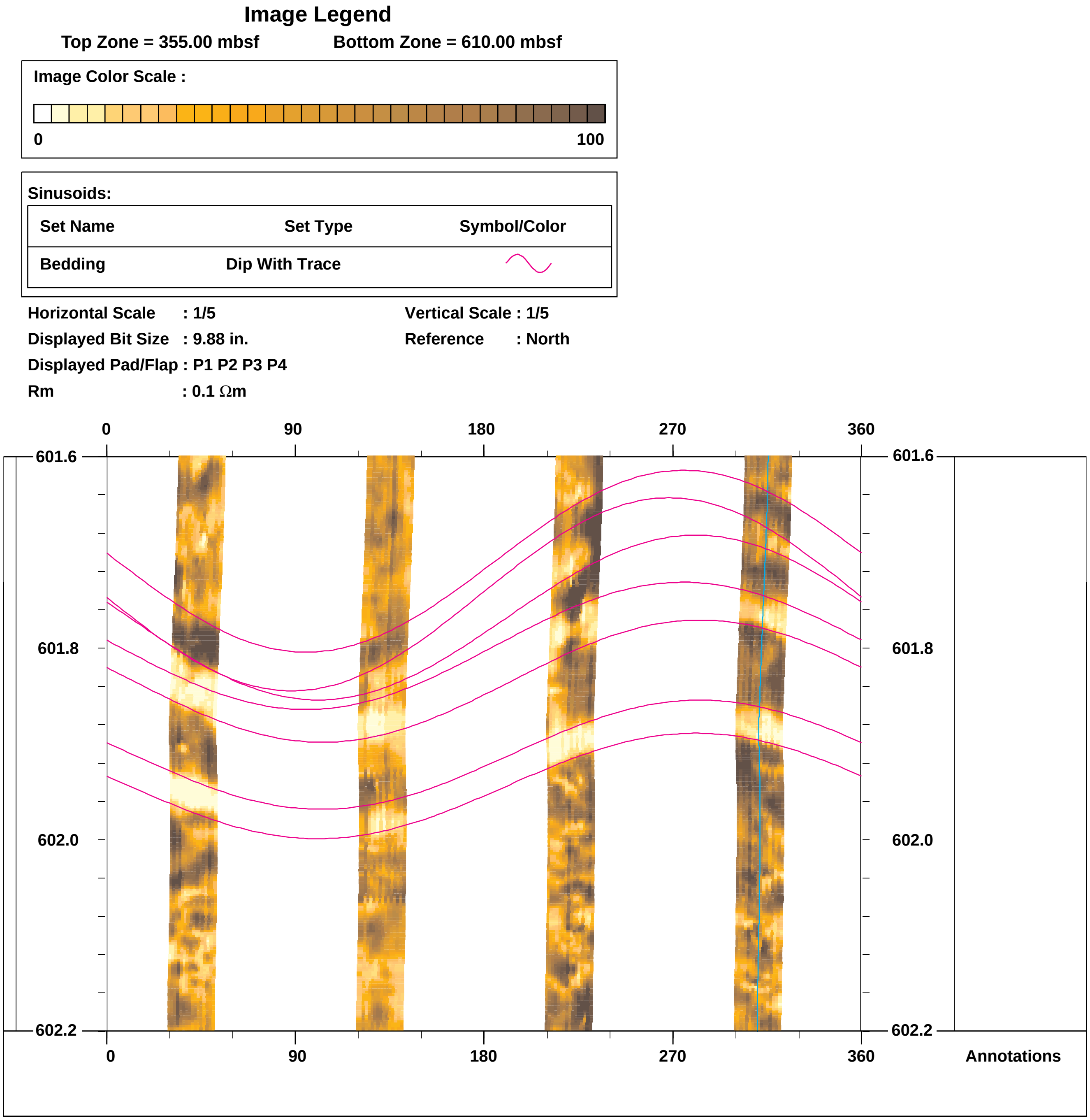

Figure 34. FMS image of part of lithostratigraphic Subunit VB (601.6–602.2 mbsf). The image is displayed without vertical exaggeration. Horizontal scale is azimuth by reference to north; vertical scale is in mbsf. The sinusoids follow the trace of the intersection between bedding and borehole. In the lower part of the image, the mottling is probably produced by burrows.

aligned with the Late Jurassic paleomagnetic pole direction for Iberia (65°N, 143°E), known from measurements on land, then the rotation that best aligns the two vectors and restores the bedding planes to horizontal provides an estimate of the present dip (25°) and dip azimuth (035°) of the bedding planes (Table 19).

It is therefore clear from Table 19 that the bedding planes dip at about 20° in a direction that varies mainly between north-northeast and northeast but that is closer to east in the lowest 30 m of lithostratigraphic Unit V. The probably imprecise estimate of apparent dip from the seismic section is consistent with a true dip of 23° to the northeast or of 14° to the east, in reasonable agreement with the above estimates.

Even though much of the logged hole was oversize, a number of significant changes occur downhole in the logs that correspond well with the lithostratigraphic unit boundaries. Based on an abrupt increase in natural gamma activity and a similar decrease in PEF and resistivity, the Unit II/Unit V boundary occurs at 303 mbsf, compared to a depth of 308.8 mbsf based on recovered cores. At ~515 mbsf, close to the Subunit VA/Subunit VB boundary, hard bands appear that leave a narrower hole diameter (caliper logs) while sonic veloc-

Table 19. Compilation of estimates of bedding plane dips and azimuths in the Middle–Upper Jurassic lithostratigraphic Unit V.

Depth (mbsf)	Dip (°)	Azimuth (°)	Source
309-631	18 ± 10	Unknown	Measurements on split cores
550-608	5-32	Unknown	Whole-round CoreScan images
360-570	10-20	045-090	FMS borehole images
586	20-40	000-020	FMS borehole images
595	20-40	100-130	FMS borehole images
600-605	20-40	080-110	FMS borehole images
522.5-549.5	25	035	Paleomagnetism

Table 20. Predicted basement depth while drilling upper lithostratigraphic Unit V.

Reflector depth (s TWT)	Observed or (predicted) depth (mbsf)	Interval velocity, computed or (assumed) (km/s)	Lithostratigraphic unit/subunit boundary
0.35	319	1.82	II/V
0.55	(619)	(3.00)	V/basement

Table 21. Predicted basement depth while drilling lithostratigraphic Subunit VB.

Reflector depth (s TWT)	Observed or (predicted) depth (mbsf)	Interval velocity, computed or (assumed) (km/s)	Lithostratigraphic unit/subunit boundary
0.35	319	1.82	II/VA
0.55	510	1.91	VA/VB
0.63	(630)	(3.00)	VB/basement

Table 22. Predicted minimum depth of crystalline basement after downhole logs were available.

Reflector depth (s TWT)	Observed or (predicted) depth (mbsf)	Interval velocity, computed or (assumed) (km/s)	Lithostratigraphic unit/subunit boundary
0.35	301	1.72	II/VA
0.55	~550	2.49	Within VB
0.63	(~670)	(3.00)	VB/crystalline basement (?)

ity, PEF, and resistivity begin to increase steadily downward and porosity decreases. Other changes within units or subunits require further investigation ashore (e.g., at 235–265, 385, and 445 mbsf). Because of the poor core recovery (mostly <10%), only discrete index measurements were made on the cores.

Drilling at this site was based on the premise that the acoustic basement reflector at 0.55 s TWT represented crystalline basement rocks. Using a velocity model derived from sonobuoy data and experience from Leg 149, the base of the postrift sediments at 0.35 s TWT was estimated to lie at 330 mbsf. The first fossiliferous Tithonian sediments were found in Core 173-1065A-8R (319 mbsf) and the downhole logs showed a significant and abrupt change in gamma ray, PEF, and resistivity at 303 mbsf. The core and log observations imply interval velocities of 1.82 and 1.72 km/s for the postrift sediments, respectively. The velocity in the Middle–Late Jurassic sediments that constitute the weakly reflective "transparent" layer was unknown. Conservatively, an interval velocity of 3.0 km/s was assumed to estimate the thickness of the layer as 300 m and hence the maximum depth to basement as 619 mbsf. This assumption seemed justified since shipboard velocity measurements on the soft clays of Subunit VA were all less than 2.0 km/s even though some harder rock fragments in the cores had higher velocities. Although some thin, hard claystone layers in Subunit VB exhibited Hamilton frame velocities in the range 3.0–5.5 km/s, these appeared to be unrepresentative of the whole subunit, which mostly had values in the range 2.0–2.8 km/s with an average of about 2.5 km/s. Thus, as the hole approached a depth of 630 mbsf without encountering crystalline basement, we formed the view that the reflector at 0.55 s TWT was a response to the velocity contrast between the mainly soft clays of lithostratigraphic Subunit VA and the harder claystones of Subunit VB at about 510 mbsf. This implies a velocity of 1.91 km/s in Subunit VA, which is in good agreement with the physical properties measurements. Nevertheless, further study of the seismic profile revealed a short but strong reflector at 0.63 s TWT, which might represent the crystalline basement. So again assuming a conservative 3.0 km/s, we estimated the depth of this reflector to lie 120 m below the top of Subunit VB (i.e., at 630 mbsf). When no crystalline basement had been encountered by 631.4 mbsf, the hole was abandoned. With the benefit of the preliminary downhole logs, it appears that the actual interval velocities were well below the conservative assumption of 3.0 km/s (which ensured we overestimated the depths of reflectors). Further, the effective "depth" of the 0.55 s TWT reflector may have lain deeper than 510 mbsf (the top of Subunit VB), because the reflection is not the result of a first-order velocity increase at this depth but probably results from interference between positive and negative velocity contrasts between 510 and 540 mbsf. In that case, it now appears that crystalline basement might lie in the 650–700 mbsf range at this site; alternatively, crystalline basement could lie very much deeper and does not give rise to a clear seismic reflection. The above different interpretations of the reflector depths are presented in Tables 20, 21, and 22.

Conclusions

1. The fault block on which the site is located is capped on its eastern flank by a tilted seismically weakly reflective layer, at least 322 m thick, of Middle–Late Jurassic sediments deposited under offshore shelf conditions below wavebase.
2. The sediments and the fault block were tilted about 20° to the northeast, probably during the final Early Cretaceous phase of rifting.
3. Acoustic basement proved to be caused by hard bands of claystone and dolomitic claystone within Subunit VB rather than the crystalline continental basement that was expected. Even so, the evidence of shallow-water sedimentation in Jurassic times and the >4500 m subsidence since then strongly suggest that the site is underlain by continental crust.

REFERENCES

Boillot, G., Agrinier, P., Beslier, M.-O., Cornen, G., Froitzheim, N., Gardien, V., Girardeau, J., Gil-Ibarguchi, J.-I., Kornprobst, J., Moullade, M., Schaerer, U., and Vanney, J.-R., 1995. A lithospheric syn-rift shear zone at the ocean-continent transition: preliminary results of the GALINAUTE II cruise (Nautile dives on the Galicia Bank, Spain). *C. R. Acad. Sci. Ser 2a,* 321:1171–1178.

Capdevila, R., Boillot, G., Lepvrier, C., Malod, J., and Mascle, G., 1980. Les formations cristallines du Banc Le Danois (marge nord-ibérique), *C.R. Acad. Sci. Paris, Ser. D,* 317–320.

Capdevila, R., and Mougenot, D., 1988. Pre-Mesozoic basement of the western Iberian continental margin and its place in the Variscan Belt. *In* Boillot, G., Winterer, E.L., et al., *Proc. ODP, Sci. Results,* 103: College Station, TX (Ocean Drilling Program), 3–12.

Claypool, G.E., and Kvenvolden, K.A., 1983. Methane and other hydrocarbon gases in marine sediment. *Annu. Rev. Earth Planet. Sci.,* 11:299–327.

Collins, E.S., Kuhnt, W., and Scott, D.B., 1996. Tithonian benthic foraminifers from Hole 901A. *In* Whitmarsh, R.B., Sawyer, D.S., Klaus, A., and Masson, D.G. (Eds.), *Proc. ODP, Sci. Results,* 149: College Station, TX (Ocean Drilling Program), 193–201.

de Kaenel, E., and Bergen, J.A., 1996. Mesozoic calcareous nannofossil biostratigraphy from Sites 897, 899, and 901, Iberia Abyssal Plain: new biostratigraphic evidence. *In* Whitmarsh, R.B., Sawyer, D.S., Klaus, A., and Masson, D.G. (Eds.), *Proc. ODP, Sci. Results,* 149: College Station, TX (Ocean Drilling Program), 27–59.

de Kaenel, E., and Villa, G., 1996. Oligocene–Miocene calcareous nannofossil biostratigraphy and paleoecology from the Iberia Abyssal Plain. *In* Whitmarsh, R.B., Sawyer, D.S., Klaus, A., and Masson, D.G. (Eds.), *Proc. ODP, Sci. Results,* 149: College Station, TX (Ocean Drilling Program), 79–145.

Dennis, J.G., 1982. Closely spaced antithetic shear surfaces in siltstone. *In* Borradaile, G.J., Bayly, M.B., and Powell, C.M. (Eds.), *Atlas of Deformational and Metamorphic Rock Fabrics:* Berlin (Springer-Verlag), 194–195.

Fuegenshuh, B., Froitzheim, N., Gardien, V., Boillot, G., in press. Cooling history of granulite samples from the ocean-continent transition of the Galicia margin: implications for rifting. *Terra Nova.*

Francis, J.E., 1983. The dominant conifer of the Jurassic Purbeck Formation, England. *Palaeontology,* 26:277–94.

————, 1984. The seasonal environment of the Purbeck (Upper Jurassic) fossil forests. *Palaeogeogr., Palaeoclimatol., Palaeoecol.,* 48:285–307.

Galdeano, A., Moreau, M.G., Pozzi, J.P., Berthou, P.Y., and Malod, J.A., 1989. New paleomagnetic results from Cretaceous sediments near Lisboa (Portugal) and implications for the rotation of Iberia. *Earth Planet. Sci. Lett.,* 92:95–106.

Gradstein, F.M., Agterberg, F.P., Ogg, J.G., Hardenbol, J., van Veen, P., Thierry, J., and Huang, Z., 1995. A Triassic, Jurassic and Cretaceous time scale. *In* Berggren, W.A., Kent, D.V., and Aubry, M.P. (Eds.), *Geochronology, Time Scales and Global Stratigraphic Correlation.* Spec. Publ.—Soc. Econ. Paleontol. Mineral., 54:95–128.

Guerrot, C., Peucat, J.J., Capdevila, R., and Dosso, L., 1989. Archean protoliths within Early Proterozoic granulitic crust of the west European Hercynian belt: possible relics of the west African craton. *Geology,* 17:241–244.

Jansa, L.F., Comas, M.C., Sarti, M., and Haggerty, J.A., 1988. Late Jurassic carbonate platform of the Galicia Margin. *In* Boillot, G., Winterer, E.L., et al., *Proc. ODP, Sci. Results,* 103: College Station, TX (Ocean Drilling Program), 171–192.

Leinfelder, R.R., and Wilson, R.C.L., 1989. Seismic and sedimentologic features of Oxfordian-Kimmeridgian syn-rift sediments on the eastern margin of the Lusitanian Basin. *Geol. Rundsch.,* 78:81–104.

————, in press. Third order sequences in an Upper Jurassic rift-related second order sequence, central Lusitanian basin, Portugal. *In* Graciansky, P.-C., Hardenbol, J., Jaquin, T., Vail, P.R., and Farley, M.B. (Eds.), *Mesozoic and Cenozoic Sequence Stratigraphy of European Basins.* Spec. Publ.—Soc. Econ. Paleontol. Mineral.

Mamet, B., Comas, M.C., and Boillot, G., 1991. Late Paleozoic basin on the West Galicia Atlantic margin. *Geology,* 19:738–741.

Minshull, T.A., 1995. *A Geophysical Study of the Ocean-continent Transition in the Iberia Abyssal Plain, R.R.S. Discovery Cruise 215.* Bullard Labs., Dep. Earth Sci., Cambridge Univ.

Mohre, A.R, and Schmidt, D., 1988. The Oxfordian/Kimmeridgian boundary in the region of Porto de Mos (Central Portugal): stratigraphy, facies and palynology. *Neues Jahrb. Geol. Palaeontol. Abh.,* 176:245-267.

Postaire, B., 1983. Sistématique Pb et U-Pb sur zircons. Applications aux roches de haut grade métamorphique impliquées dans la chaine Hercynienne (Europe de l'Ouest) et aux granulites de Laponie (Finlande). *Bull. Soc. Geol. Mineral. Bretagne,* C15:29–72.

Ravnås, R., Windelstad, J., Mellere, D., Nøttvedt, A., Stuhr Sjøblom, T., Steel, R.J., and Wilson, R.C.L., 1997. A marine Late Jurassic syn-rift succession in the Lusitanian Basin, Western Portugal—tectonic significance of stratigraphic signature. *Sediment. Geol.,* 114:237–266.

Schott, J.J., Montigny, R., and Thuizat, R., 1981. Paleomagnetism and potassium-argon age of the Messejana dike (Portugal and Spain): angular limitation to the rotation of the Iberian Peninsula since the middle Jurassic. *Earth Planet. Sci. Lett.,* 53:457–470.

Serra, O., 1986. *Fundamentals of Well-Log Interpretation* (Vol. 2): *The Interpretation of Logging Data.* Dev. Pet. Sci., 15B.

Shipboard Scientific Party, 1994a. Site 897. *In* Sawyer, D.S., Whitmarsh, R.B., Klaus, A., et al., *Proc. ODP, Init. Repts.,* 149: College Station, TX (Ocean Drilling Program), 41–113.

————, 1994b. Site 899. *In* Sawyer, D.S., Whitmarsh, R.B., Klaus, A., et al., *Proc. ODP, Init. Repts.,* 149: College Station, TX (Ocean Drilling Program), 147–209.

————, 1994c. Site 900. *In* Sawyer, D.S., Whitmarsh, R.B., Klaus, A., et al., *Proc. ODP, Init. Repts.,* 149: College Station, TX (Ocean Drilling Program), 211–262.

————, 1994d. Site 901. *In* Sawyer, D.S., Whitmarsh, R.B., Klaus, A., et al., *Proc. ODP, Init. Repts.,* 149: College Station, TX (Ocean Drilling Program), 263–268.

Srivastova, S.K., 1976. The fossil pollen genus *Classopollis*. *Lethaia,* 9:437–457.

Suess, E., 1980. Particulate organic carbon flux in the oceans: surface productivity and oxygen utilization. *Nature,* 288:260–263.

Thusu, B., and Vigran, J.O., 1985. Middle-Late Jurassic (Late Bathonian-Tithonian) palynomorphs. *J. Micropalaeontol.,* 4:113-130.

Traverse, A., 1988. Paleopalynology: Boston (Unwyn Hyman).

Van der Voo, R., 1969. Paleomagnetic evidence for the rotation of the Iberia peninsula. *Tectonophysics,* 7:5–56.

Van Erve, A.W., Besems, R.E., and Love, C.F., 1988. A palynological investigation of some Lower Kimmeridgian deposits from Spain. *J. Micropaleontol.,* 17: 217-232.

Van Erve, A.W., and Mohr, B., 1988. Palynological investigations of the Late Jurassic microflora from the vertebrate locality Guimarota coal mine (Leira, Central Portugal). *Neues Jahrb. Geol. Palaeontol. Abh.,* 176:217-232.

Viscek, T., 1989. *Fractal Growth Phenomena: Singapore:* (World Scientific Press).

Whitmarsh, R.B., and Sawyer, D.S., 1996. The ocean/continent transition beneath the Iberia Abyssal Plain and continental-rifting to seafloor-spreading processes. *In* Whitmarsh, R.B., Sawyer, D.S., Klaus, A., and Masson, D.G. (Eds.), *Proc. ODP, Sci. Results,* 149: College Station, TX (Ocean Drilling Program), 713–733.

Wilson, R.C.L., Hiscott, R.N., Willis, M.G., and Gradstein, F.M., 1989. The Lusitanian Basin of west-central Portugal: Mesozoic and Tertiary tectonic, stratigraphic and subsidence history. *In* Tankard, A.J., and Balkwill, H.R. (Eds.), *Extensional Tectonics and Stratigraphy of the North Atlantic Margins.* AAPG Mem., 46:341–361.

Ms 173IR-103

NOTE: For all sites drilled, core-description forms ("barrel sheets") and core photographs can be found in Section 3, beginning on page 295. Forms containing smear-slide data, sedimentary thin-section descriptions, and igneous/metamorphic thin-section descriptions can be found on CD-ROM. See Table of Contents for material contained on CD-ROM.

APPENDIX. PALYNOLOGY[1]

Summary

Nine samples were analyzed for palynology from this site. Samples 173-1065-11R-CC, 4-7 cm, 13R-1, 5-8 cm, 13R-CC, 1-5 cm, and 22R-1, 8-12 cm, contain moderately abundant miospore assemblages dominated by *Classopollis* with common to abundant bisaccate pollen. Most of the species present are long-ranging forms typical of the Upper Jurassic–Lower Cretaceous. The fern spore (?)*Striatella scanica* ranges from the Anisian–lower Callovian, (?)Portlandian. All contain rare and quite poorly preserved marine dinocysts. *Systematophora daveyi* in Sample 173-1065-13R-CC, 1-5 cm, indicates a lower Kimmeridgian–post-Portlandian age. Deposition in a restricted marine environment with strong terrestrial influence is suggested by the strong dominance of miospores.

Samples 173-1065-23R-1, 2-5 cm, 24R-1, 59-62 cm, 33R-1, 81-85 cm, 33R-2, 77-80 cm, and 34R-1, 21-24 cm, contain predominantly terrestrially derived miospores. *Classopollis torosus* and *C. echinatus* are dominant with subordinate bisaccate pollen. Most species are long ranging. The presence of (?)*Striatella scanica* in Samples 173-1065-23R-1, 2-5 cm, and 33R-1W, 81-85 cm, indicates an age of Anisian–lower Callovian, (?)Portlandian. Deposition in a terrestrial or very restricted marine environment is suggested by the absence of dinocysts.

---

[1] Susan L.Matthews, Dept. of Geological Sciences, University College, London, U.K.

Results

Samples 11R-CC, 4-7 cm, 13R-1, 5-8 cm, 13R-CC, 1-5 cm, and 22R-1, 8-12 cm contain dominant *Classopollis (C. torosus and C. echinatus)* with occasional to abundant bisaccate pollen (*Vitreisporites pallidus* and *Alisporites* sp.). Also present are rare to occasional *Araucariacites australis, Cerebropollenites macroverrucosus, Eucommiidites troedssonii, Exesipollenites tumulus* and rare fern spores including *Callialasporites dampieri, Cibotiumspora juriensis, Deltoidospora* sp., and (?)*Striatella scanica.* No *Cicatricosisporites* sp. were present.

Rare marine dinocysts are present including *Adnatosphaeridium caullyeri* (Sample 173-1065-13R-1, 5-8 cm), *Systematophora daveyi* (Sample 173-1065-13R-CC, 1-5 cm), *Cribroperidinium globatum*, and (?)*Senoniasphaera* sp. (Sample 173-1065-22R-1, 8-12 cm).

Samples 173-1065-23R-1, 2-5 cm, 24R-1, 59-62 cm, 33R-1, 81-85 cm, 33R-2, 77-80 cm, 34R-1, 21-24 cm, contain poor to moderately abundant miospore assemblages dominated by *Classopollis* with bisaccate pollen (*Vitreisporites pallidus* and *Alisporites* sp.) also prominent. *Callialasporites dampieri*, *Spheripollenites psilatus,* and *Deltoidospora* sp. occur consistently. Other species sporadically present include *Cerebropollenites macroverrucosus, Exesipollenites tumulus, Araucariacites australis* and (?)*Striatella scanica. Cicatricosisporites* spp. were not present in any of these samples. A single specimen of the long-ranging acanthomorph acritarch, *Micrhystridium* sp. was present in Sample 173-1065-33R-1W, 81-85 cm. See Table 23 for full assemblage details.

Age Significance

Age determination of Samples 173-1065-11R-CC, 4-7 cm, 13R-1, 5-8 cm, 13R-CC, 1-5 cm, and 22R-1, 2-5 cm, is difficult because of the lack of good age- restricted marker species. The presence of *Adnatosphaeridium caullyeri* (lower Bathonian–post-Portlandian) in Sample 173-1065-13R-1, 5-8 cm, *Systematophora daveyi* (lower Kimmeridgian–post-Portlandian) in Sample 173-1065-13R-CC, 1-5 cm, and *Cribroperidinium globatum* (a mid-Oxfordian–post-Portlandian) in 22R-1, 8-12 cm, indicates a lower Kimmeridgian to post-Portlandian age based on scattered dinocyst evidence.

Miospores present are generally long-ranging Jurassic–Cretaceous forms, the species *Classopollis echinatus* (mid-Kimmeridgian–Albian) and (?)*Striatella scanica* (Anisian–lower Callovian, (?)Portlandian) both occur consistently. Overall, a mid-Kimmeridgian to Portlandian age is suggested.

The absence of the spore *Cicatricosisporites* is unusual. This genus usually occurs consistently in Kimmeridgian and younger samples in Portugal and Spain (Van Erve et al., 1988; Van Erve and Mohr, 1988; Mohre and Schmidt, 1988).

Samples 173-1065-23R-1, 2-5 cm, 24R-1, 59-62 cm, 33R-1, 81-85 cm, 33R-2, 77-80 cm, and 34R-1, 21-24 cm, contain miospore assemblages that are very similar to, although more impoverished than, those in the samples above. The presence of rare *Classopollis echinatus* (mid-Kimmeridgian–Albian) and (?)*Striatella scanica* (Anisian–lower Callovian, (?)Portlandian) again suggest a mid-Kimmeridgian–Portlandian age. As mentioned above, the absence of *Cicatricosisporites* is problematical, although overall abundance and diversity is quite low and may account for its non-occurrence. No dinocysts were recorded from these samples.

Palaeoenvironment

Samples 173-1065-11R-CC, 4-7 cm, 13R-1, 5-8 cm, 13R-CC, 1-5 cm, and 22R-1, 2-5 cm, contain moderately abundant palynofloral assemblages strongly dominated by terrestrially derived miospores. Rare dinocysts and chitinous microforaminiferal test linings are present scattered throughout and indicate deposition in a marine environment with very strong terrestrial influences. Miospore assemblages are dominated by *Classopollis* with subordinate bisaccate pollen; this is typical of Tethyan palynofloral assemblages (Thusu and Vigran, 1985).

Classopollis is a coniferous pollen characteristic of Lower Jurassic to mid-Cretaceous palynofloras. Its occurrence is widespread, particularly in lower latitudes, where it often occurs in abundance, often comprising over 90% of the assemblage. It is considered to have been produced mainly by a variety of warmth-loving shrubs, particularly by *Hirmeriella* and other cheirolepidiaceous conifers that grew in masses on low lying mudflats close to water, although some were able to withstand semi-arid conditions (Francis, 1983, 1984) and others grew on higher ground (Srivastova, 1976). Fern spores such as *Deltoidospora* sp., *Lycopodiacidites* sp., *Cibotiumspora juriensis, Lycopodiumsporites* sp., *Osmundacidites,* and (?)*Striatella scanica* were also probably derived from low-lying, possibly swampy areas while conifer taxa, *Araucariacites australis* and bisaccate pollen were most likely from a higher, more continental environment.

Samples 173-1065-23R-1, 2-5 cm, 24R-1, 59-62 cm, 33R-1, 81-85 cm, 33R-2, 77-80 cm, and 34R-1, 21-24 cm, contain no positive evidence of a marine environment. One isolated occurrence of the acanthomorph acritarch, *Micrhystridium* sp., was present in Sample 173-1065-33R-2, 77-80 cm. Acritarchs are known to tolerate wider salinity variations than most dinocysts, so this occurrence does not positively indicate the presence of marine conditions. The absence of good dinocyst assemblages (which are usually quite abundant and diverse in the Upper Jurassic and Lower Cretaceous) and the presence of moderate to poor miospore assemblages suggest deposition in either terrestrial freshwater or extremely restricted marine conditions. The composition of the miospore assemblages is similar to those described above.

All samples analyzed were processed in the palynological laboratory at University College London using standard palynological processing techniques. Thanks to P. Zippi for his careful review of the work presented here.

Table 23. Palynology abundance chart for Hole 1065A.

				Miospores																		Dinocysts								Others			
Age range	Core, section, interval (cm)	Depth (mbsf)	Abundance	*Classopollis torosus*	*Vitreisporites pallidus*	*Alisporites* spp.	*Classopollis echinatus*	*Cerebropollenites macroverrucosus*	*Exesipollenites tumulus*	*Araucariacites australis*	*Deltoidospora* sp.	*Spheripollenites psilatus*	(?)*Striatella scanica*	*Converrucosisportes* sp.	*Eucommiidites* sp.	*Callialasporites dampieri*	*Lycopodiacidites* sp.	*Cibotiumspora juriensis*	*Appendicisporites* sp.	*Lycopodiumsporites* sp.	*Osmundacidites* sp.	*Cribroperidinium globatum*	(?)*Senoniasphaera* sp.	(?)*Systematophora* sp.	*Adnatosphaeridium caullyeri*	*Cleistosphaeridium* sp.	*Systematophora daveyi*	*Gonyaulacysta* sp.	*Scriniodinium* sp.	Acanthomorph acritarch	*Micrhystridium* sp.	Microforaminiferal test linings	*Pediastrum* sp. (freshwater algae)
mid-Kimmeridgian–Portlandian	173-1065A-																																
mid-Kimmeridgian–Portlandian	11R-CC, 4-7	347.37	A	A	O	O	R				O	R	R	R	R	R								R						R		R	R
mid-Kimmeridgian–Portlandian	13R-1, 5-8	371.08	A	A	C	C	O	R	R	R	O	R	R		R		R	R							R	R						O	
mid-Kimmeridgian–Portlandian	13R-CC, 1-5	371.35	A	A	C	C	O	R	R	R	O	R	R						R	R							R	R				R	
mid-Kimmeridgian–Portlandian	22R-1, 8-12	482.32	A	A	A	C	O	R	O		O	O	R		R	R					R	R	R						R			R	
mid-Kimmeridgian–Portlandian	23R-1, 2-5	501.55	A	C	O	O	R	R	O	R	R	R	R			R																	
mid-Kimmeridgian–Portlandian	24R-1, 59-62	521.42	A	A	O	R			R		R	R				R																	
mid-Kimmeridgian–Portlandian	33R-1, 81-85	608.25	A	C	O	C					R	R	R			R															R		
mid-Kimmeridgian–Portlandian	33R-2, 77-80	609.65	C	O	R	R	R	R			R	R				R																	?R
mid-Kimmeridgian–Portlandian	34R-1, 21-24	617.34	A	A	C	C	R	R	R	R	O	R				R																	?R